Calhoun: The NPS Institutional Archive

DSpace Repository

Theses and Dissertations 1. Thesis and Dissertation Collection, all items

1981-06

Fatigue characteristics and microstructural analysis of thermomechanically-processed, high-magnesium aluminum-magnesium alloy

Cadwell, Charles A.

http://hdl.handle.net/10945/20527

Downloaded from NPS Archive: Calhoun

Calhoun is the Naval Postgraduate School's public access digital repository for research materials and institutional publications created by the NPS community. Calhoun is named for Professor of Mathematics Guy K. Calhoun, NPS's first appointed -- and published -- scholarly author.

Dudley Knox Library / Naval Postgraduate School
411 Dyer Road / 1 University Circle
Monterey, California USA 93943

http://www.nps.edu/library

FATIGUE CHARACTERISTICS AND MICROSTRUCTURAL ANALYSIS OF THERMOMECHANICALLY-PROCESSED, HIGH-MAGNESIUM ALUMINUM-MAGNESIUM ALLOY

Charles A. Cadwell

NAVAL POSTGRADUATE SCHOOL
Monterey, California

THESIS

FATIGUE CHARACTERISTICS AND MICROSTRUCTURAL ANALYSIS OF THERMOMECHANICALLY-PROCESSED, HIGH-MAGNESIUM ALUMINUM-MAGNESIUM ALLOY

by

Charles A. Cadwell, Jr.

June 1981

Thesis Advisor: T. R. McNelley

Approved for public release; distribution unlimited

T199254

Unclassified

SECURITY CLASSIFICATION OF THIS PAGE (When Data Entered)

REPORT DOCUMENTATION PAGE

READ INSTRUCTIONS BEFORE COMPLETING FORM

1. REPORT NUMBER

2. GOVT ACCESSION NO.

3. RECIPIENT'S CATALOG NUMBER

4. TITLE (and Subtitle) Fatigue Characteristics and Microstructural Analysis of Thermomechanically-Processed, High-Magnesium Aluminum-Magnesium Alloy

5. TYPE OF REPORT & PERIOD COVERED
Master's Thesis
June 1981

6. PERFORMING ORG. REPORT NUMBER

7. AUTHOR(s)
Charles A. Cadwell, Jr.

8. CONTRACT OR GRANT NUMBER(s)

9. PERFORMING ORGANIZATION NAME AND ADDRESS
Naval Postgraduate School
Monterey, California 93940

10. PROGRAM ELEMENT, PROJECT, TASK AREA & WORK UNIT NUMBERS

11. CONTROLLING OFFICE NAME AND ADDRESS
Naval Postgraduate School
Monterey, California 93940

12. REPORT DATE
June 1981

13. NUMBER OF PAGES
127

14. MONITORING AGENCY NAME & ADDRESS(if different from Controlling Office)

15. SECURITY CLASS. (of this report)
Unclassified

15a. DECLASSIFICATION/DOWNGRADING SCHEDULE

16. DISTRIBUTION STATEMENT (of this Report)

Approved for public release; distribution unlimited.

17. DISTRIBUTION STATEMENT (of the abstract entered in Block 20, if different from Report)

18. SUPPLEMENTARY NOTES

19. KEY WORDS (Continue on reverse side if necessary and identify by block number)

High-magnesium-aluminum magnesium alloys,
thermomechanical processing,
fatigue characteristics, microstructural analysis

20. ABSTRACT (Continue on reverse side if necessary and identify by block number)

This research was an investigation of the fatigue characteristics of warm rolled high-magnesium aluminum-magnesium alloys. Particular emphasis was placed on study of the microstructural changes which occur during cyclic loading. The study was conducted utilizing a simple binary alloy, Al-10.2 wt pct Mg, and a ternary Al-8.14 wt pct Mg-0.40 wt pct Cu alloy. Both alloys were given similar processing; in particular, both alloys were examined for

DD FORM 1473 1 JAN 73 EDITION OF 1 NOV 65 IS OBSOLETE
(Page 1) S/N 0102-014-6601

Unclassified

SECURITY CLASSIFICATION OF THIS PAGE (When Data Entered)

Item #20 continued:

two rates of quenching to determine the effect of cooling rate from the homogenization temperature on the tensile properties and fatigue characteristics of the alloys.

The primary strengthening mechanism in the high-magnesium aluminum-magnesium alloys was determined to be the dislocation substructure developed during warm rolling. In fatigue, the Al-10.2 wt pct Mg alloy appears to exhibit an endurance limit, with a fatigue strength to yield strength ratio in excess of 0.6 in the oil quenched condition. Microstructural refinement achieved through more rapid quenching or through alloying additions was found to degrade the fatigue response although providing improved strength and ductility.

Approved for public release; distribution unlimited

Fatigue Characteristics and Microstructural Analysis of Thermomechanically-Processed, High-Magnesium Aluminum-Magnesium Alloy

by

Charles A. Cadwell, Jr.
Lieutenant, United States Navy
B.S.M.E., Kansas University, 1975

Submitted in partial fulfillment of the
requirements of the degree of

MASTER OF SCIENCE IN MECHANICAL ENGINEERING

from the

NAVAL POSTGRADUATE SCHOOL
June 1981

ABSTRACT

This research was an investigation of the fatigue characteristics of warm rolled high-magnesium aluminum-magnesium alloys. Particular emphasis was placed on study of the microstructural changes which occur during cyclic loading. The study was conducted utilizing a simple binary alloy, Al-10.2 wt pct Mg, and a ternary Al-8.14 wt pct Mg-0.40 wt pct Cu alloy. Both alloys were given similar processing; in particular, both alloys were examined for two rates of quenching to determine the effect of cooling rate from the homogenization temperature on the tensile properties and fatigue characteristics of the alloys.

The primary strengthening mechanism in the high-magnesium aluminum-magnesium alloys was determined to be the dislocation substructure developed during warm rolling. In fatigue, the Al-10.2 wt pct Mg alloy appears to exhibit an endurance limit, with a fatigue strength to yield strength ratio in excess of 0.6 in the oil quenched condition. Microstructural refinement achieved through more rapid quenching or through alloying additions was found to degrade the fatigue response although providing improved strength and ductility.

TABLE OF CONTENTS

I. INTRODUCTION -- 16

II. BACKGROUND -- 18

- A. ALUMINUM-MAGNESIUM ALLOYS ----------------- 18
- B. PREVIOUS WORK ----------------------------- 20
- C. FATIGUE IN ALUMINUM ALLOYS ---------------- 23

III. EXPERIMENTAL PROCEDURES ---------------------- 27

- A. MATERIAL PROCESSING ----------------------- 27
- B. TENSILE TESTING --------------------------- 29
- C. FATIGUE TESTING --------------------------- 29
  - 1. Test Selection and Specimen Desing ---- 29
  - 2. Fatigue Testing Procedures ------------ 30
- D. METALLOGRAPHY ---------------------------- 32
- E. FRACTOGRAPHY ----------------------------- 33
- F. TRANSMISSION ELECTRON MICROSCOPY (TEM) ---- 33
  - 1. General Description ------------------ 33
  - 2. Electrolytic Thinning ---------------- 34

IV. RESULTS AND DISCUSSION ----------------------- 37

- A. MATERIAL PROCESSING ----------------------- 37
- B. RESULTING TENSILE PROPERTIES -------------- 38
- C. FATIGUE CHARACTERISTICS ------------------ 43
  - 1. Al-10.2 wt pct Mg Solution Treated, Oil Quenched and Warm-Rolled at 300°C - 43

2. Al-10.2 wt pct Mg Solution Treated Water-Quenched and Warm-Rolled at 300°C -- 51

3. Al-9.14 wt pct Mg-0.40 wt pct Cu Solution Treated, Oil-Quenched and Warm-Rolled at 300°C -------------------- 58

4. Al-8.14 wt pct Mg-0.40 wt pct Cu Solution Treated, Water-Quenched and Warm-Rolled at 300°C ---------------- 62

D. GENERAL DISCUSSION --------------------------- 65

V. CONCLUSIONS AND RECOMMENDATIONS ----------------- 70

A. CONCLUSIONS ---------------------------------- 70

B. RECOMMENDATIONS ------------------------------- 72

LIST OF REFERENCES ------------------------------------ 122

INITIAL DISTRIBUTION LIST ------------------------------- 125

LIST OF FIGURES

FIGURE 1. Partial Aluminum-Magnesium Phase Diagram --- 74

FIGURE 2. Fatigue Test Specimen Design Utilized for This Study ---------------------------------- 75

FIGURE 3. Electrolytic thinning apparatus utilized for thin foil preparation (power supplies included) ------------------------------------ 76

FIGURE 4. Fischione specimen holder, 3mm disc and plug used in foil preparation -------------- 77

FIGURE 5. Positioning of specimen holder and jet in final preparation for electrolyte thinning of foils -------------------------- 78

FIGURE 6. Al-8.14 wt pct Mg-0.40 wt pct Cu microstructure: (a) as-cast; (b) solution treated and water-quenched; (c) solution treated and oil-quenched ------ 79

FIGURE 7. Regions of intergranular cracking in billets of Al-8.14 wt pct Mg-0.40 wt pct Cu solution treated and water-quenched. Cracking occurred in both billets after 2 passes in rolling mill (rolling temperature 300°C) ------------------------- 80

FIGURE 8. Engineering Stress vs Engineering Plastic Strain for Al-10.2 wt pct Mg Solution Treated Oil-Quenched and Warm-Rolled at 300°C ----------------------------------- 81

FIGURE 9. Engineering Stress vs Engineering Plastic Strain for Al-10.2 wt pct Mg Solution Treated, Water-Quenched and Warm-Rolled at 300°C ----------------------------------- 82

FIGURE 10. Engineering Stress vs Engineering Plastic Strain for Al-8.14 wt pct Mg-0.40 wt pct Cu Solution Treated, Oil-Quenched and Warm Rolled at 300°C ---------------------- 83

FIGURE 11. Engineering Stress vs Engineering Plastic Strain for Al-8.14 wt pct Mg-0.40 wt pct Cu Solution Treated, Water-Quenched and Warm-Rolled at 300°C ---------------------- 84

FIGURE 12. Optical micrographs of the Al-10.2 wt pct Mg alloy, oil-quenched from homogenization: (a) longitudinal; (b) long transverse; (c) short transverse ------ 85

FIGURE 13. Optical micrographs of the Al-10.2 wt pct Mg alloy, water-quenched from homogenization: (a) longitudinal; (b) long transverse; (c) short transverse ------ 86

FIGURE 14. Optical micrographs of the Al-8.14 wt pct Mg-0.40 wt pct Cu alloy, oil-quenched from homogenization: (a) longitudinal; (b) long transverse; (c) short transverse -- 87

FIGURE 15. Optical micrographs of Al-8.14 wt pct Mg-0.40 wt pct Cu alloy, water-quenched from homogenization: (a) longitudinal; (b) long transverse; (c) short transverse -- 88

FIGURE 16. Regions of thin foils of Al-10.2 wt pct Mg, oil-quenched from homoginzation in the as-rolled condition indicating (a) heavily dislocated region similar to that expected of a cold worked material; (b) coarse precipitates which have sheared during subsequent rolling passes, and the diffuse cellular substructure; (c) light regions outlining original locations of precipitates and heavily dislocated structure ---------------------------------- 89

FIGURE 17. Regions of thin foils of Al-10.2 wt pct Mg water-quenched from homogenization, in the as rolled condition indicating (a) heavily dislocated and diffuse cellular substructure; (b) same region as (a), but tilted; (c) cellular nature of substructure more clearly defined at higher magnification ------------------------------ 90

FIGURE 18. Thin foil micrographs of Al-10.2 wt pct Mg solution treated and oil-quenched, indicating: (a) precipitates forming within GP zones, with dislocations pinned; (b) grain boundary with GP zones well defined to the right through tilting: (c) grain boundary triple point with precipitates nucleating in the grain boundaries: (d) precipitates nucleated within GP zones ---------------------------------- 91

FIGURE 19. Thin foils of Al-10.2 wt pct Mg artificially aged (a) oil-quenched from homogenization showing sites originally occupied by second phase particles; (b) oil-quenched from homogenization, relative free of precipitates with small dislocation density; (c) and (d) water-quenched precipitate growth during aging at 300°C with dislocations believed generated through increased volume occupied by second phase particles -------- 92

FIGURE 20. Al-10.2 wt pct Mg TEM micrographs contrasting cellular substructure of as-rolled materials when (a) oil-quenched from homogenization, and (b) water-quenched from homogenization. Both materials were warm-rolled at 300°C ----------------- 93

FIGURE 21. Stress Amaplitude vs Cycles to Failure for Al-10.2 wt pct Mg Solution Treated, Oil-Quenched and Warm-rolled at 300°C ----- 94

FIGURE 22. Hardness vs number of cycles to failure for Al-10.2 wt pct Mg solution treated, oil-quenched and warm-rolled at 300°C, illustrating cyclic hardening under low cycle fatigue conditions ----------------------- 95

FIGURE 23. Optical micrographs of a low cycle fatigued specimen of Al-10.2 wt pct Mg solution treated, oil-quenched and warm-rolled at 300°C: (a) adjacent to the main fracture surface (b) adjacent to the main fracture surface; (c) adjacent to the main fracture surface (dark field image); (d) adjacent to secondary crack (dark field image) ------ 96

FIGURE 24. Thin foil TEM Micrographs of Al-10.2 wt pct Mg solution treated, oil-quenched and warm-rolled at 300°C, after being tested under low cycle fatigue conditions (a) foil taken from a region adjacent to the main fracture surface parallel to the rolling plane (b) foil taken from a region heavily concentrated with secondary cracks (parallel to the rolling plane) ------------------------------ 97

FIGURE 25. Scanning Electron Fractograph of Stage II crack growth region of a specimen of Al-10.2 wt pct Mg, oil-quenched -from homogenization. Failure occurred after 3300 cycles of fully reversed bending fatigue; (a) 1100x; (b) 2200x ------------- 98

FIGURE 26. Overload region of same specimen as Figure 27 at 1175x on the Scanning Electron Microscope ----------------------- 99

FIGURE 27. (a) Regions of Stage II crack growth in a specimen of Al-10.2 wt pct Mg Oil-quenched from homogenization temperature which fractured after 1.81 x 10^5 cycles; (b) overload region of the same specimen (SEM x 1050) ------------------------------ 100

FIGURE 28. Transmission Electron Micrographs of thin foils taken from a plane parallel to the rolling plane of Al-10.2 wt pct Mg alloy, oil-quenched from homogenization and warm-rolled at 300°C. Failure occurred after 4.4 x 10^6 cycles -------------------- 101

FIGURE 29. Transition from Stage I growth to Stage II growth in Al-10.2 wt pct Mg, oil-quenched from homogenization and warm-rolled at 300°C. Failure occurred after 4.4 x 10^6 cycles of fully reversed bending fatigue. (a) SEM fractograph x600 (b) SEM fractograph x1200 ------------ 102

FIGURE 30. (a) Fully developed Stage II crack growth of same specimen shown in Figure 29; magnification 1100x SEM; (b) Stage III fracture appearance; magnification 1250x SEM ------------------ 103

FIGURE 31. Stress amplitude vs cycles to failure for Al-10.2 wt pct Mg solution treated, water-quenched and warm-rolled at 300°C --- 104

FIGURE 32. Hardness vs number of cycles to failure for Al-10.2 wt pct Mg solution treated, water-quenched and warm-rolled at 300°C, illustration cyclic hardening under low cycle fatigue conditions ----------------- 105

FIGURE 33. Optical micrographs of low cycle fatigued specimen of Al-10.2 wt pct Mg solution treated, water-quenched and warm-rolled at 300°C: (a) adjacent to the main fracture surface, (b), (c) and (d) adjacent to secondary cracks (dark field images) ---------------------------------- 106

FIGURE 34. Thin foil TEM micrograph of Al-10.2 wt pct Mg solution treated, water-quenched and warm-rolled at 300°C after being tested under low cycle fatigue conditions; (a) some indication of larger precipitates (b) region where volume fraction of precipitates is increased over the as-rolled condition (dark blotches in (b) are artifact from electrolyte thinning) ------- 107

FIGURE 35. SEM fractographs of Al-10.2 wt pct Mg, solution treated, water-quenched and warm-rolled at 300°C, in which fracture occurred after 3400 cycles: (a) Stage II crack growth x1050; (b) overload region x1050 ---------------------------------- 108

FIGURE 36. SEM fractographs of Al-10.2 wt pct Mg, water-quenched and warm-rolled at 300°C, in which fracture occurred after 10600 cycles: (a) Stage II striations x1050 and (b) Stage III (overload region) x1050 -- 109

FIGURE 37. Thin foil TEM micrographs of Al-10.2 wt pct Mg, water-quenched and warm-rolled at 300°C, in which failure occurred after 4.2×10^6 cycles: (a) regions of high dislocation density and relatively dislocation free zones; (b) same region as (a) except tilted; (c) region similar to those shown in (a) and (b), but from a different section of the fatigue specimen ----------- 110

FIGURE 38. SEM fractographs of Al-10.2 wt pct Mg, solution treated, water-quenched and warm-rolled at 300°C, in which failure occurred after 4.2×10^6 cycles: (a) Stage II crack growth x 1050; (b) Stage III crack growth x 1050 ------------------- 111

FIGURE 39. Stress amplitude vs cycles to failure for Al-8.14 wt pct Mg-0.40 wt pct Cu solution treated, oil-quenched and warm-rolled at 300°C -- 112

FIGURE 40. Optical micrographs of a low cycle fatigued specimen of Al-8.14 wt pct Mg-0.40 wt pct Cu, solution treated, oil-quenched and warm-rolled at 300°C: (a) adjacent to the main fracture surface; (b) adjacent to the main fracture surface; (c) secondary cracks originating at the main fracture surface; and (d) secondary cracks (dark image) --------------------- 113

FIGURE 41. SEM fractographs of a specimen of Al-8.14 wt pct Mg-0.40 wt pct Cu, solution treated, oil-quenched and warm-rolled at 300°C, in which failure occurred after 1400 cycles: (a) Stage II crack growth x1050; (b) Stage III crack growth x1050 ------------------- 114

FIGURE 42. SEM fractographs of a specimen of Al-8.14 wt pct Mg-0.40 wt pct Cu, solution treated, oil-quenched and warm-rolled at 300°C, in which failure occurred after 110200 cycles; (a) Stage II crack growth x1050; (b) Stage III crack growth x1050 -------------- 115

FIGURE 43. Microcrack formation on the surface of Al-8.14 wt pct Mg-0.40 wt pct Cu, solution treated, oil-quenched and warm-rolled at 300°C. Test terminated after 10^7 cycles without failure ---------- 116

FIGURE 44. Stress amplitude vs cycles to failure for Al-8.14 wt pct Mg-0.40 wt pct Cu, solution treated water-quenched and warm-rolled at 300°C ---------------------- 117

FIGURE 45. Optical micrographs of a low cycle fatigued specimen of Al-8.14 wt pct Mg-0.40 wt pct Cu, solution treated, water-quenched and warm-rolled at 300°C: (a) region adjacent to the main fracture surface; (b) region adjacent to the main fracture surface; (c) region adjacent to a blunt tipped secondary crack; and (d) region adjacent to and in front of a crack tip (dark field image) ------------------------------ 118

FIGURE 46. SEM fractographs of Al-8.14 wt pct Mg-0.40 wt pct Cu, solution treated, water-quenched and warm-rolled at 300°C, in which failure occurred after 2700 cycles: (a) Stage II crack growth x1200; (b) Stage III crack growth x1200 --- 119

FIGURE 47. SEM fractographs of Al-8.14 wt pct Mg -0.40 wt pct Cu, solution treated, water-quenched and warm-rolled at 300°C, in which failure occurred after 13.4 x 10^4 cycles: (a) Stage II crack growth x1050 ------------------------------ 120

FIGURE 48. SEM fractographs of Al-8.14 wt pct Mg-0.40 wt pct Cu, solution treated, water-quenched and warm-rolled at 300°C, in which failure occurred after 4.8 x 10^6 cycles: (a) Stage II crack growth x1200; (b) Stage III crack growth x1200 ---------------------------- 121

ACKNOWLEDGEMENT

I would like to take this opportunity to express my sincere thanks to those individuals who have given their support and guidance during the time span involved in completing this study. I would like to thank Professors T. R. McNelley and M. Edwards for their assistance as my advisors in organizing and conducting the experiments and in preparing the manuscript. Also worthy of mention are Mr. Tom Kellogg for his assistance in troubleshooting and repairing the required equipment in a timely fashion thus ensuring that the schedule could be met. I would like to thank the typist, Mrs. Edna Cerone for her advice in organizing the manuscript into the proper format. Finally, I would like to express my sincere appreciation to Janet and my sons for their patience and understanding and unwavering support throughout this research project.

I. INTRODUCTION

The purpose of this thesis was to investigate the fatigue characteristics of warm worked high-magnesium aluminum-magnesium alloys with particular emphasis on study of the microstructural changes which occur during cyclic loading. Studies conducted by Ness [Ref. 1], Bingay [Ref. 2], Glover [Ref. 3], Grandon [Ref. 4], Speed [Ref. 5], Chesterman [Ref. 6], and Johnson [Ref. 7] provided a basis for continuing research efforts with these alloys by demonstrating clearly that high strengths with good ductility are achievable through thermomechanical processing of these alloys.

The study extends the knowledge obtained from preceding efforts [Ref. 1-7] and utilizes Johnson's [Ref. 7] standardized thermomechanical process as a basis for determining the fatigue response of Al-10.2 wt pct Mg and Al-8.14 wt pct Mg-0.4 wt pct Cu alloys. Fatigue testing was accomplished via fully reversed bending at 2000 cycles per minute. Microstructures of material were studied utilizing optical metallographic techniques, Scanning Electron Microscopy and Transmission Electron Microscopy.

This thesis presents the data obtained from the fully reversed bending fatigue testing as well as microstructural evidence of the strengthening mechanism which is dominant in these alloys. Additionally, the observed changes in

microstructure for material subjected to low cycle fatigue and high cycle fatigue loading conditions is presented and provide valuable insight for subsequent investigations.

II. BACKGROUND

A. ALUMINUM-MAGNESIUM ALLOYS

Aluminum and its alloy systems have been the focal point of research for several years with the central theme being the development of materials with higher strength-to-weight ratios. The study of those alloys strengthened by the formation of discontinuous second phase precipitates has been directed towards improved understanding of the nucleation and growth kinetics of precipitate formation and relating the morphology of the precipitates to the material properties and characteristics of the alloys [Ref. 8]. The ultimate goal of developing materials with higher strength-to-weight ratios is the achievement of more efficient structural designs- the benefit of which is most significant when applied to the aerospace industry.

The aluminum-magnesium alloy system is of interest since the addition of magnesium to aluminum results in a decrease in density and also results in alloys of good strength, corrosion resistence, toughness and weldability. The equilibrium phase diagram (Figure 1) shows the solubility of magnesium in aluminum to decrease from its maximum of about 15 wt pct. magnesium at the eutectic temperature (451°C) to a value of 0.8 wt pct. magnesium at 100°C. The decreasing solubility of magnesium in aluminum as temperature decreases provides the driving potential for second-phase precipitate formation.

Alloys in which magnesium is utilized as the primary alloying element long have been commercially available (the 5xxx series alloys) and display excellent resistance to general corrosion and stress corrosion cracking, excellent workability and good fatigue strengths [Ref. 9]. The machinability, workability and resistance to stress corrosion cracking decrease as the magnesium content is increased [Ref. 9 and 10]. The higher volume fraction of second phase particles resulting from increased magnesium contents contribute to the decreasing machinability and workability. On quenching, magnesium segregates to the grain boundaries and the alloy reacts in a manner similar to sensitized stainless steel, with decreased resistance to stress corrosion cracking [Ref. 10]. The 5xxx series alloys (work hardenable alloys) are therefore, limited to less than about 5 weight percent magnesium [Ref. 9 and 10].

Aluminum-magnesium alloys containing greater than 5 weight percent magnesium respond as precipitation hardenable alloys due to the additional driving potential for precipitate formation created by the increased magnesium contents [Ref. 10]. Under conventional methods of age hardening, the workability, machinability and resistance to stress corrosion cracking follow the trend described above. Furthermore, strength increases and ductility decreases as the magnesium content is increased up to 14 weight percent. Alloys containing greater than 14 weight percent magnesium have been found to be too brittle to determine tensile properties [Ref. 10]. The use of

aluminum-magnesium alloys for age hardenability has not been widespread due to the relatively poor material properties they possess when compared to the 2xxx and 7xxx alloys.

B. PREVIOUS WORK

Ness [Ref. 1] initiated work in this area with an investigation of the influence of thermomechanical processing on an aluminum -18 wt pct alloy. This work attempted to apply concepts developed by Bly, Sherby and Young [Ref. 11] in their work on high-carbon steels. Essentially, this consists of mechanical working of an alloy composition at temperatures where two phases are present; mechanical working then results in microstructural refinement and subsequent improvement of mechanical properties. Ness [Ref. 1] demonstrated that microstructural refinement could be accomplished in such an alloy and reported compressive strengths in excess of 95 KSI (655 MPa). The central problem was, however, that very slow rolling was required to avoid cracking of the material during processing.

Bingay [Ref. 2] and Glover [Ref. 3] examined variations on the thermomechanical processing used by Ness and sought conditions to facilitate processing of the material. Bingay [Ref. 2] employed both isothermal and nonisothermal forging prior to rolling in an attempt to refine microstructures of alloys containing 15 to 19 wt pct magnesium. With such alloys containing more than the maximum solubility of magnesium the

desired refinement was not obtained and the recommendation was made that alloys containing less than the maximum solubility of magnesium (i.e. less than 15 wt pct) be examined and that the process be modified to include solution treatment prior to deformation processing in the two-phase condition. Glover [Ref. 3] reported mechanical test data on a series of isothermally forged alloys containing from 7 to 19 wt pct magnesium and noted several characteristics of superplastic materials, especially in the higher magnesium alloys.

Grandon [Ref. 4] combined the recommendations of preceeding efforts in a study of alloys containing 7 to 10 wt pct magnesium. He introduced a twenty-four hour solution treatment followed by quenching, reheating and warm rolling at 300°C. This work demonstrated that such processing could result in materials with high strength and good ductility. Alloys containing larger amounts of magnesium were examined by Speed [Ref. 5]. Such alloys were readily worked at temperatures above the solvus but during warm rolling severe edge cracking and alligatoring occurred and the limited tensile data obtained suggested generally poor ductility in 12 wt pct magnesium alloys.

Several questions were raised in the work described above regarding the nature of precipitation and recrystallization in these high magnesium alloys. Chesterman [Ref. 6] addressed these questions and concluded that recrystallization does not occur during deformation at any temperature below the solvus

for magnesium in alloys continuing up to 14 wt pct magnesium. Also, cold work followed by annealing would not induce recrystallization if the annealing temperature were below the solvus. This rather surprising result was obtained even in alloys where such annealing would take place at temperatures above 0.6 T_M where T_M is the melting temperature for the alloy. Rather, precipitation always replaced recrystallization as the means by which stored energy was released.

Johnson [Ref. 7] successfully consolidated the results obtained by his predecessors [Refs. 1, 2, 3, 4, 5, 6], and developed a standardized thermomechanical process for high magnesium, aluminum-magnesium alloys. He applied this standardized process to six alloys in which magnesium is the major alloying element, with magnesium additions ranging from 8.14 weight percent to 10.4 weight percent. He produced alloys which exhibited yield strengths exceeding the strongest 5000 series commercial alloys by more than 200% and yet maintained moderate ductilities. His process consisted of solution treatment of the alloy for 10 hours at 440°C, with an isothermal upset forging at 440°C after nine hours of solution treatment. The material was subsequently quenched to room temperature and then warm worked in a rolling mill to final plate thickness. Warm rolling temperatures ranged from 200°C to 340°C. He found that controlling the precipitation of the fine "beta" intermetalic to be the most significant factor in obtaining the best strength and ductility. A more comprehensive

description of the thermomechanical process which he employed is presented in the "EXPERIMENTAL PROCEDURES" section of this thesis. Johnson [Ref. 7] recommended that a fatigue study on high magnesium, aluminum-magnesium alloys be conducted utilizing the standardized thermomechanical processing scheme as a basis for obtaining the initial material properties. He further recommended that a study of the effects of quenching rates be conducted to determine the effect of quench rate on microstructure and material properties.

C. FATIGUE IN ALUMINUM ALLOYS

Fatigue is defined as the progressive permanent damage of a material which occurs due to cyclic loading [Ref. 12]. The loading conditions are such that the material is subjected to stresses which cycle between minimum and maximum values, possess a tensile component and cause local plastic deformation. The process of fatigue may be divided into three stages [Ref. 12].

Stage I is the crack initiation stage. It is characterized by the piling up of dislocations along the surface (microslip) creating microscopic cracks at 45° to the maximum tensile stress component. Typically, crack growth in this stage will be from one to five grain diameters in depth and will give the appearance of a slip plane fracture (smooth and silky appearance). The crack is propagating by shear in stage one. Stage one initiation is strongly dependent upon the surface finish and strength of the material [Ref. 12].

Stage II is the crack propagation stage. In this phase of fatigue, crack growth is under plane strain conditions and occurs perpendicular to the maximum tensile stress component. On a macroscopic scale, beach marks may be evident (usually under spectrum loading conditions) and microscopic striations indicate the step wise crack growth with each loading cycle.

Stage III is the final fracture and occurs when crack growth under Stage II progresses to the point where the conditions for fast fracture are satisfied, i.e. the crack length and maximum stress in combination reach the fracture toughness of the material. Failure may be by either ductile or brittle overload.

The analysis of the fatigue properties of high strength aluminum alloys is complex since a consideration of the interaction between crack growth pehnomenon and the precipitates which strengthen the alloys is required [Ref.s 8, 13, 14, 15]. Commercial alloys containing high levels of iron and silicon impurities have been found to exhibit substantially reduced fatigue properties [Ref. 8]. This is attributed to the formation of coarse intermetallic particles which do not contribute to strength and either fracture or separate from the matrix at low levels of local plastic strain.

The aluminum-copper-magnesium alloys (the 2xxx series) exhibit fatigue characteristics which are sensitive to the state of age hardening. For these alloys, the maximum fatigue strength occurs before the intermediate phase forms and the

minimum fatigue strength occurs with the formation of coherent $CuMgAl_2$ precipitates [Ref. 16]. The presence of $CuMgAl_2$ phase degrades fatigue life by providing localized stress concentrations which serve as crack initiation sites and may accelerate crack growth. The precipitates form as sharp-cornered platelets. Additionally, retrogression and reformation of GP zones under cyclic loading is found to occur in these alloys [Ref. 16].

The aluminum-zinc-magnesium alloy system displays no endurance limit and reported values for fatigue strength vary. Values reported depend upon the method of testing, frequency of load reversals, surface defects and the testing environment [Ref. 17]. For these alloys, the formation of slip bands in which fine precipitates are redissolved and subsequently reprecipitated as coarse particles preceeds fatigue failure [Ref. 17]. Under certain conditions, grain boundary sliding can be induced in aluminum-zinc-magnesium alloys at room temperature which will subsequently develop into intergranular fatigue failure under cyclic loading [Ref. 18].

Increased precipitation under cyclic loading can occur in high magnesium, aluminum-magnesium alloys. Stubbington [Ref. 19] found that fatigue deformation of an Al-12.5 wt pct Mg alloy produced a fine, homogeneous distribution of precipitates as a result of the formation of many suitable nucleation sites by the cyclic stress. This reduced "the incubation period for hardening" and increased the slope of

the hardness versus time curve [Ref. 20]. The nucleation sites produced under cyclic loading were thought to be the dislocation loops "so commonly produced by the fatigue stress" [Ref. 20].

Aluminum-magnesium alloys with less than about 5 weight percent magnesium display an "abnormally small response to age hardening", and exhibit high fatigue strengths [Ref. 13]. Stress versus number of cycles to failure curves for these alloys exhibit "true endurance limits which is uncommon for non-ferrous materials" [Ref. 13].

III. EXPERIMENTAL PROCEDURES

A. MATERIAL PROCESSING

The alloys selected for study were Al-10.2 wt pct Mg and Al-8.14 wt pct Mg - 0.40 wt pct Cu, and were obtained as direct chill cast ingots 127 mm (5 in) in diameter by 1016 mm (40in) in length. The ingots were produced by ALCOA utilizing 99.99% pure Al as a base metal and were alloyed using commercially pure copper and magnesium, 5% beryllium-aluminum master alloy and 5% titanium -0.2% boron-aluminum rod [Ref. 7]. The as-received compositions of the alloys are shown below with alloy additions in weight percentage [Ref. 7].

SERIAL NUMBER	Si	Fe	Cu	Mg	Ti	Be
501299A	0.01	0.03	0.00	10.2	0.01	0.0002
501303A	0.01	0.03	0.40	9.14	0.01	0.0002

The as-received ingots were sectioned to produce billets of 96 mm (3.75 in) length by 32 mm (1.25 in) by 32 mm (125 mm) crossection to facilitate subsequent thermomechanical processing.

The thermomechanical processing scheme employed was that developed by Johnson [Ref. 7]. Briefly, the as-cast billets were solution treated at 440°C for nine hours. The billets were then isothermally forged at 440°C from a length of 96 mm (3.75 in) to a maximum height of 32 mm (1.25 in) to provide hot work and break up the dendritic, as cast microstructure. After forging, the billets received an additional one hour of

annealing at 440°C to ensure complete solutionizing. The billets were then quenched to room temperature utilizing either oil or water as a quenching medium.

The forged billets were further deformed following the warm rolling procedure developed by Johnson [Ref. 7]. A warm rolling temperature of 300°C was selected to examined the fatigue response of alloys processed at an intermediate temperature with respect to the range of rolling temperatures utilized by Johnson [Ref. 7]. The warm rolling was accomplished by first heating the billets to the rolling temperature. This required placing the billets in a preheated furnace for 10 minutes prior to the first pass through the rolling mill. Further consideration of temperature loss which occurs during each pass (since the mill rollers are not heated) required a two-minute interval in the furnace between passes to permit the billet temperature to stabilize at the desired rolling temperature. This temperature loss was found to average approximately 20°C per pass by Grandon [Ref. 4] and the interval between passes required to restore the billet to the required temperature was determined by Johnson [Ref. 7]. These are average values and were easily verified by taking temperature readings on the billet surfaces before and after each pass. (Each pass through the mill requires approximately 15 seconds.)

To maintain straightness of the billets as they were rolled, a four-pass sequence was utilized [Ref. 7]. This sequence

consisted of "passing each end of the billet through the rolling mill and then turning it over and repeating the same pattern" [Ref. 7]. Final thickness was 0.140 in (3.6 mm) in all cases.

B. TENSILE TESTING

Tensile specimens were machined from sections of each rolled plate to compare data obtained from this project with the previous results obtained by Johnson [Ref. 7] and to served as a basis for predicting the fatigue behavior of the alloys. The tensile specimens were machined with a 38 mm 1.5 in) gage length and testing was accomplished utilizing a model TT-D Instron Floor Model testing machine and a cross-head speed of 5 mm (0.2 in) per minute.

C. FATIGUE TESTING

1. Test Selection and Specimen Design

The selection of a method of testing the fatigue properties of the alloys was dictated by the material processing scheme employed. The most suitable test for flat plate is one of fully reversed bending, in which a tapered cantilever beam with the load applied at the apex of the triangular shape formed by extending the sides of the tapered test specimen [Ref. 21]. The specimen design selected is shown in Figure 2.

2. Fatigue Testing Procedures

Fatigue testing was accomplished utilizing a Tatnall-Krouse Variable Speed Plate Fatigue Testing Machine with a 150lb load capacity. The machine is of the fixed deflection type and uses the specimen as its own dynamometer.

The machine is calibrated with each specimen in its test position; the fixed end of the specimen is clamped in a horizontally and vertically adjustable vise which is alligned to the appropriate mean stress level. A variable throw crank transmits the loading force of the machine through a rigid connecting rod to the specimen. The machine is equipped with a cycle counter and an automatic cut-off switch which deenergizes the machine and activates a magnetic brake when the specimen fractures. A machine speed of 1980 RPM (was used) which equates to 1980 fully reversed fatigue cycles per minute.

Specimen loading is determined by measuring the deflection caused when a given load is suspended from the "free end" of the specimen while the fixed end is securely clamped in the vise. Then by adjusting the variable throw crank to the same deflection with the specimen connected via the connecting rod, the desired stress within the gauge length is obtained.

Calculations of bending stresses were accomplished using the flexure formula [Ref. 22],

$$S = \frac{Mc}{I} , \qquad (1)$$

where S is the tensile stress at the surface of the specimen,

M is the applied bending moment, I is the moment of inertia of the cross sectional area about the centroidal axis, and c is half the specimen thickness. Within the tapered gauge length, the ratio of M/I remains constant. Therefore, the stress at any point along the surface of the gauge length is the same. For a rectangular cross-sectional area [Ref. 23],

$$I = \frac{bt^3}{12} \tag{2}$$

where b is the specimen width and t is the specimen thickness. Thus the stress equation can be reduced to

$$S = \frac{6PL}{bt^2} , \tag{3}$$

where P is the load applied at the apex of the taper, L is the distance from the apex of the taper to clamped end of the gauge length and b is the specimen width at a distance L from the point of load application. Rearranging and solving the stress equation for P, we have

$$P = \frac{Sbt^2}{6L} \quad . \tag{4}$$

Due to the length of time required to test a specimen to more than 10^7 cycles, an estimate of the slope of the fatigue curves was made utilizing the Basquin relationship [Ref. 24],

$$\frac{\Delta\varepsilon_e}{2} = \frac{\sigma_a}{E} = \frac{\sigma_f'}{E}(2N_f)^b ; \tag{5}$$

where E is the modulus of elasticity for the material, σ_a is the stress amplitude, σ_f' is the fatigue strength coefficient (taken as the ultimate tensile strength for the predictions) and b is the fatigue strength exponent [Ref. 25]. The estimated

performance curves were based on the assumption that E for these alloys is 10.2×10^6 PSI and b is -0.11. These values correspond to those of the 5000 series aluminum alloys and were therefore considered conservative. By selecting stress values midrange on the estimated curves (which were plotted from 10^0 through 10^7 cycles), the initial data points were obtained. Then, using the predicted slopes, subsequent loading conditions could be determined without excessive expenditure of materials and time.

D. METALLOGRAPHY

Sections of the as rolled plate were mounted to examine the longitudinal, long transverse and short transverse microstructures. Additionally, fatigued specimens were mounted to allow optical examination of the crack growth in both the low cycle and high cycle fatigue conditions.

Metallographic samples were mounted in bakelite. Polishing was accomplished utilizing wet sand papers of 240, 400 and 600 grit, followed by 1.0 micron and 0.05 micron aluminum oxide slurries. The final finish was obtained using a magomet slurry and an automatic vibromet polisher. The polished specimens were etched with Keller's reagent [Ref. 26] for 35 seconds and examination was accomplished utilizing a Zeiss optical microscope.

E. FRACTOGRAPHY

Fractured fatigue specimens from the low, intermediate and high cycle fatigue regimes were sectioned and mounted to permit examination of the fracture surfaces using a Cambridge S4-10 Scanning Electron Microscope. The crack growth regions (Stage II fatigue) and the overload regions (Stage III) were examined and photographed to allow subsequent comparison of the materials response in each fatigue regime and to make microstructural comparisons where possible.

F. TRANSMISSION ELECTRON MICROSCOPY (TEM)

1. General Description

In order to obtain more detailed microstructural information, the Al-10.2 wt pct Mg binary alloy was selected for TEM analysis. Thin foils were prepared from both oil-and water-quenched materials such that microstructural analysis of the alloy in five stages could be accomplished. The five conditions selected were: as-quenched; quenched and artificially aged; as warm-rolled; after low cycle fatigue; and after high cycle fatigue.

Thin foil preparation was accomlished utilizing a non-submerged jet thinning technique in which the foil is thinned from one side at a time. The electrolyte used was 1 part perchloric acid in 4 parts ethanol, with an applied potential of 20 volts DC and a current density of approximately 0.1 amperes per square centimeter [Ref. 27].

Material from each of the previously mentioned conditions was sectioned on a plane parallel to the rolling plane

(longitudinal direction) to produce a thin sheet of material approximately0.010 in (0.3 mm) thickness. Sectioning was accomplished utilizing a Buehler ISOMET Model 11-1180 Low Speed Diamond Saw. The sectioned sheets were then mechanically thinned to a thickness of approximately 0.006 in (0.2 mm) utilizing 600 grit wet sand paper. This was accomplished by using double-stick tape to bond the sheets to a sanding bar and then hand sanding to the desired thickness. Acetone was then used to dissolve the tape and allow removal of the thinned sheet from the sanding block. Three-millimeter diameter discs were then stamped from the 0.006 in sheets for electrolytic thinning.

2. Electrolytic Thinning

The thinning apparatus utilized was a modified Buehler Electromet with the light source and photocells removed. The pump housing was wedged in the bottom of the beaker with the magnetic impeller in place. One jet was used and the beaker was cut to accomodate the installation of a viewing window. An external low-power microscope and light source were positioned to allow continuous monitoring of the foil as thinning was accomplished. This is the same apparatus utilized by Vining [Ref. 27] and Schultz [Ref. 28] and is shown along with power supplies in Figure 3.

Final preparation of the 3 mm discs for thinning required removal of all rough edges utilizing dry 600 grit sand paper. The disc was then mounted in a Fischione

"lollypop" specimen holder. Figure 4 shows the Fischion1 specimen holder and 3 mm disc ready for mounting. Care was taken to ensure that the specimen holder was thoroughly dry inside prior to placing the 3 mm disc in contact with the platinum electrode and insertion of the plug. The plug was securely tightened to prevent the electrolyte from leaking around the disc during thinning.

Five hundred milileters of electrolyte were then placed in the beaker and the specimen holder was postioned approximately 10 mm (0.375 in) from the jet with the 3mm disc centered in the jet stream as shown in Figure 5.

The desired electrical potential is applied by connecting the cathode lead to the coil which surrounds the jet, and connecting the anode lead to the specimen holder. The thinning process begins as soon as the pump, line, and DC switches on the power supply are positioned on. Best results were obtained with a pump speed setting of "3" on the power supply.

To account for slight variations in thickness which may occur from the mechanical thinning of the thin sheets, the first 3 mm disc from each sheet was thinned from one side only and the length of time required to achieve penetration was measured. Half the length of time required to achieve penetration provided an excellent estimate of the time required to thin each side and produce a useable foil. The remainder of the discs were thinned on one side for the proper time

at which point the specimen holder was disconnected and removed from the thinning apparatus. The specimen holder, plug and foil were washed with ethanol and thoroughly dried using an air dryer, and then reassembled with the unpolished side of the foil facing the jet. With the low power microscope and its light source focused to allow close monitoring of the specimen, thinning was initiated on the remaining side of the foil. The line current switch on the power supply was turned off at the first sign of penetration (usually detected as a small burst of electrolyte coming through the foil). At this point, the specimen holder was again removed from the apparatus and dismantled (carefully, to prevent bending the foil). The foil was rinsed in ethanol and air dried and then placed in a desiccator to await subsequent TEM analysis. This must usually be accomplished within three days to minimize oxidation damage to the foil [Ref. 26]. The specimen holder and plug were rinsed in ethanol and thoroughly dried before and after each use to prevent contaminants from degrading the effectiveness of subsequent thinning operations.

It should be noted that perchloric acid is highly reactive and leaves a powdery residue when it dries which is explosive. Extreme care was taken to ensure that no electrolyte was allowed to dry on surfaces if spilled. The spilled electrolyte was immediately wiped up with a damp sponge and then the sponge was thoroughly rinsed with fresh water.

IV. RESULTS AND DISCUSSION

A. MATERIAL PROCESSING

The standardized thermomechanical processing scheme developed by Johnson [Ref. 7] was followed as closely as possible, deforming the material to the greatest extent possible with each pass through the rolling mill. No difficulty was encountered in processing the Al-10.2 wt pct Mg alloy in either the oil-quenched or the water-quenched condition. This material was processed utilizing a 0.04 in. (1.0mm) reduction in thickness per pass throughout the rolling sequence. In contrast, the Al-8.14 wt pct Mg -0.40 wt pct Cu alloy exhibited a severe tendency to crack when applying the same degree of reduction in thickness per pass. This was apparent in both oil-quenched and water-quenched materials, with cracking occurring on the first or second pass.

Metallographic samples of as-cast materials and as-quenched materials (both oil and water) were compared microstructurally as shown in Figure 6. Figure 6(a) shows the as-cast microstructure to be dendritic in nature, typical of a cast material. Segregation which roughly corresponds to the distribution of dendrites in the original as-cast microstructure is evident in Figures 6(b) and (c).

Cracked billets of the Al-8.14 wt pct Mg -0.40 wt pct Cu alloy were sectioned and examined metallographically. Figure

7 shows the intergranular nature of cracking in two billets of Al-8.14 wt pct Mg -0.40 wt pct Cu, each of which cracked after a true rolling strain of 0.08 at 0.04 in.(1.0mm per pass.

Mondolfo [Ref. 16] indicates that at 300°C it is possible to form the ternary phase $CuMg_4Al_6$ if sufficient magnesium is available to form the phase (approximately 9 wt pct Mg from the ternary phase diagram for Al-Cu-Mg). With the degree of segregation suggested by the microstructural comparison of the as-cast and as-quenched materials, it is probable that at least some regions of the material favor ternary phase formation with grain boundaries providing the most favorable nucleation sites. The severe cracking tendency is therefore attributable to ternary phase precipitates forming preferentially in the grain boundaries with precipitation enhanced by an inhomogeneous distribution of magnesium and copper following the solution treatment.

The Al-8.14 wt pct Mg -0.40 wt pct Cu alloy was processed by reducing the amount of deformation per pass to 0.02 in. (0.5 mm) reduction in thickness per rolling pass. In this manner, a sufficient amount of material was processed to conduct the remaining experiments. Cracking and alligatoring were held to acceptable limits while processing the alloy at the reduced rate of deformation.

B. RESULTING TENSILE PROPERTIES

Correlation of the results obtained from tensile tests with those obtained by Johnson [Ref. 7] was excellent. A

somewhat reduced 0.2% yield strength was noted in all samples tested and this attributed to a difference in interpretation of the strip charts from the Instron machine.

Figures 8-11 are engineering stress versus engineering plastic strain plots for the alloys as they were processed.

The Al-10.2 wt pct Mg alloy exhibits a 0.2% yield strength of approximately 46 KSI (317 MPa) in both the oil-quenched and water-quenched conditions. Comparison of Figures 8 and 9 shows the water-quenched condition to be somehwat stronger, with an ultimate tensile strength of 70.6 KSI (487 MPa) compared to an ultimate tensile strength of 64.6 KSI (445 MPa) for the oil-quenched condition, and the water-quenched material is also more ductile than the oil-quenched material.

Comparison of Figures 10 and 11 indicates that both the oil-and water-quenched Al-8.14 wt pct Mg-0.40 wt pct Cu materials possess similar strengths, with 0.2% offset yield strengths of 51 KSI (353 MPa) and ultimate tensile strengths of 65 KSI (448 MPa). The water-quenched material here exhibits a marked increase in ductility (14.8% elongation) over the oil-quenched material (10.5% elongation).

Figures 12-15 show the microstructures of these materials in the as-rolled condition. Little difference in the microstructure is notable from the optical micrographs other than a possibly more uniform precipitate dispersion in the water-quenched materials.

Subsequent transmission electron microscopy analysis of thin foils of the Al-10.2 wt pct Mg alloy in the as-rolled condition for prior quenching in either oil or water indicates an inhomogeneous precipitate dispersion in a diffuse dislocation substructure. Figures 16 and 17 show the resulting substructures obtained when the alloy was oil-quenched and water-quenched from solution treatment respectively. Several regions of extremely dense dislocations are evident in foils prepared from both oil-quenched and water-quenched materials. In these regions the material appears cold worked despite the relatively high warm rolling temperature at which it was processed. The light areas which appear at cell nodes are believed to be locations which were occupied by precipitates dislodged during foil preparation.

In order to gain a better understanding of the strengthening characteristics of the Al-10.2 wt pct Mg alloy and its precipitate morphology, rolled plates were solution treated for 2 hours at 440°C, quenched to room temperature and then aged at 300°C for 2 hours. Both oil and water were utilized as a quenching medium. Thin foils were prepared from the material in the as-quenched and aged conditions.

GP zones were evident in the as-quenched condition with a few grain boundary precipitates. Figure 18 shows the GP zones in a sample which was solution treated and quenched to room temperature in oil. Grain boundaries exhibit sub-micron precipitates, and within the grains there are highly angular

precipitates clearly resolvable and a relatively low dislocation density. It should be noted that the morphology of the precipitates found in the as-quenched material supports the assumption that the light regions appearing at substructure nodes in the as-rolled materials (Figure 16 and 17) are sites which were occupied by precipitates.

Figure 19 shows a relatively inhomogeneous precipitate distribution in the aged materials and also indicates the angular morphology of precipitates. Figures 19(a) and (b) are from foils prepared from Al-10.2 wt pct Mg plate which was solution treated at 440°C for 2 hours, oil-quenched and aged at 300°C for 2 hours. Figures 19(c) and (d) are from foils of the same alloy and similar processing except that the quenching medium was water. Note the increased dislocation density present in the aged conditon (compared to the as-quenched conditions, Fig. 18) with the dislocations being generated by the increased volume occupied by precipitates forming within the solid solution [Ref. 10 and 29].

The primary strengthening mechanism in these alloys appears to be the dislocation substructure developed during warm-rolling. Precipitate formation occurs at grain boundaries and at dislocation cell nodes within the grains, which provide the most energetically favorable nucleation sites [Ref. 29]. As precipitates nucleate at the substructure nodes, growth is supported by dislocation core diffusion along the cell walls and by Mg atoms dragged with disloations as they move to the

cell walls and tangle during warm-rolling. Precipitates may stabilize the substructure in the alloy but in general they appear too large to provide direct strengthening via the Orowan mechanism.

The average cell size of oil-quenched material was found to be about 0.3 μm and the average cell size of water-quenched material was found to be about 0.1 μm. Comparison of substructures for the two quenching conditions is shown in Figure 20. Figure 20(a) shows the substructure of Al-10.2 wt pct Mg, oil-quenched from homogenization and warm-rolled at 300°C, in contrast to Figure 20(b) which is the same alloy but water-quenched from homogenization, and warm-rolled at 300°C. The greater strength and ductility of the water quenched material is attributed to the finer substructure developed during warm rolling. Additionally, the apparently more uniform precipitate dispersion indicated in the optical micrographs of water-quenched materials (Figures 13 and 15) is attributable to the closer proximity of nucleation sites (substructure cell nodes). The development of a finer dislocation substructure in water-quenched material is most probably a result of a greater retention of magnesium in solution due to the more rapid quench from homogenization temperature. Magnesium atoms interact with dislocations and pin them, thus retarding their mobility [Ref. 10, 13]. This increased interaction with dislocations results in more rapid tangling and thus the formation of more refined substructure.

The addition of copper to the aluminum-magnesium system provides additional refinement in that copper, when in solid solution, tends to retard the diffusion of magnesium [Ref. 16]. This results in an effect similar to water-quenching the Al-10.2 wt pct Mg alloy. That is, the introduction of copper results in more magnesium being retained in solution when the Al-8.14 wt pct Mg -0.40 wt pct Cu alloy is oil-quenched. Copper addition also provides increased strength at a cost of somehwat reduced ductility [Ref. 16].

The refining properties of copper combined with those of a more rapid quench rate are shown in the marked increase in ductility which occurs when the Al-8.14 wt pct Mg -0.40 wt pct Cu alloy is water-quenched. The increased strength achieved through the addition of copper is retained while ductility is improved from 10.5% to 14.8%.

C. FATIGUE CHARACTERISTICS

1. Al-10.2 wt pct Mg Solution Treated, Oil Quenched and Warm-Rolled at 300°C

Figure 21 shows the experimental results obtained from the fatigue tesing conducted on the Al-10.2 wt pct Mg alloy solution treated, oil-quenched and warm-rolled at 300°C. The Basquin prediction of the fatigue response (based upon the tensile data) is included for comparison.

The alloy appears to cyclically harden under low cycle fatigue conditions, especially when loaded at stresses above the yield-strength. This is implied by the degree of

improvement in the observed fatigue life over the predicted life at high stress loadings. The Basquin prediction is based on the assumption that the material behaves in a purely elastic fashion and therefore the relative appearance of the experimental results in contrast to the Basquin curve is not sufficient in itself to be conclusive [Ref. 25].

The high cycle fatigue response of the alloy is also better than the Basquin prediction and suggests an endurance limit beyond 10^7 cycles, with a corresponding fatigue strength of 30 KSI (207 MPa). At stress below the yield strength of the material, the total strain on the specimen approaches the Basquin assumption of elastic response. The improved fatigue life and fatigue strength observed in the experimental results is therefore considered significant. The behavior observed is similar to that found in fatigue of aluminum-magnesium alloys with less than 5 wt pct Mg as discussed by Boyapati and Polmear [Ref. 13]. Additionally, the ratio of fatigue strength to yield-strength for this material appears to be about 0.6 which is considerably improved over commercially available high strength aluminum alloys.

The cyclic hardening implied under low cycle fatigue conditions was verified by conducting hardness tests on fatigued and failed specimens. The resulting data is plotted in Figure 22. For comparison, the total range of hardness values and the mean hardness of the material in the as-rolled condition are shown in the cross hatched region of the figure.

A marked increase in hardness is observed when the applied stress amplitude is substantially higher than the 0.2 percent offset yield strength of the material. Decreasing the stress amplitude (increasing the cycles to failure) results in a lower degree of hardening. Beyond 10^4 cycles, hardness values remain within the range of the as-rolled material.

Precipitation is believed to occur under cyclic loading, particularly under low cycle fatigue conditions. Figure 23 shows micrographs of a specimen of Al-10.2 wt pct Mg (oil-quenched from homogenization temperature and warm-rolled at 300°C) which failed after 3300 cycles at an initial stress of 48.5 KSI (334 MPa). The specimen was sectioned and mounted to allow microscopic examination of the long transverse section such that microstructural comparison of the regions adjacent to the main fracture surface and secondary cracks was possible. A dramatic increase in the volume fraction of second phase particles is evident in the regions adjacent to the main fracture surface (Figures 23(a), (b) and (c)) and adjacent to secondary cracks (Figure 23(d)). Bands of second phase particles, forming perpendicular to the stress axis, are clearly evident. The precipitates are 0.5 μm to 1 μm in diameter and it is unlikely that nucleation and growth of second phase particles of this size could occur at room temperature in the run time for this specimen (approximately 1.5 minutes). The most plausable explanation for these coarse, banded second

phase particles is that nucleation and early growth occurs in slip bands during the fatigue test. Subsequent to specimen failure, continued growth at room temperature is enhanced by magnesium diffusion along paths of high dislocation density. Stubbington [Ref. 19] noted similar behavior in an Al-12.5 wt pct Mg alloy subjected to fatigue loading; however, his specimens were tested in torsion and at lower levels of stress amplitude. He observed a fine, homogeneous dispersion of second pahse particles in contrast to the banded structure noted in this study.

Examination of thin foils prepared from the fatigued specimens provides additional evidence that precipitation occurs under low cycle fatigue conditions. Figure 24 shows the microstructure of a specimen which failed after 1200 cycles of fully reversed bending fatigue at a stress amplitude of 55.7 KSI (384 MPa). The foil was prepared to allow viewing the microstructure in a plane parallel to the rolling plane. Thus, the area examined is primarily that of a grain interior adjacent to the fracture surface.

When compared to the microstructures of the as-rolled material shown previously (Figure 16), the dramatic increase in both the number and size of second phase particles present is evident. Again, the short run time involved during the cyclic testing of this specimen does not appear to account for the coarse nature of the precipitates. This suggests that nucleation and early growth has occurred during the

fatigue test and coarsening has probably resulted due to enhanced aging at room temperature as previously explained. The banded appearance of the second phase particles does support the original hypothesis that initial nucleation and early growth occur in slip bands. The cyclic hardening response of the material under low cycle fatigue conditions was observed by traversing the entire length of specimens and taking several hardness readings. The fact that the observed hardness was uniform throughout the specimen indicates that cyclic hardening probably occurs due to the dislocation density increase and not as a result of precipitation.

Some supporting evidence that precipitation occurs under low cycle fatigue conditions was obtained by Scanning Electron Microscopy (SEM) as shown in Figures 25 and 26. Figure 25 is an SEM fractograph of the fracture surface of the Al-10.2 wt pct Mg specimen which failed after 3300 cycles. Stage II crack growth is shown at different levels of magnification. Striations are relatively widely spaced and are well defined. Coarse bands approximately 1 μm wide appear to be lying on the surface perpendicular to the striations. Additionally, finer, more uniform particles lie on the surface. The directional nature of the coarse bands and particularly their size and orientation with respect to the axis of applied stress and direction of crack growth, suggests that they correspond to the coarse bands of secondary phase particles observed in the optical micrographs shown previously. The

more uniformly dispersed, fine particles are believed to correspond to precipitates which may have nucleated during the latter stages of testing and have grown subsequent to the failure.

Figure 26 is an SEM fractograph of the overload region of the same specimen showing a dimpled pattern characteristic of ductile overload failures. Dimples corresponding to voids, believed to be initiated by the presence of both coarse and fine precipitates, are evident. Some smaller precipitates are shown lying on the surface adjacent to the coarse dimples (top center of Figure 26) and within the dimples as well which supports the assumption that void initiation occurs as a result of the presence of second phase particles.

As the stress amplitude is reduced and cycles to failure increase, little indication of microstructural changes could be observed optically. In the intermediate cycle fatigue regime, there was no detectable change in microstructure when comparison is made with the as-rolled optical micrographs (Figure 12).

Figure 27 is a SEM fractograph of the fracture surface of a specimen which failed after 1.81×10^5 cycles with an applied stress amplitude of 33.8 KSI (233 MPa). Both Stage II and Stage III regions of the fracture surface are shown. Crack growth is primarily transgranular with some grain boundary separation. Few indications of precipitate interaction are visible within the striations in Figure 27(a). The

overload region exhibits the appearance of a ductile failure (Figure 27(b)), however, few dimples are present and a high degree of deformation is indicated.

Subsequent tests of the same material under high cycle fatigue conditions again show little or no microstructural changes from the as-rolled condition. This was found to be true in analyzing specimens using standard optical metallographic techniques, Transmission Electron Microscopy and Scanning Electron Microscopy.

Figure 28 demonstrates the characteristic microstructure observed in thin foils of specimens tested in the high cycle fatigue regime. The microstructures shown in Figure 28 are of a specimen of Al-10.2 wt pct Mg alloys (solution treated, oil-quenched and warm-rolled at 300°C) which failed after 4.6×10^6 cycles with an applied stress amplitude of 30 KSI (207 MPa). The microstructure is remarkably similar to that of the as-rolled material shown in Figures 16 and 20(a). The average substructure cell size is approximately 0.33 μm and there is no appreciable increase in the dislocation density.

Figure 29 shows Stage I to Stage II transition of crack growth in a specimen which failed after 7.6×10^6 cycles at a stress amplitude of 31 KSI (214 MPa). Here, some grain boundary separation is apparent. Fracture appearance of the grain interiors in this region is ductile with some dimpling and deformation (crack growth is from right to left in the figure).

Figure 30 shows the Stage II and Stage III crack growth regions of the same specimen. Crack growth is predominately transgranular with some regions of intergranular fracture as well. Striations are well defined and closely spaced (Figure 30(a), consistent with the fatigue life of the specimen. The overload region (Figure 30(b)) appears ductile.

Crack initiation is this alloy appears to be a result of slip band formation which probably occurs through the interaction of pre-existing precipitates near the surface (formed during warm-rolling) with dislocations. These precipitates assist in the formation of slip bands by pinning dislocations as they move under the applied cyclic loads. Under low cycle fatigue conditions, the formation of slip bands will provide energetically favorable nucleation sites for subsequent precipitation to occur and the locally increased volume fraction of second phase particles may accelerate crack propagation rates. As the applied strain (stress amplitude) is reduced and the number of cycles to failure increased, the rate of second phase particle formation is decreased. This is attributable to the reduced amount of dislocation motion during each cycle. Less dislocation tangling occurs offering fewer nucleation sites for precipitation to occur. Under high cycle fatigue conditions, the distances which dislocations travel during each cycle are sufficiently small to create a stable system and little or no increase in the dislocation

density occurs. Thus, slip band formation is more difficult and few new second phase particles form.

The absence of secondary cracks on intermediate and high cycle fatigue specimens indicates that the greatest percentage of the materials life is consumed in crack initiation. Once initiation has occurred, the crack provides its own localized stress riser and subsequent propagation to failure is rapid.

Comparison of the SEM fractographs for the material under low, intermediate and high cycle fatigue conditions (Figures 25-27, 29 and 30) indicates a trend towards an increased degree of grain boundary separation as the number of cycles to failure is increased. Under low cycle fatigue conditions, the stress amplitude is higher than the general yield-strength of the material, and the deformation incurred with each cycle is realtively uniform. Reducing the stress amplitude to a level below the general yield-strength increase the significance of localized microstructural stress concentration. The highly angular precipitates which form (during warm-rolling) are mostly found in the grain boundaries. The grain boundary precipitates are believed to provide localized stress concentrations which then allow the grain boundary to fracture at lower stress amplitudes.

2. Al-10.2 wt pct Mg Solution Treated Water-Quenched and Warm-Rolled at 300°C

Figure 31 shows the experimental results obtained from the fatigue testing conducted on the Al-10.2 wt pct Mg

alloy solution treated, water-quenched and warm-rolled at 300°C. The Basquin prediction is included for comparison. The response of the alloy when water-quenched from homogenization temperature in contrast to the same alloy in the oil-quenched condition (Figure 21), implies that the cooling rate from solution treatment can have a significant effect on the fatigue behavior of the material.

Cyclic hardening appears to occur as indicated by the improved fatigue life observed in the experimental results in contrast to the predicted response. The subtle difference between the fatigue life observed in the water-quenched material as apposed to the oil-quenched implies that hardening may occur to a lesser extent in the water-quenched condition. Due to the high degree of scatter between data points often encountered in fatigue testing, this observation in itself was not considered particularly significant.

The high cycle fatigue response is improved over the Basquin prediction but to a lesser extent than that of the oil-quenched material (Figure 21). This too, could be attributed to scatter between data points and was noted as a possible trend to watch for during the remainder of the study.

The experimental results imply that an endurance limit may exist beyond 10^7 cycles at an applied stress amplitude of about 22 KSI (152 MPa). This would result in a fatigue strength to yield stress ratio of about 0.48 which is comparable

to fatigue strength to yield stress ratios observed in the 5000 series aluminum-magnesium alloys [Ref. 13].

Hardness tests conducted on the fatigued specimens verify that cyclic hardening does occur in samples tested with stress amplitudes in excess of the yield stress as shown in Figure 32. The subtle difference between the apparent levels of hardening between the oil-quenched and water-quenched materials described earlier, gains significance when the hardness results shown in Figures 22 and 32 are compared. Hardening does appear to be more pronounced in the oil-quenched material. This may be expected to occur in a material in which the solute atom concentration in solution has been reduced through segregation and precipitation on quenching. As explained previously, the decreased solute atom concentration is believed to be the most significant factor in accounting for the larger substructure cell size found in the oil-quenched material. The coarser microstructure would then be expected to harden under cyclic loading to a relatively greater extent.

As in the oil-quenched condition, an increased volume fraction of second phase particles were found to exist in the low cycle fatigue specimens of the Al-10.2 wt pct Mg alloy solution treated, water-quenched and warm-rolled at 300°C. Figure 33 shows the bonded nature of precipitate formation adjacent to the main fracture surface (Figure 33(a)) and adjacent to the secondary cracks (Figures 33(b), (c) and (d)). The specimen failed after 3400 cycles of fully reversed

bending fatigue at an applied stress amplitude of 49.9 KSI (344 MPa). The appearance of regions adjacent to the main fracture surface and secondary cracks shown in Figures 33 resembles the microstructures presented earlier of similar regions in oil-quenched material (Figure 23). One subtle difference between the two groups of figures is apparent on close comparison. Precipitation appears to be less pronounced in the water-quenched material (Figure 33). This is particularly evident in the regions adjacent to the main fracture surface. This feature may be linked in some way to differing levels of solute atom concentration caused by the varied rates of quench from solution treatment, however, at this point, this is only speculation. As mentioned previously, it is unlikely that second phase particles of this size would nucleate and grow to this extent during the limited run time for the specimen. Coarsening is probably a result of accelerated aging response at room temperatures due to the highly dislocated microstructure.

Figure 34 shows transmission electron micrographs from thin foils prepared utilizing the specimen which failed after 3400 cycles. A greater number of precipitates is present in comparison to the as-rolled condition shown previously in Figures 17 and 20. Additionally, comparison of the TEM micrographs in Figure 34 with those of the low cycle fatigued, oil-quenched specimen (Figure 24), implies that less precipitation has occurred in the water-quenched material.

Recognizing that TEM observations made from foils of aluminum alloys may be strongly dependent upon several factors, including the location within the specimen from which the foil is taken, the plane from which the foil is cut, polishing conditions and the wide variety of artifacts which may appear, the observation that perhaps second phase particle formation has occurred to a reduced extent under the stated conditons is not considered to be conclusively supported.

Figure 35 is an SEM fractograph of the fracture surface of a specimen which failed after 2000 cycles of fully reversed bending fatigue at a stress amplitude of 55 KSI (379 MPa). Both Stage II and Stage III regions of the surface are shown.

Striations are widely spaced (Figure 35(a)) and there is little evidence of void initiation having occurred within the Stage II fracture region. The overload region is that of a relatively low energy fracture with small, finely dispersed dimples (Figure 35(b)). Several regions of intergranular failure are evident but the surface is primarily that of a transgranular fracture. Both coarse and fine dimples are present and are believed to correspond to the precipitate dispersion in the water-quenched material with the second phase particles acting as void initiation sites. If this is true, comparison of Figure 35(b) and Figure 26 may be representative of contrasts in the microstructures of the water-quenched and oil-quenched conditions respectively. Furthermore, if the dimples originate as a result of void

formation and coallescence, then the apparent absence of precipitates indicated in Figure 35(a) implies that second phase particles are perhaps more easily fractured and afford little resistance to Stage II crack growth in the water-quenched material.

As in the oil-quenched condition, little evidence of microstructural changes occurring through conditions of intermediate and high cycle fatigue loadings could be found through optical metallographic techniques. Few secondary cracks were found to be nucleated and no evidence of an increase in the volume fraction of second phase particles was found.

Figure 36 is a SEM fractograph of a sample which failed after 10600 cycles at an applied stress amplitude of 40.1 KSI (276.5 MPa). Void formation is apparent in the striated regions with both coarse and fine voids clearly defined (Figure 36(a)). Transgranular and intergranular growth is indicated. The overload region (Figure 36(b) also indicates a heavily dimpled pattern with regions of intergranular growth clearly defined. The dimpled appearance of the Stage II and Stage III regions of the surface give the impression that, in this instance, crack growth has followed a region of material in which the precipitate volume fraction is comparatively large with respect to the rest of the material.

Examination of the microstructures of high cycle fatigue specimens utilizing transmission electron microscopy does reveal some microstructural dissimilarities when compared

to the microstructures observed in the as-rolled conditon (Figures 17 and 20(b)). Figure 37 presents the microstructures observed from two foils cut from different sections of a sample which failed after 4.2 x 10^6 cycles at an applied stress amplitude of 21.2 KSI (146 MPa). Figures 37(a) and 37(b) are views of the same region and same magnification but tilted differently to show the heavily increased dislocation density observed in the high cycle fatigue foils from this material. Figure 37(c) is a foil taken from a different region of the specimen and also expresses an increased dislocation density over the microstructures observed for the as-rolled material. Also evident are regions which appear relatively dislocation free. This is shown in Figure 37(a) and (b), which are tilted to achieve different beam diffraction conditions to verify the presence or absence of dislocations. A similar effect is present in Figure 37(c). Of possible merit is the fact that a subtle difference in the fatigue response between the oil-quenched material and the water-quenched material on a microstructural level is apparent. The trend between the improved behavior of oil-quenched material over the water-quenched alloy, in terms of high cycle fatigue strength and fatigue life gains some significance. This trend was noted earlier in discussing the experimental results of the water-quenched material and some degree of speculation was necessary due to the possibility of scatter involved in conducting the tests. With the additional evidence of existing microstructural

differences between the alloy when quenched in different mediums and tested under similar conditons, noting the trend appears more valid.

Figure 38 shows the fracture surface of the sample which failed at 4.2 x 10^6 cycles as viewed using scanning electron microscopy. Both Stage II and Stage III regions of the fracture surface are shown.

Figure 38(a) shows Stage II crack growth with finely spaced striations. Both transgranular and intergranular growth are indicated. Figure (38(b) shows the overload region with some dimples and some grain boundary separation. The fracture appears to be that of a low energy, ductile failure.

It is appropriate to note that the Al-10.2 wt pct Mg alloy solution treated, water-quenched and warm-rolled at 300°C follows the trend toward an increased amount of grain boundary separation and intergranular crack growth as fatigue life is increased. This same trend was noted earlier in the discussion of the characteristics of the same alloy oil-quenched from the homogenization temperature.

3. Al-8.14 wt pct Mg-0.40 wt pct Cu Solution Treated, Oil-Quenched and Warm-Rolled at 300°C

Figure 39 shows the experimental results obtained from the fatigue testing conducted on the Al-8.14 wt pct Mg-0.40 wt pct Cu alloy, solution treated, oil-quenched and warm-rolled at 300°C. The Basquin prediction is included for comparison.

Cyclic hardening appears to occur, and to a similar extent as with the Al-10.2 wt pct Mg alloy in the water-quenched

condition. However, hardness readings taken on fatigued specimens remained within the range of hardness obtained in the as-rolled conditions (71-78 R_B with a mean hardness of 75 R_B). This facet of the cyclic behavior is in direct conflict with the binary alloy discussed previously. The degree to which the nonuniform alloying element distribution is affecting the behavior of the ternary alloy is not known. It is speculated that either the hardness remains constant under testing conditions as in the case of an overaged material, or that the hardness response is similar to that of an alloy containing precipitates which are easily cut. In the latter case, the hardness may be expected to increase rapidly to some peak value and then gradually decrease under cyclic loading. The study of both conditions is attributed to Calabrese and Laird [Ref. 30].

The high cycle fatigue response is also improved over the Basquin prediction and suggests the existence of an endurance limit beyond 10^7 cycles with an associated stress amplitude of about 22 KSI (152 MPa). This corresponds to a fatigue strength to yield stress ratio of about 0.44 which again is comparable to that of the 5000 series alloys.

As in the previously discussed fatigue tests, an increased volume fraction of second phase particles appears to exist adjacent to the main fracture surface and secondary cracks of low cycle fatigued specimens of the Al-8.14 wt pct Mg-0.40 wt pct Cu alloy (in the oil-quenched condition).

This is shown in Figure 40 which presents micrographs of a specimen which failed after 1400 cycles of fully reversed bending fatigue at an applied stress amplitude of 46 KSI (317 MPa). Banding of precipitates adjacent to the main fracture (Figure 40(a) and (b)), and adjacent to secondary cracks (Figures 40(c) and (d)) is evident. Again, precipitates are believed to nucleate in slip bands under cyclic loading with growth occurring subsequent to the specimen failure.

Figure 41 shows SEM fractographs of the Stage II region (Figure 41(a)), and Stage III regions (Figure 41(b)) of the fracture surface of the specimen which failed after 1400 cycles. Striations are widely spaced consistent with the high stress amplitude and large degree of crack growth per cycle. The overload region exhibits well defined coarse and fine dimples characteristic of a high energy ductile failure. Crack growth in both stages is primarily transgranular with some regions of intergranular growth indicated as secondary cracks on adjacent planes linked with the main growth front.

In concert with the binary alloys response, little evidence of microstructural changes occurring under higher cycle conditions was detectable utilizing optical metallographic techniques. Few secondary cracks were found to be initiated in the specimens failing beyond 10^4 cycles and changes in the volume fraction of second phase particles were not observed.

Figure 42 shows Stage II and Stage III regions of fatigue crack growth (a and b, respectively) of a sample that failed after 110200 cycles with an applied stress amplitude of 30 KSI (207 MPa). Striations are more closely spaced and some grain boundary separation is evident as the front grows from one grain to the next in Stage II (Figure 41(a)). The overload region is dimpled with precipitates acting as void initiation sites (Figure 41(b)). The fracture path is primarily transgranular with some intergranular growth occurring as the front crosses the grain boundaries. The deep dimples correspond to a relatively high energy ductile failure in Stage III.

Decreasing the stress amplitude to below 25 KSI (172 MPa) produced run times on specimens substantially in excess of 10^7 cycles while levels above 25 KSI resulted in failure within the intermediate cycle fatigue regime. This suggests that an endurance limit exists at a stress amplitude in the neighborhood of 22 KSI (152 MPa). Figure 43 shows the small microscopic cracks which originated at corners and were visible at a magnification of 200x using an optical microscope. This is the only evidence of fatigue damage under such low stress, high cycle fatigue loading (23 KSI (157 MPa)). The cracks appear at 45° to the applied tensile component of stress.

4. Al-8.14 wt pct Mg-0.40 wt pct Cu Solution Treated, Water-Quenched and Warm-Rolled at 300°C

Figure 44 shows the experimental results obtained from the fatigue testing conducted on the Al-8.14 wt pct Mg -0.40 wt pct Cu alloy solution treated, water-quenched and warm-rolled at 300°C. The material appears to cyclically harden, but as in the case of the oil-quenched alloy, hardness readings taken on the fatigued specimens fail to verify the range of values obtained on the as-rolled material (75 R_B to 82 R_B with a mean hardness of 80 R_B). As before, this feature conflicts with the behavior of the binary alloy and the degree to which the nonuniform alloying element distribution is affecting the behavior is not inown. The speculative comments made previously concerning the possible behavior apply here as well and are based on the studies conducted by Calabrese and Laird [Ref. 30].

In contrast to the previous discussions, the high cycle fatigue response seems more closely to approach the predicted response curve. Under conditions of high cycle loading, the Basquin prediction is more accurate and this observation may be considered significant despite the relative effects of scatter often encountered in conducting fatigue tests.

Increased volume fractions of second phase particles appear adjacent to the main fracture surfaces and adjacent to the secondary cracks in specimens tested under low cycle fatigue conditions. This is shown in Figure 45 which presents

optical micrographs of regions adjacent to the main fracture surface (Figures 45(a) and (b) and to secondary cracks (Figures 45(c) and (d)). The microstructures presented are from a sample that failed after 2700 cycles with an applied stress amplitude of 43.1 KSI (297 MPa). An increased volume fraction of second phase particles is notable adjacent to the main fracture path (Figures 45(a) and (b)) and the banded aspect in which they form is also apparent. This is also shown, but to a lesser extent, at the blunt tip of the secondary crack shown in Figure 45(c). Figure 45(d) indicates a sharp edged secondary crack with the banded second phase particles forming adjacent to the crack and ahead of the crack tip.

Figure 46 shows Stage II and Stage III crack growth for the same specimen. The striations indicated in Figure 46(a) are widely spaced and the fracture appearance suggest some interaction between the growing crack front and the precipitates has taken place. Within the striations, precipitates are found to be lying on the surface and the striations give the appearance that the crack front has looped around precipitates which were retained on the mating fracture surface subsequent to failure. Figure 46(b) shows the overload region with elongated dimples corresponding to voids which have initiated as a result of the presence of second phase particles. Some grain boundary separation is apparent although the fracture surface is predominately transgranular.

As in the previous cases, microstructural changes could not be observed optically as the loading conditions were altered from those of low cycle fatigue to those of longer fatigue lives.

Figure 47 shows SEM fractographs of a specimen that failed after 13.4 x 10^4 cycles with a stress amplitude of 24.5 KSI (169 MPa). Stage II fracture appearance (Figure 47(a)) shows more closely spaced striations than those shown in Fgire 46 which is consistent with the decreased stress amplitude. A similar interaction between the growth of the crack front and the second phase particles to that noted in the low cycle fatigue specimen is apparent. The overload region shown in Figure 47(b) is that of a ductile failure with a large degree of deformation. Some fine dimples are visible on close observation and secondary crack paths are also notable as the main crack altered its direction to accomodate the second phase particles.

Figure 48 shows the resulting fracture surface of a specimen that failed after 4.8 x 10^6 cycles with an applied stress amplitude of 15.5 KSI (107 MPa). Both Stage II and Stage III regions of the surface are shown (Figures 48(a) and (b) respectively). Stage II fracture appearance exhibits more closely spaced striations, again with some evidence of possible interaction between the growing crack front and second phase particles. The overload region exhibits a ductile appearance with some dimpling and a high degree of

secondary growth paths occurring as the crack propagates to failure.

D. GENERAL DISCUSSION

It should be noted again that study of the fatigue response of any alloy system is difficult. The characteristics must be documented and verified through studies in which the material is tested utilizing different testing modes and specimen designs to ensure that documented trends are consistent. Only when studied in this manner does the data become useful from a design standpoint. This feature has been noted previously by Mondolfo [Ref. 17] in commenting on Al-Zn-Mg alloys. Verification studies are also necessary in order to adequately account for the wide degree of scatter in data encountered in fatigue testing. This study represents a first analysis of the fatigue behavior of warm-rolled high-magnesium aluminum-magnesium alloys and will require additional effort and verification of the trends noted.

The tensile behavior of the alloy in the oil-quenched condition supports the findings of Johnson [Ref. 7]. However, the microstructural analysis conducted during the coarse of this experiment shows the primary strengthening mechanism to be the diffuse dislocation substructure developed during warm-rolling. This contradicts the results of preceding efforts [Refs. 1-7] and is based upon the microstructural evidence obtained through transmission electron microscopy.

Precipitates are non-uniformely dispersed and the system favors the formation of coarse particles rather than uniformly

dispersed fine particles. The diffuse dislocation cell structure of the alloy in the oil-quenched condition appears to exhibit an average cell diameter of about 0.33 μm, with the intersections of cell walls acting as nucleation sites for second phase particle formation. As the particles nucleate and grow, the local dislocation density adjacent to them appears to decrease and in that sense, second phase particle formation seems to be a recovery event.

The observed microstructure shows the alloy to be a solid solution, work hardenable material and the tensile response is very similar to that of the 5000 series alloys (which are classified as work hardenable alloys) [Ref. 13]. Serrated yielding is apparent, as with other solid solution alloys, and the yield strength and ultimate tensile strength are considerably higher than those observed in the 5000 series aluminum-magnesium alloys.

It should be noted that aluminum alloys in general offer a challenge in accomplishing TEM analysis of the microstructure. The appearance of artifacts, the plane from which the foils are taken, the polishing procedure and the tendency for uneven thinning due to varying alloying element concentrations or seond phase particles can grossly affect the observed microstructures. In analyzing the microstructure during the coarse of this study, the plate thickness of the materials dictated that foils be prepared from a plane parallel to the rolling plane due to the polishing procedure utilized. In this

respect, additional information concerning the grain boundary regions was not detectable to any degree of certainty. Additionally, the precipitates formed were larger than the foil thickness by several times and showed a strong tendency to be washed out during the thinning process. This left a region which was thinned to a greater extent outlining the site originally occupied by precipitates. Justification was accomplished by examining foils of materials which were taken in the as-quenched and the quenched and artificially aged conditions to verify the precipitate morphology. These microstructures were shown previously in Figures 18 and 19.

Additional TEM analysis of foils taken from long transverse and short transverse planes will be worth while and provide a better understanding of the microstructure.

The fatigue response of the Al-10.2 wt pct Mg alloy solution treated, oil-quenched and warm-rolled at 300°C follows the trends of solid solution, work hardened alloys [Ref. 30]. The material cyclic hardens under high stress amplitude loading conditions to a substantial degree and appears to exhibit an endurance limit beyond 10^7 cycles with a fatigue strength to yield stress ratio in excess of 0.6. This also is characteristic of solid solution, work hardened alloys as stated by Boyapati and Polmear [Ref. 13].

Water-quenching the Al-10.2 wt pct Mg alloy from homogenization and then processing it in similar fashion seems to result in refinement of the microstructure with respect to

the substructure developed during warm-rolling. The average cell diameter within the substructure is on the order of 0.1 µm (as opposed to 0.33 µm using the slower rate of quench). The microstructural refinement provides a slight increase in the observed ultimate tensile strengths and ductility of the material. Ordinarily, refining the substructure by a factor of three may be expected to provide a greater strengthening effect and a more marked increase in ductility than was observed. In the Hall-Petch relationship [Ref. 31]

$$\sigma_y = \sigma_o + K_y d^{-1/2} \qquad (6)$$

the contribution of K_y for a face center cubic material is less than for a body center cubic material. Therefore, the effects of grain size (or substructure) are more subtle from a strengthening standpoint.

Water-quenching the alloy appears to have an adverse effect on the fatigue behavior of the alloy. The degree to which the material was found to cyclically harden is somewhat reduced and the fatigue strength to yield stress ratio was also reduced to about 0.48. This is thought to be related to the decreased strains required to achieve increased dislocation tangling within the refined substructure. In this sense, slip band formation becomes easier and the fatigue response is degraded as bbserved. As stressed earlier, this bears further analysis and verification.

It is difficult to make conclusive arguments as to the effects of copper within the system on the tensile behavior

and on the fatigue behavior of the alloy. As explained earlier, analysis of the cause for the materials resistance to being deformed under warm-rolling conditions indicated that a nonuniform alloying element distribution may have contributed to the problem. The effects of this nonuniform condition on the overall properties of the alloy are not known and will bear subsequent study.

The purpose of the copper addition is to provide refinement of the microstructure. Based on the work of Boyapati and Palmear [Ref. 13], additional study as to the proper amount of refining element addition and the correct solution treatment is warranted. Boyapati and Palmear worked with an Al-5 wt pct Mg alloy and studied the effects of varying amounts of silver (a refining element) on the microstructure and the fatigue response of the material. Due to the similarities in general effects realized by the addition of copper to aluminum-magnesium alloys as discussed by Mondolfo [Ref. 16] some benefit may be realized by conducting a study of that nature.

V: CONCLUSIONS AND RECOMMENDATIONS

A. CONCLUSIONS

As stated previously, the objectives of this research was to provide an initial characterization of the fatigue response of high-magnesium aluminum-magnesium alloys when processed utilizing Johnson's [Ref. 7] standardized thermomechanical process. Analysis was carried out emphasizing the microstructural changes which occur under cyclic loading conditions. The goals of the study have been attained; however, subsequent study in this area is warranted in order adequately to insure the accuracy of the trends noted with respect to the behavior of these alloys under fatigue loading.

The primary strengthening mechanism within the Al-10.2 wt pct. Mg alloy system was determined to be the dislocation substructure developed in these materials under warm-rolling. Preceding work [Refs. 1-7] suggested that the strengthening mechanism was a uniform dispersion of fine precipitates within the base material. Conversly, the observed microstructure throughout this study was that of a solid solution, work hardenable material in which the precipitates are relatively coarse, nonuniformly dispersed, and hence offer little from a strengthening standpoint.

The fatigue behavior of the Al-10.2 wt pct Mg alloy, when oil-quenched from homogenization temperature and then

subsequently warm-rolled to final plate thickness, was found closely to resemble the behavior of the 5000 series alloys. It appears to exhibit an endurance limit with a fatigue-strength to yield-strength ratio in excess of 0.6. When processed in a similar fashion with the quenching medium from solution treatment changed to water, the alloy appears to exhibit a somewhat degraded response. In this condition, the fatigue-strength to yield-strength ratio was reduced to 0.48. Cyclic hardening was observed to occur in both conditions where the materials were loaded at stress amplitudes in excesss of the yield-strength. Again, the more rapidly quenched material appears to cyclically harden to a lesser degree.

Quenching the Al-10.2 wt pct Mg alloy more rapidly from homogenization temperature appears to result in a more refined microstructure upon completion of warm-rolling. The average cell size of the dislocation substructure was reduced by a factor of three as compared to the substructure of the oil quenched material. The slightly improved strength and ductility observed in the water-quenched material is attributed to the observed microstructural refinement.

It is difficult to make conclusive comments on the behavior of the Al-8.14 wt pct Mg-0.40 wt pct Cu alloy due to the nonuniform alloying element distribution within the material when quenched from homogenization temperature. The degree to which the nonuniform distribution effects the response of this alloy is not known except that trends similar to those

noted with the 10 wt pct magnesium alloy were noted in this system with respect to the rate of quench from solution treatment.

Accurate determination of microstructural effects within these alloys requires the support of optical metallographic techniques with scanning electron microscopy and transmission electron microscopy. Only at magnifications attainable through the use of transmission electron microscope can changes within the microstructure with respect to the dislocation network be observed.

The high-magnesium aluminum-magnesium alloys show promise with respect to the increased strenth-to-weight ratio and apparently excellent fatigue behavior. Further study of these alloys is warrented and necessary to verify the behavior of the alloys before they can be used commercially.

B. RECOMMENDATIONS

Based upon the results of this study, the following recommendations for subsequent research apply:

1. The standardized thermomechanical process developed by Johnson [Ref. 7] appears to be inadequate with respect to the amount of solution treatment given to those alloys in which microstructural refinement is achieved through alloying. Both the amount of alloying element addition as well as the correct time at homogenization temperature, should be investigated.

2. Verification studies on the fatigue behavior of these alloys should be initiated utilizing different test modes and specimen designs in order to insure the alloys respond as observed in this work. Measurement of crack propagation rates and the effects of spectrum loading with and without hold periods should be included in these studies.

3. Additional microstructural analysis should be conducted utilizing transmission electron microscopy with foils prepared from various planes in order to gain additional knowledge of the microstructure and the regions adjacent to grain boundaries.

4. Corrosion studies involving the susceptibility of the alloys to stress corrosion cracking and to general corrosion are required and have been initiated.

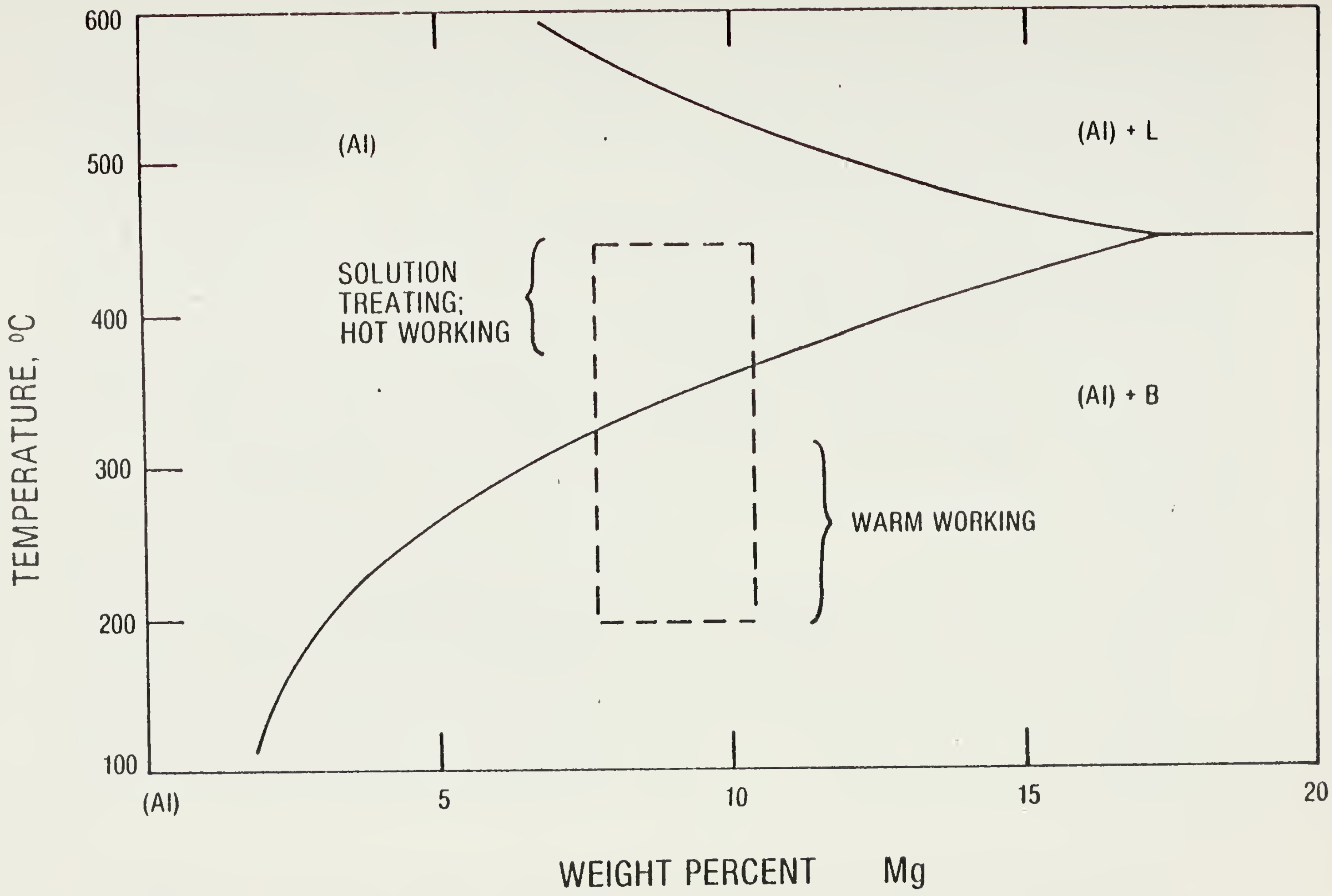

FIGURE 1. Partial Aluminum-Magnesium Phase Diagram.

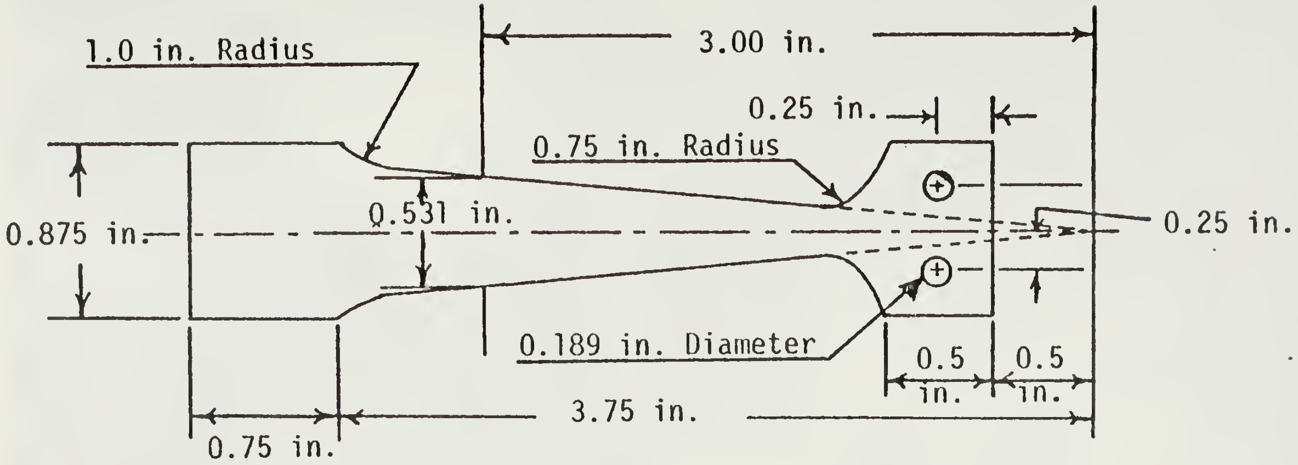

SPECIMEN THICKNESS 0.1 INCHES

FIGURE2. Fatigue Test Specimen Design Utilized for This Study

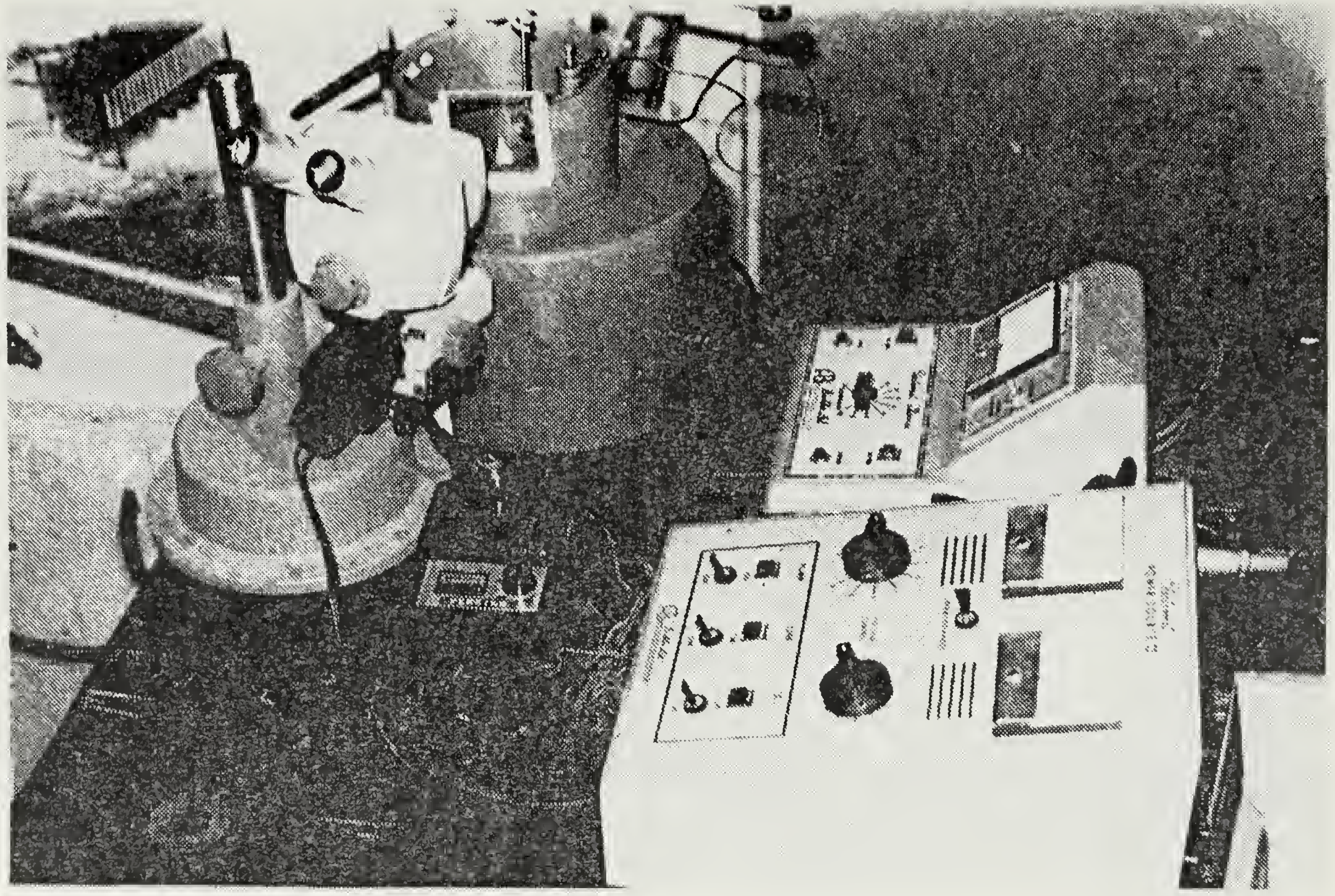

FIGURE 3. Electrolyte Thinning Apparatus Utilized for Thin Foil Preparation (power supplies included)

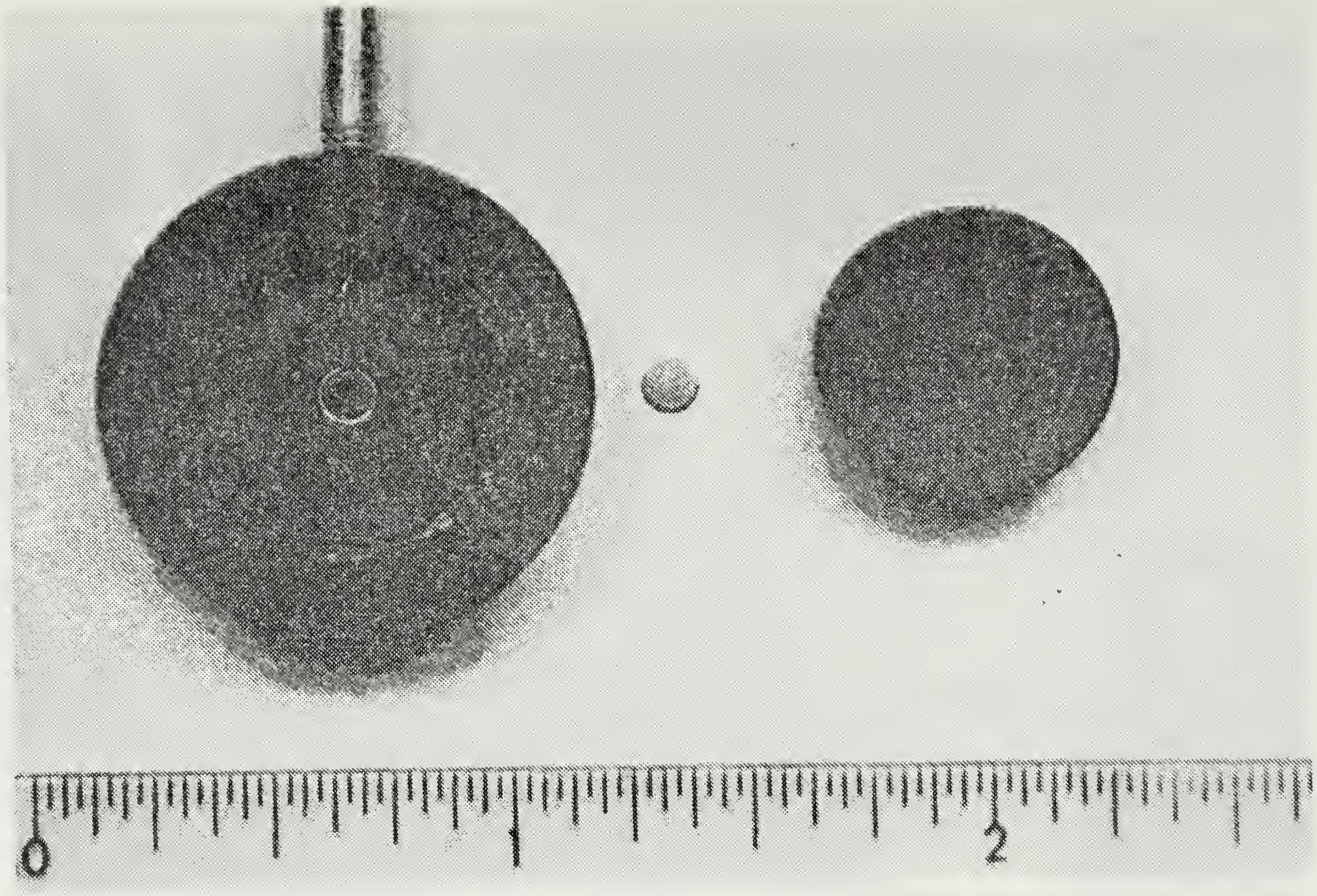

FIGURE 4. Fischione specimen holder, 3 mm disc and plug used in foil preparation

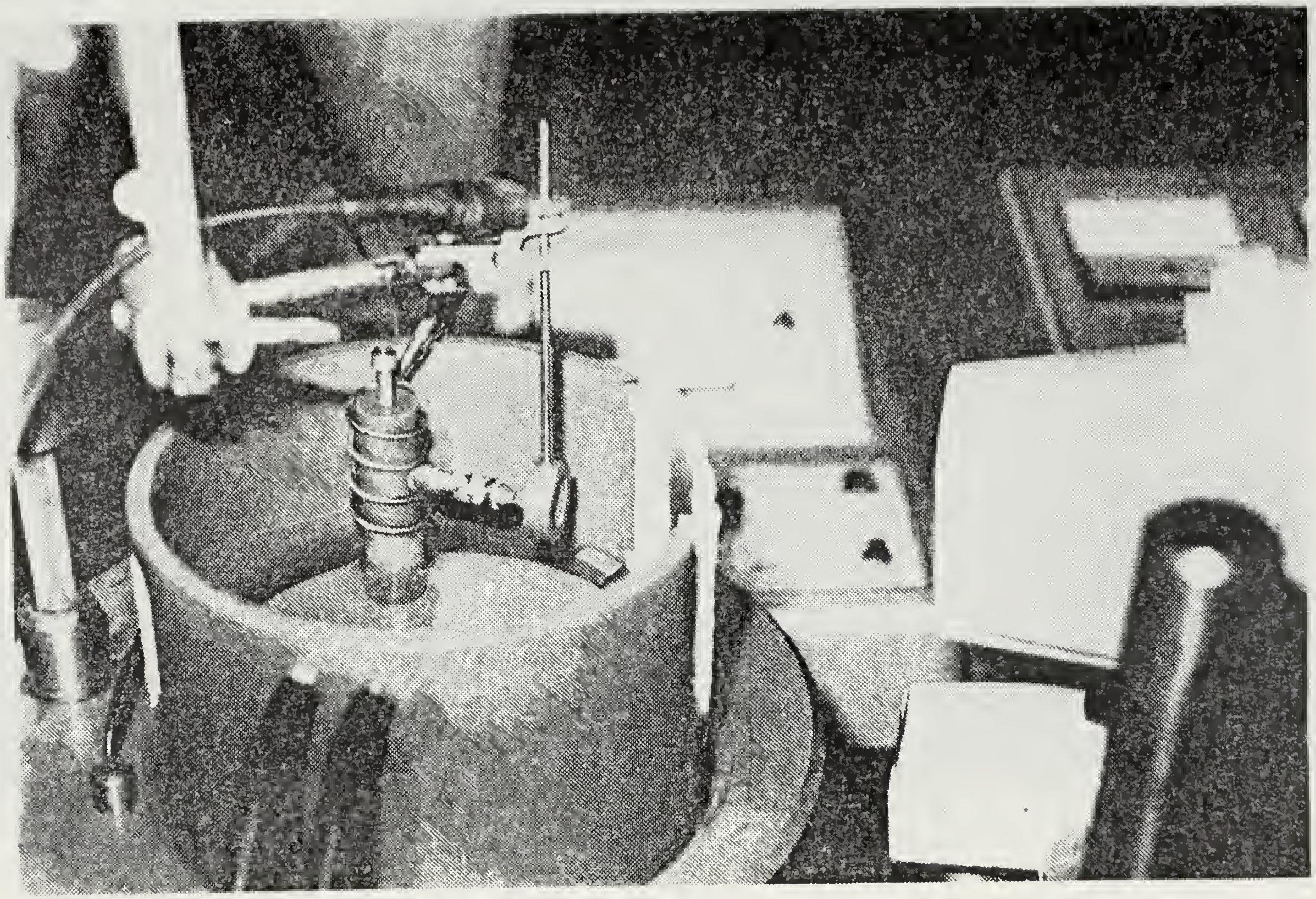

FIGURE 5. Positioning of specimen holder and jet in final preparation for electrolytic thinning of foils

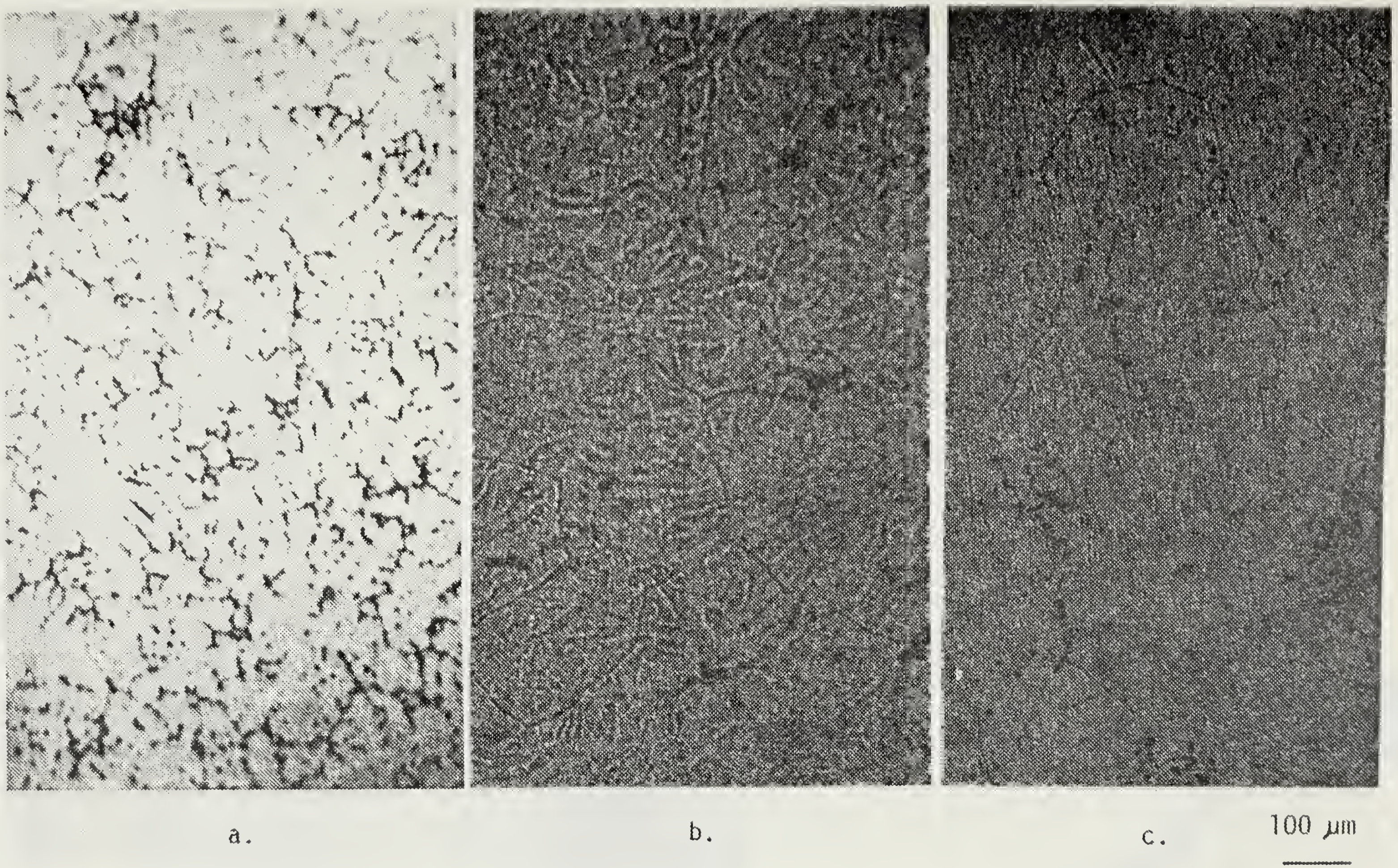

FIGURE 6. Al-8.14 wt pct Mg-0.40 wt pct Cu microstructure: (a) as-cast; (b) solution treated and water-quenched; (c) solution treated and oil-quenched

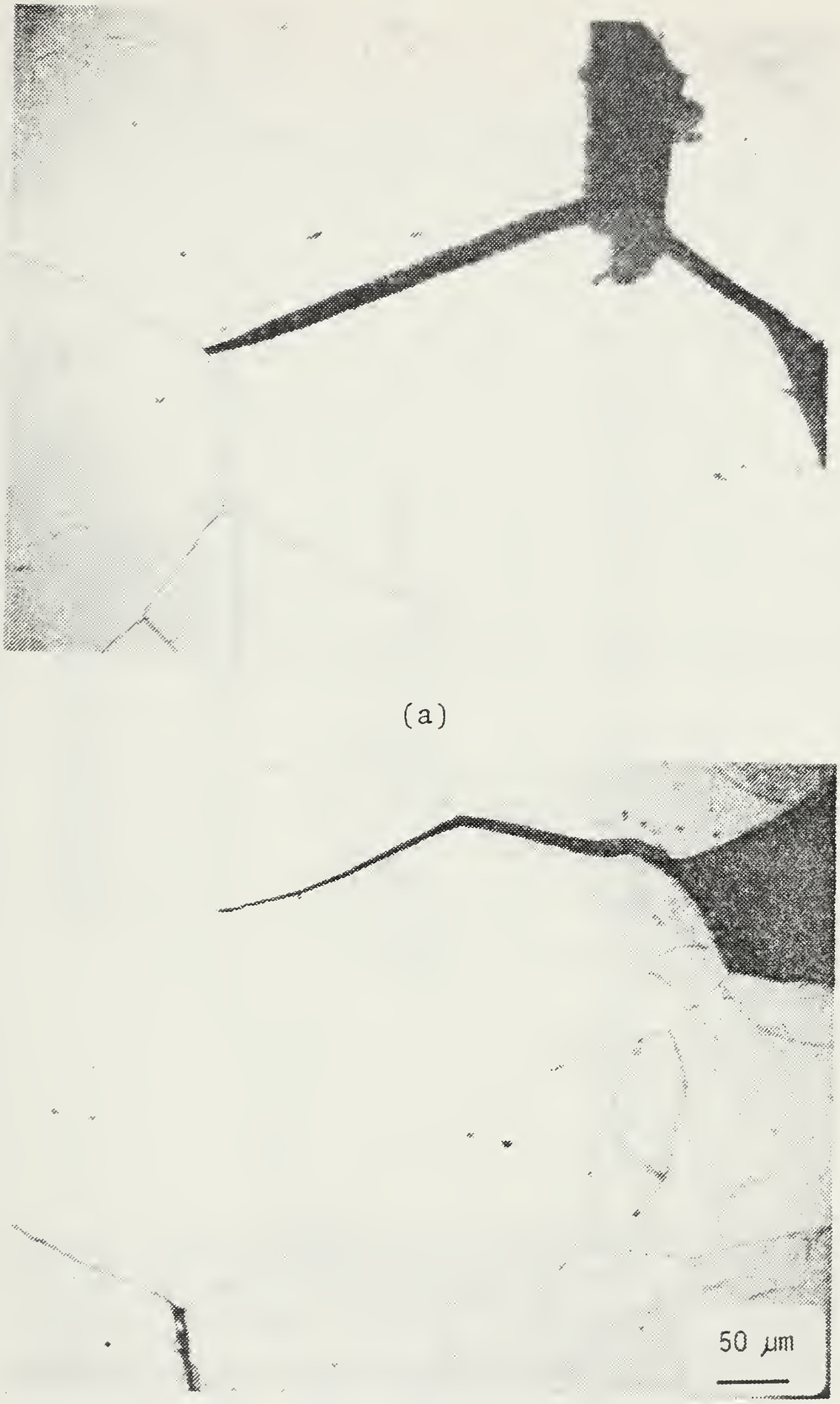

(a)

(b)

FIGURE 7. Regions of intergranular cracking in billets of Al-8.14 wt pct Mg-0.40 wt pct Cu solution treated and water-quenched. Cracking occured in both billets after 2 passes in rolling mill (rolling temperature 300°C)

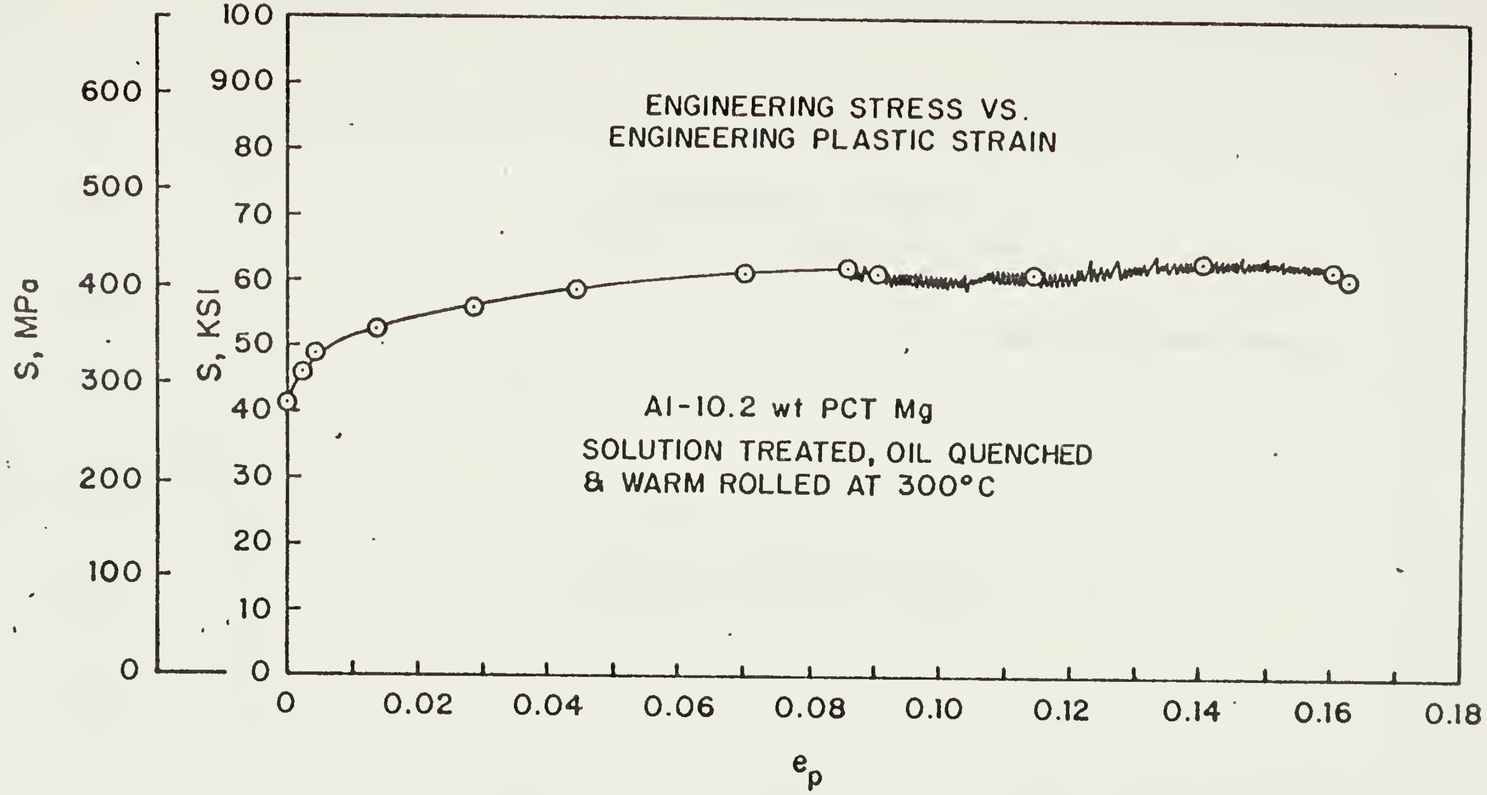

FIGURE 8. Engineering Stress vs Engineering Plastic Strain for Al-10.2 wt pct Mg Solution Treated Oil-Quenched and Warm-Rolled at 300°C

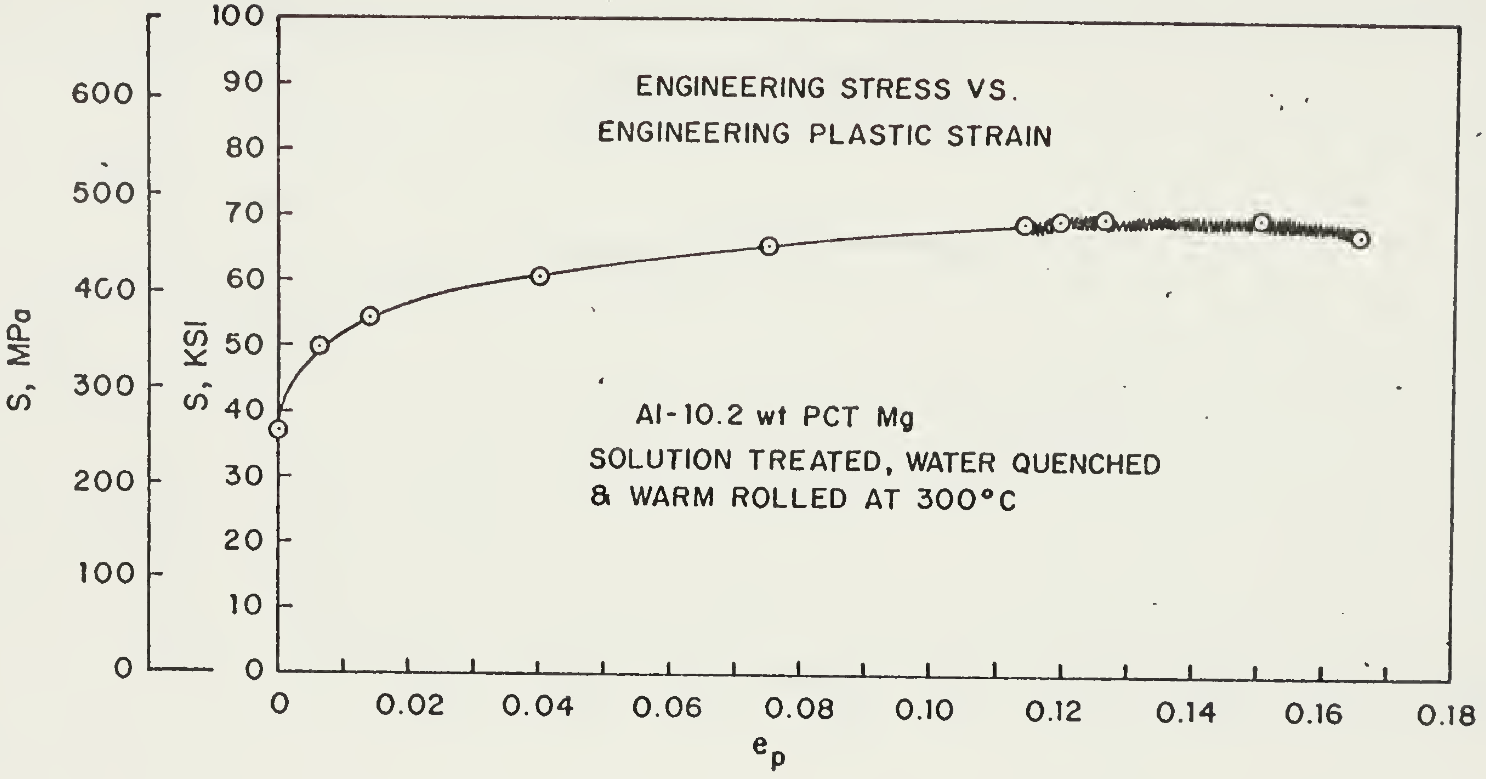

FIGURE 9. Engineering Stress vs Engineering Plastic Strain for Al-10.2 wt pct Mg Solution Treated, Water-Quenched and Warm-Rolled at 300°C

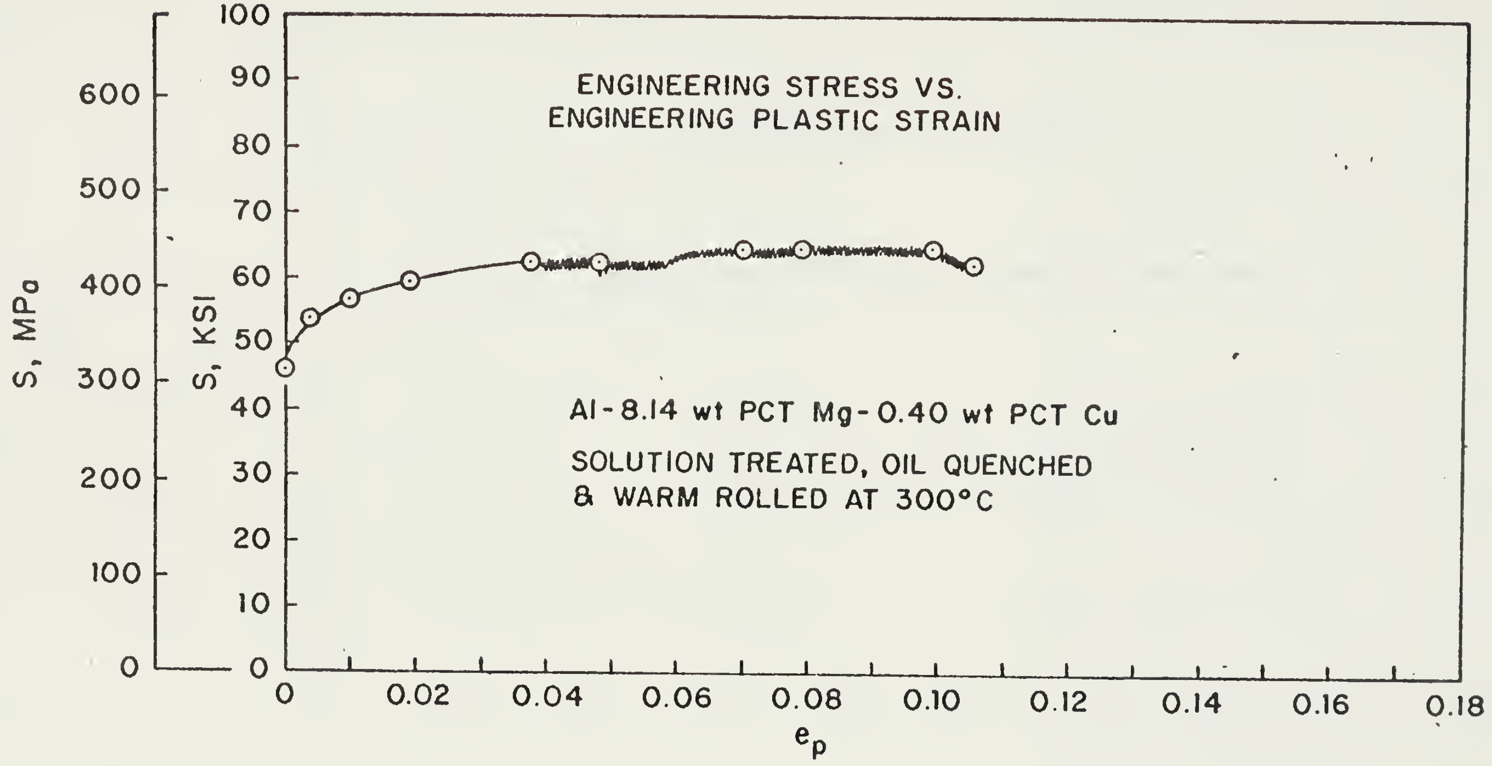

FIGURE 10. Engineering Stress vs Engineering Plastic Strain for Al-8.14 wt pct Mg-0.40 wt pct Cu, Solution Treated, Oil-Quenched and Warm-Rolled at 300°C

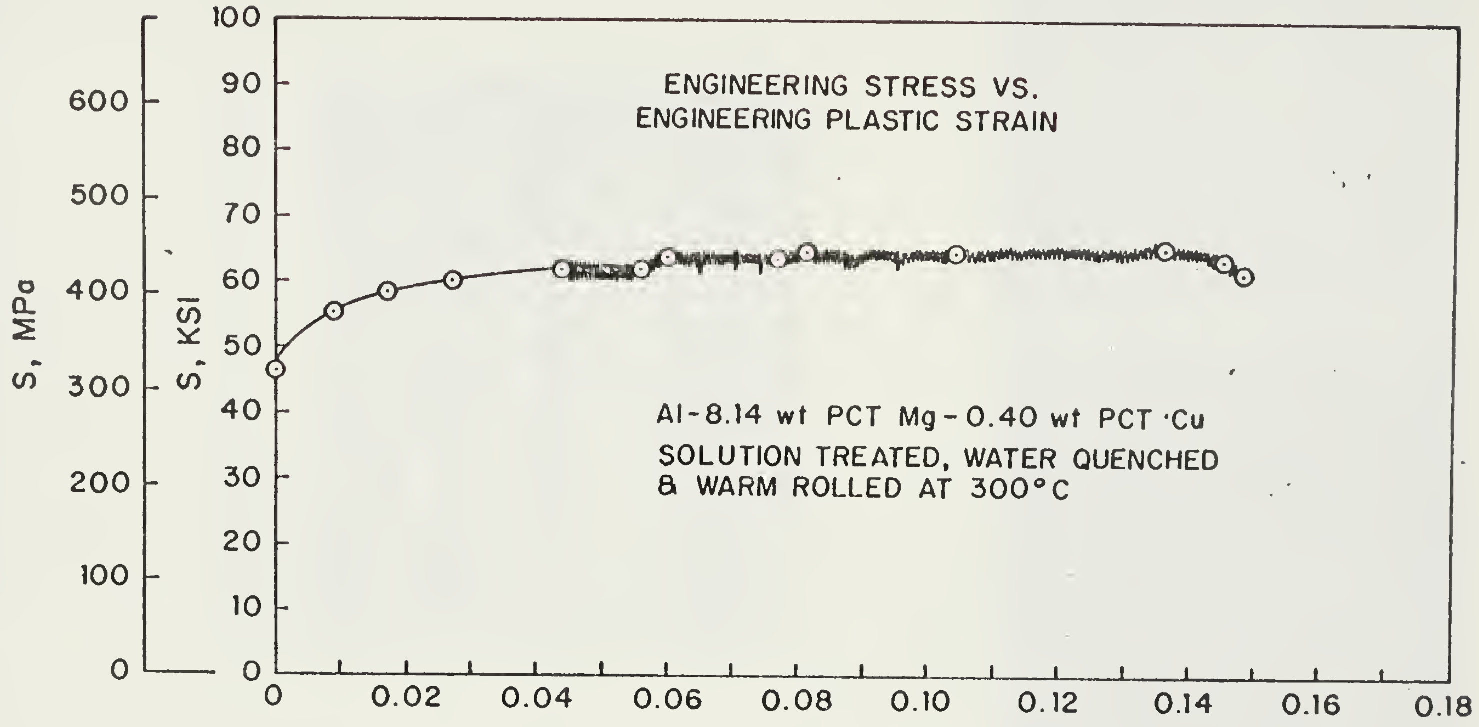

FIGURE 11. Engineering Stress vs Engineering Plastic Strain for Al-8.14 wt pct Mg-0.40 wt pct Cu, Solution Treated, Water-Quenched and Warm-Rolled at 300°C

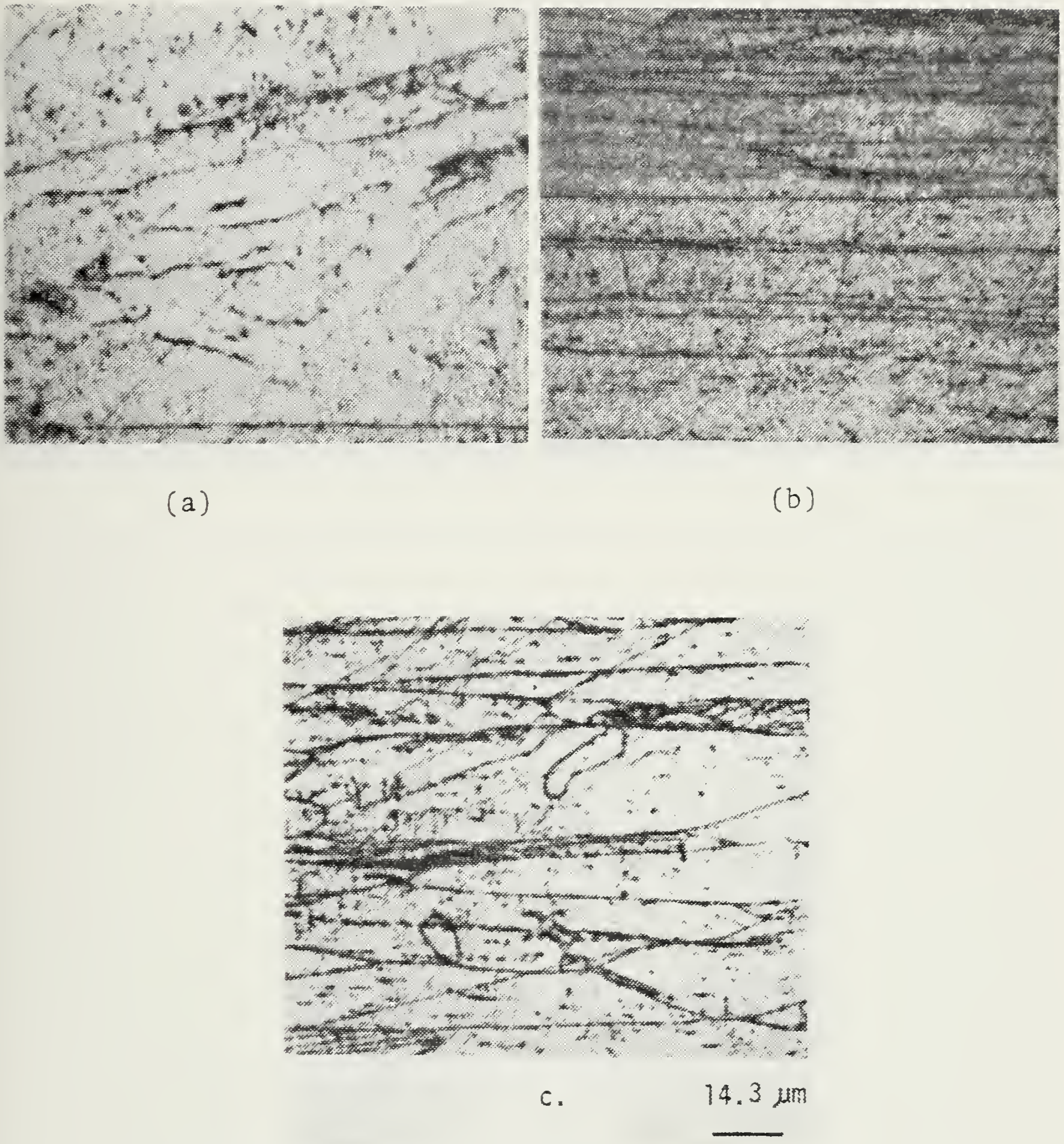

(a) (b)

c.

FIGURE 12. Optical micrographs of the Al-10.2 wt pct Mg alloy, oil-quenched from homogenization: (a) longitudinal; (b) long transverse; (c) short transverse

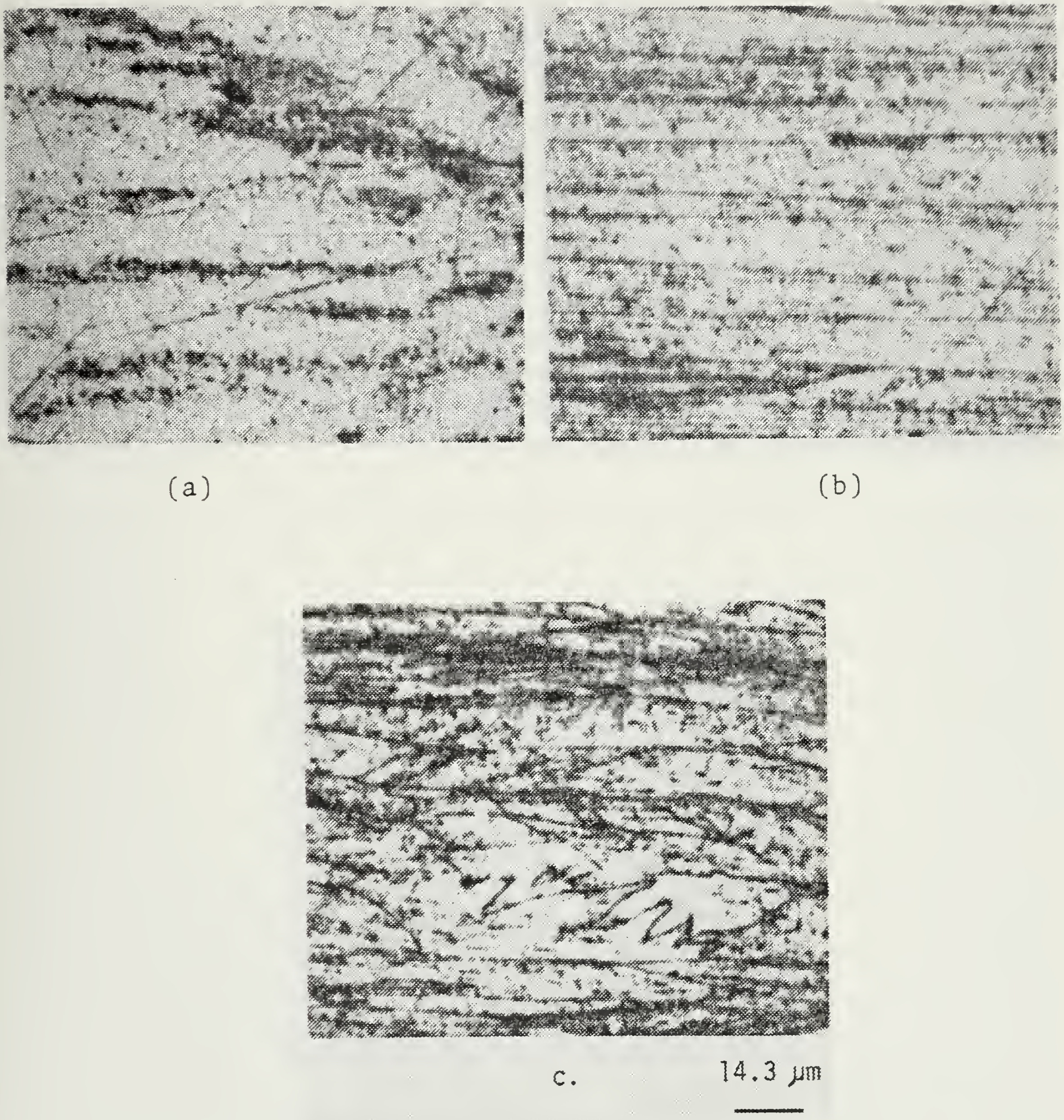

(a) (b)

c.

FIGURE 13. Optical micrographs of the Al-10.2 wt pct Mg alloy, water-quenched from homogenization: (a) longitudinal; (b) long transverse; (c) short transverse

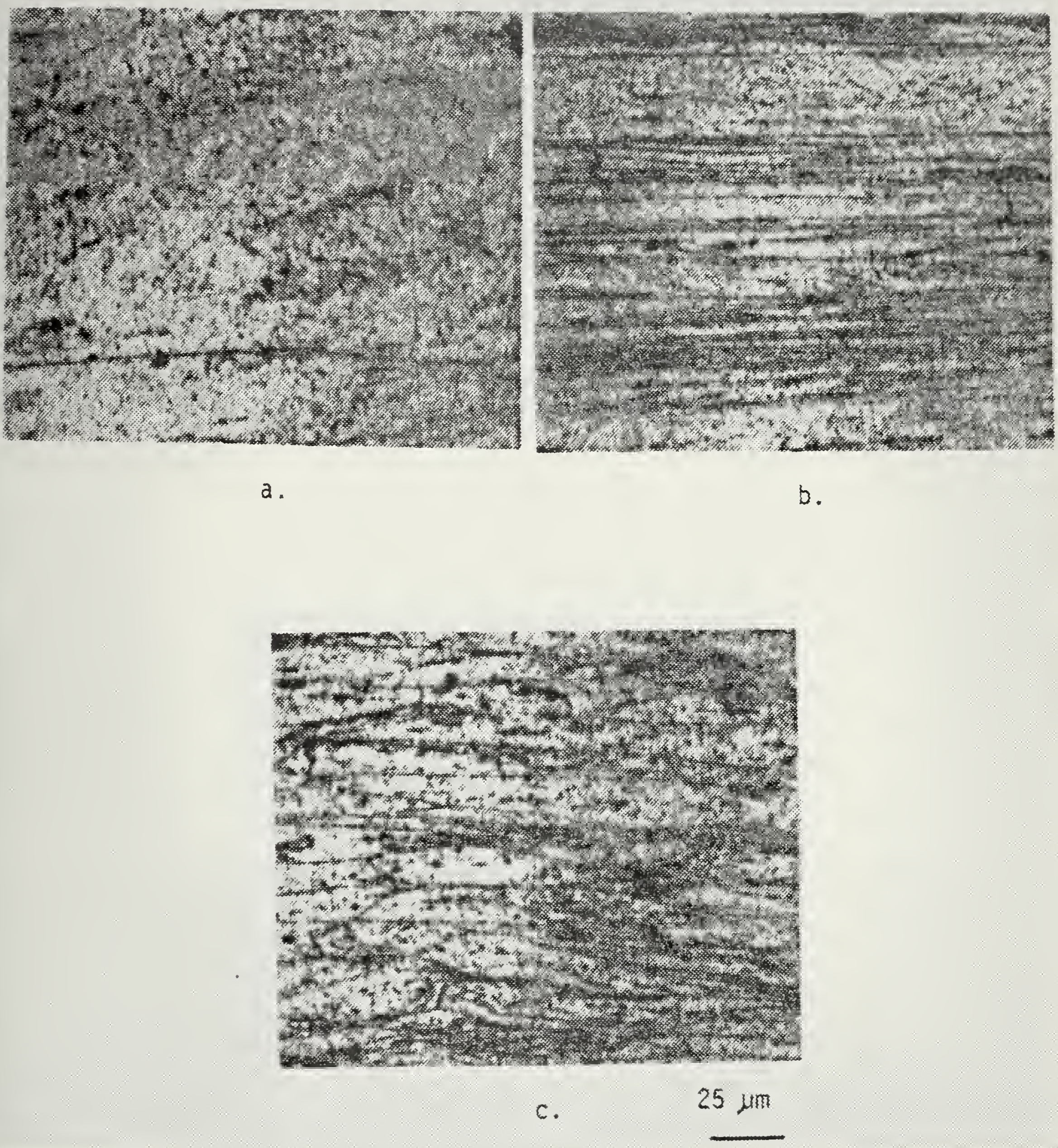

a.

b.

c.

FIGURE 14. Optical micrographs of the Al-8.14 wt pct Mg-0.40 wt pct Cu alloy, oil-quenched from homogenization: (a) longitudinal; (b) long transverse; (c) short transverse

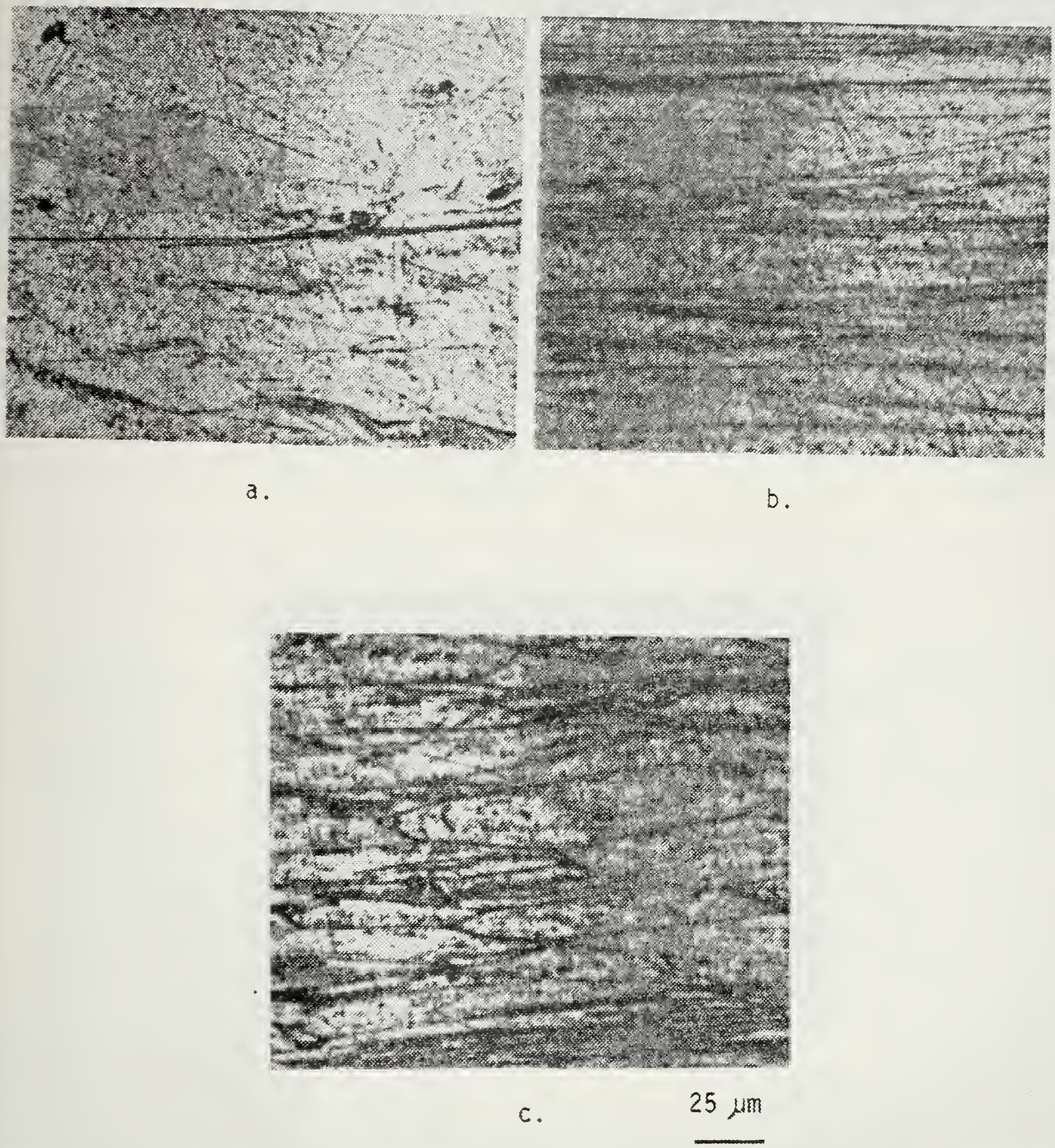

FIGURE 15. Optical micrographs of Al-8.14 wt pct Mg-0.40 wt pct Cu alloy, water-quenched from homogenization: (a) longitudinal, (b) long transverse, (c) short transverse

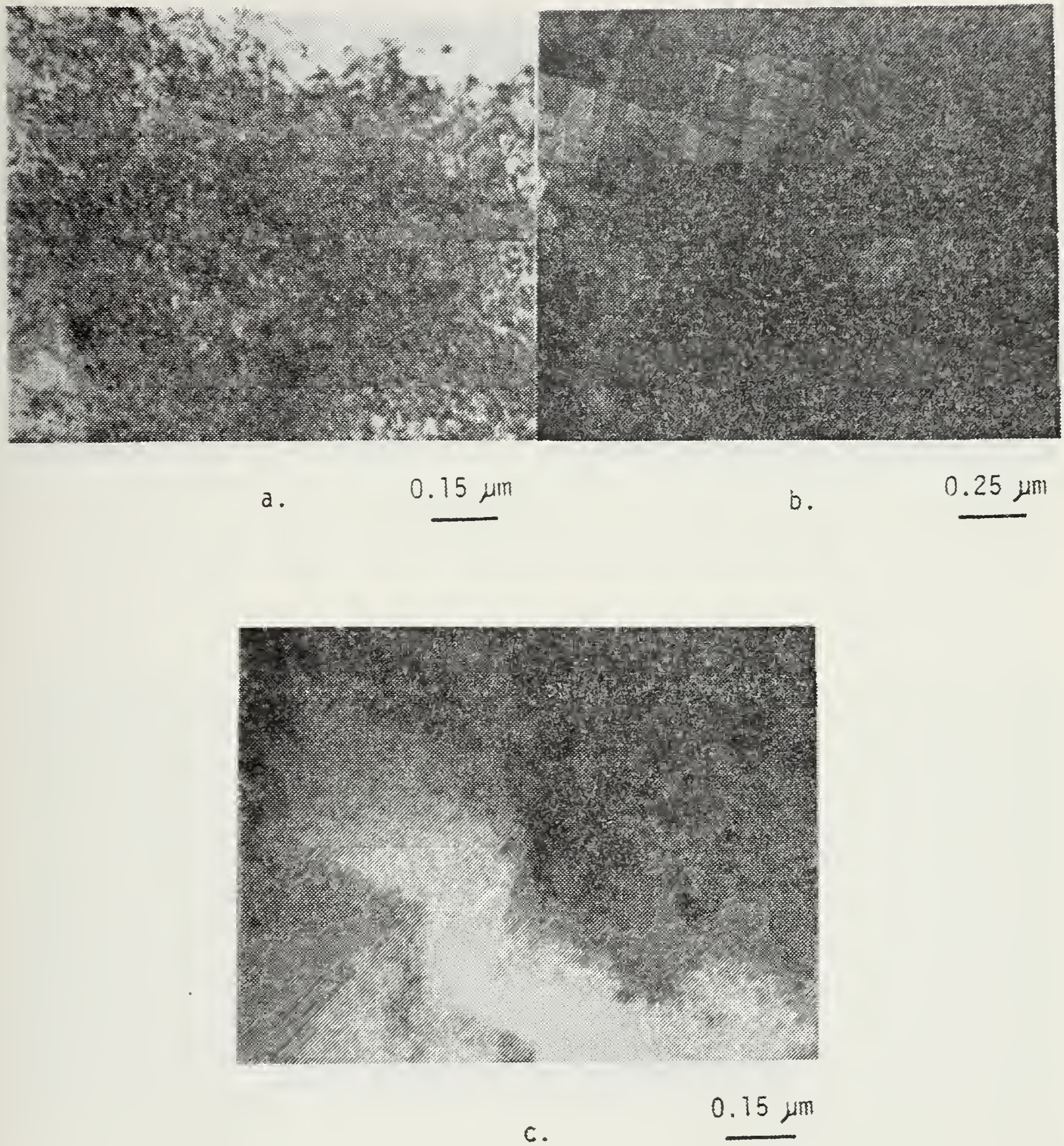

FIGURE 16. Regions of thin foils of Al-10.2 wt pct Mg, oil-quenched from homogenization, in the as-rolled condition indicating (a) heavily dislocated region similar to that expected of a cold worked material; (b) coarse precipitates which have sheared during subsequent rolling passes, and the diffuse cellular substructure; (c) light regions outlining original locations of precipitates and heavily dislocated structure

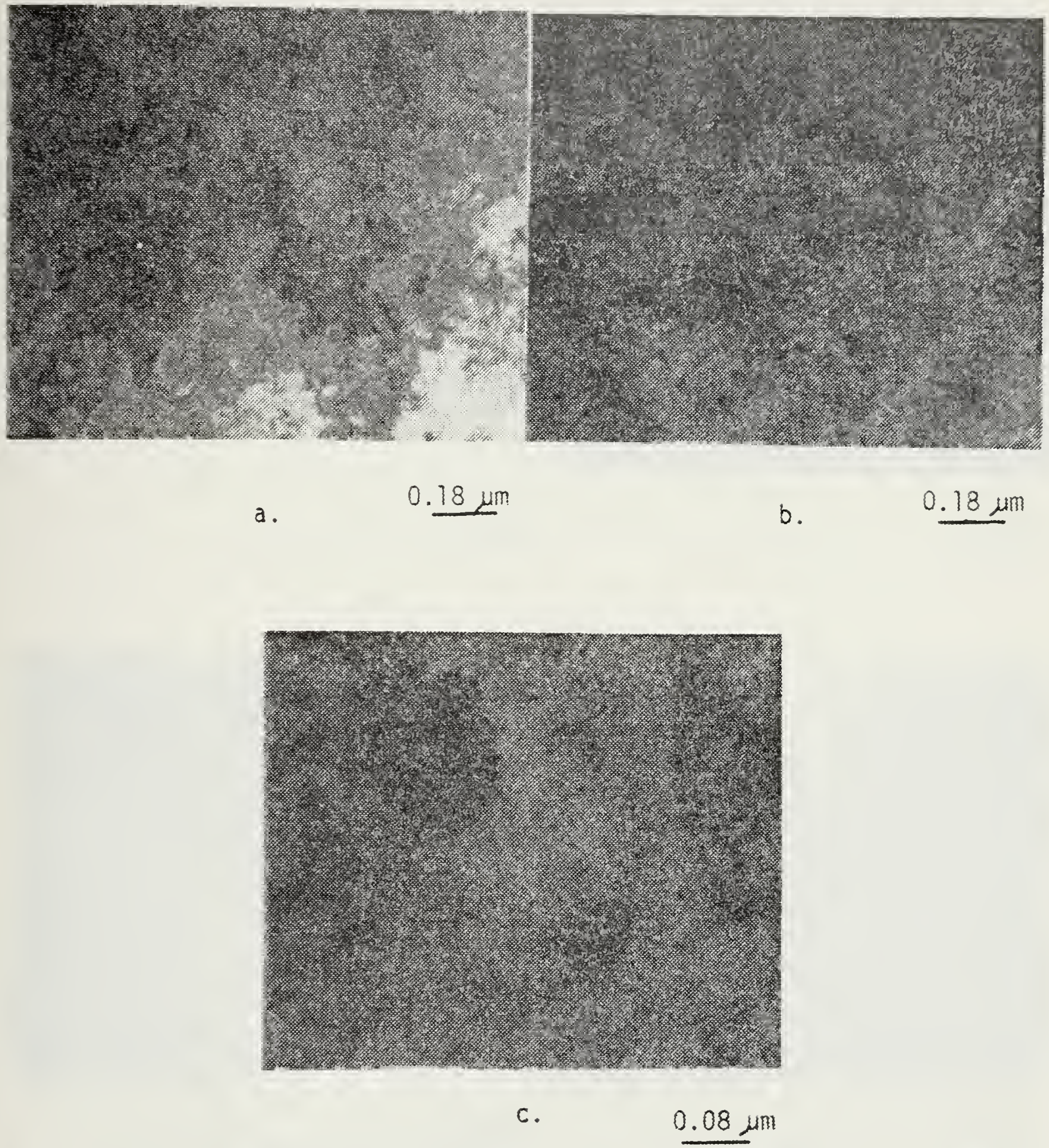

FIGURE 17. Regions of thin foils of Al-10.2 wt pct Mg, Water-quenched from homogenization, in the as-rolled condition indicating (a) heavily dislocated and diffuse cellular substructure; (b) same region as (a), but tilted; (c) cellular nature of substructure more clearly defined at higher magnification

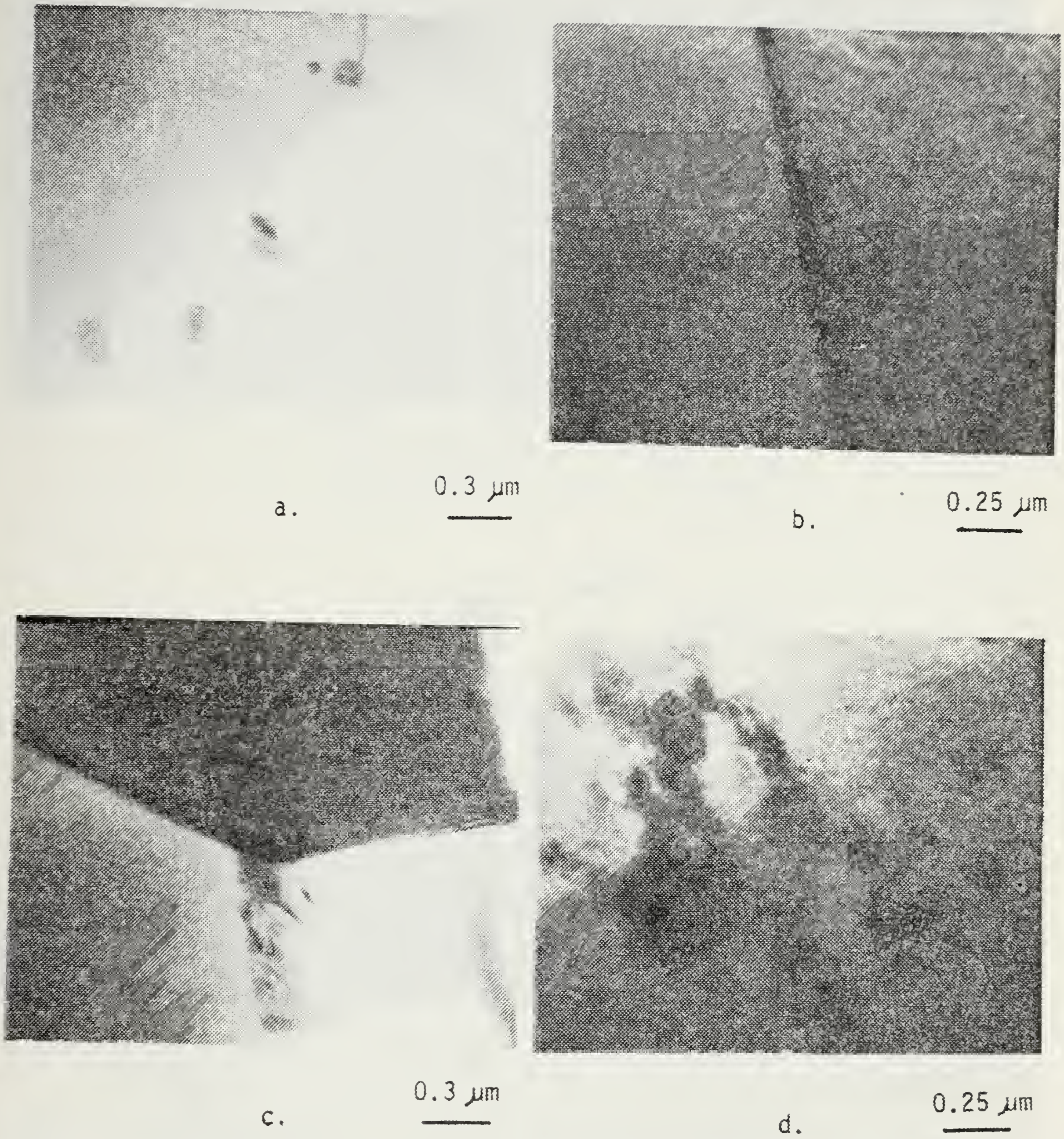

FIGURE 18. Thin foil micrographs of Al-10.2 wt pct Mg, solution treated and oil-quenched, indicating: (a) precipitates forming within GP zones, with dislocations pinned; (b) grain boundary, with GP zones well defined to the right through tilting; (c) grain boundary triple point with precipitates nucleation in the grain boundaries; (d) precipitates nucleated within GP zones

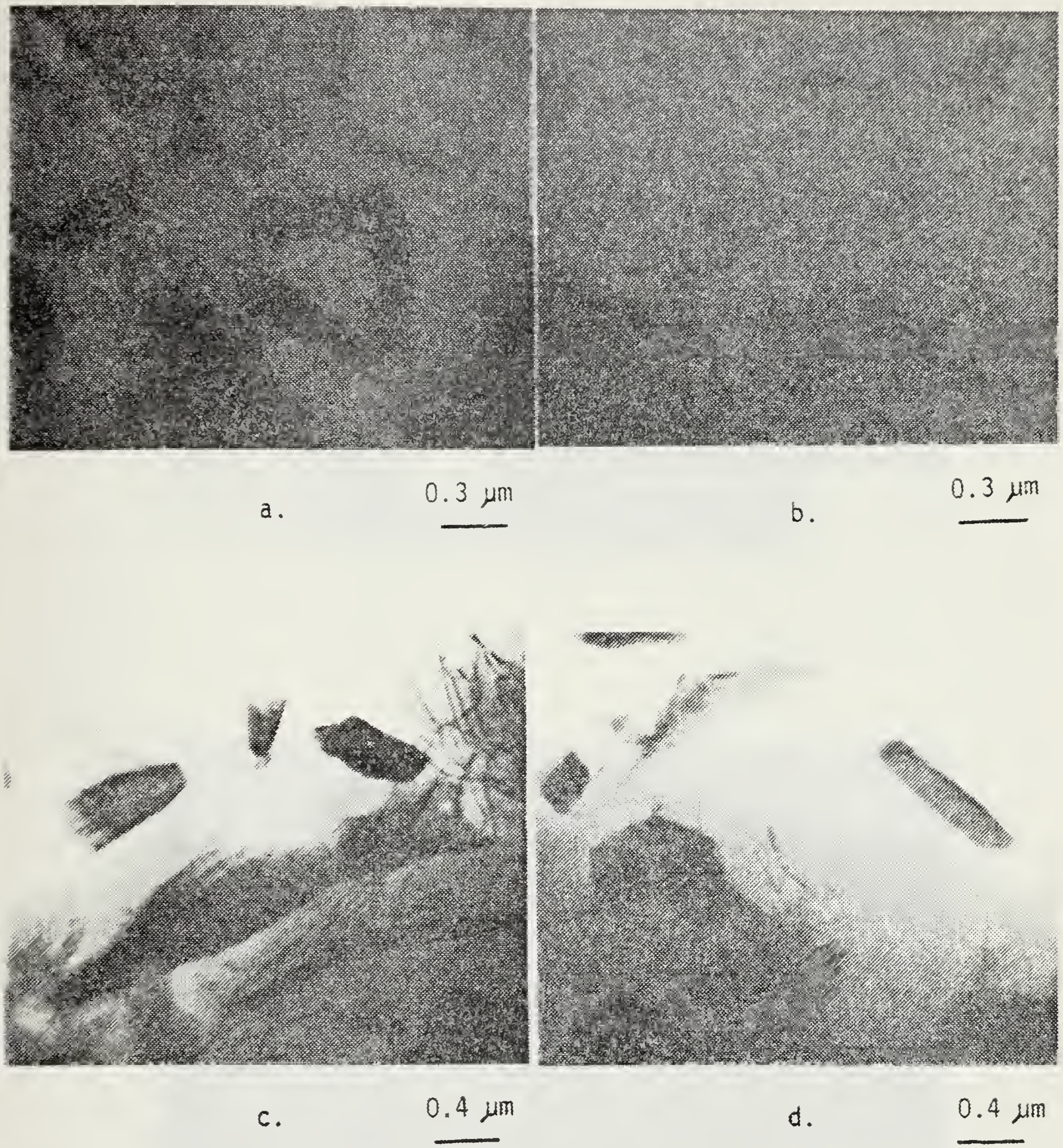

FIGURE 19. Thin foils of Al-10.2 wt pct Mg artificially aged (a) oil-quenched from homogenization showing sites originally occupied by second phase particles; (b) oil-quenched from homogenization, relatively free of precipitates with small dislocation density; (c) and (d) water-quenched from homogenization showing precipitate growth during aging at 300°C with dislocations believed generated through increments volume occupied by second phase particles

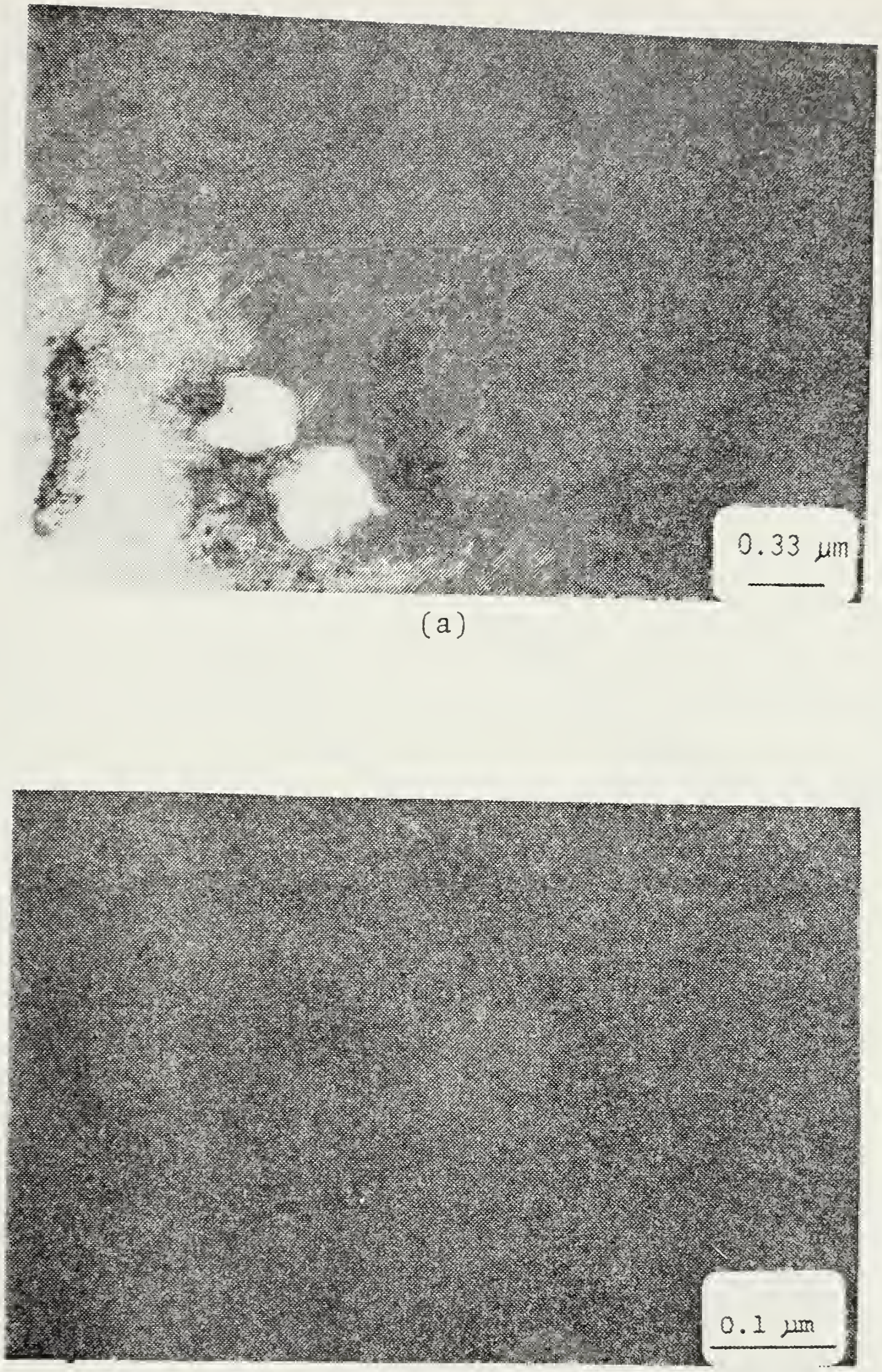

FIGURE 20. Al-10.2 wt pct Mg TEM micrographs contrasting cellular substructure of as-rolled materials when (a) oil-quenched from homogenization, and (b) water-quenched from homogenization. both materials were warm-rolled at 300°C

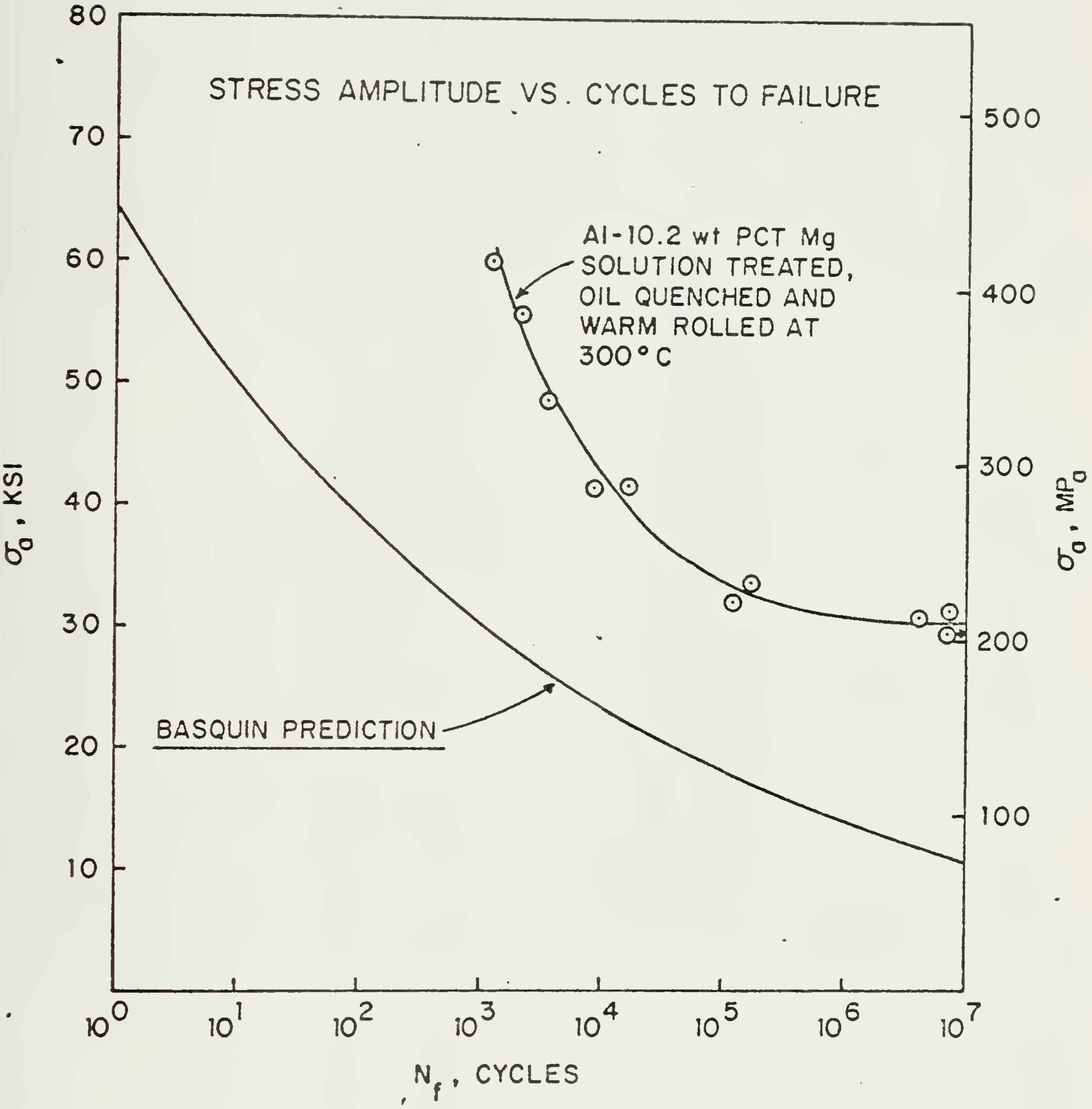

FIGURE 21. Stress Amplitude vs Cycles to Failure for Al-10.2 wt pct Mg Solution Treated, Oil-Quenched and Warm-Rolled at 300°C

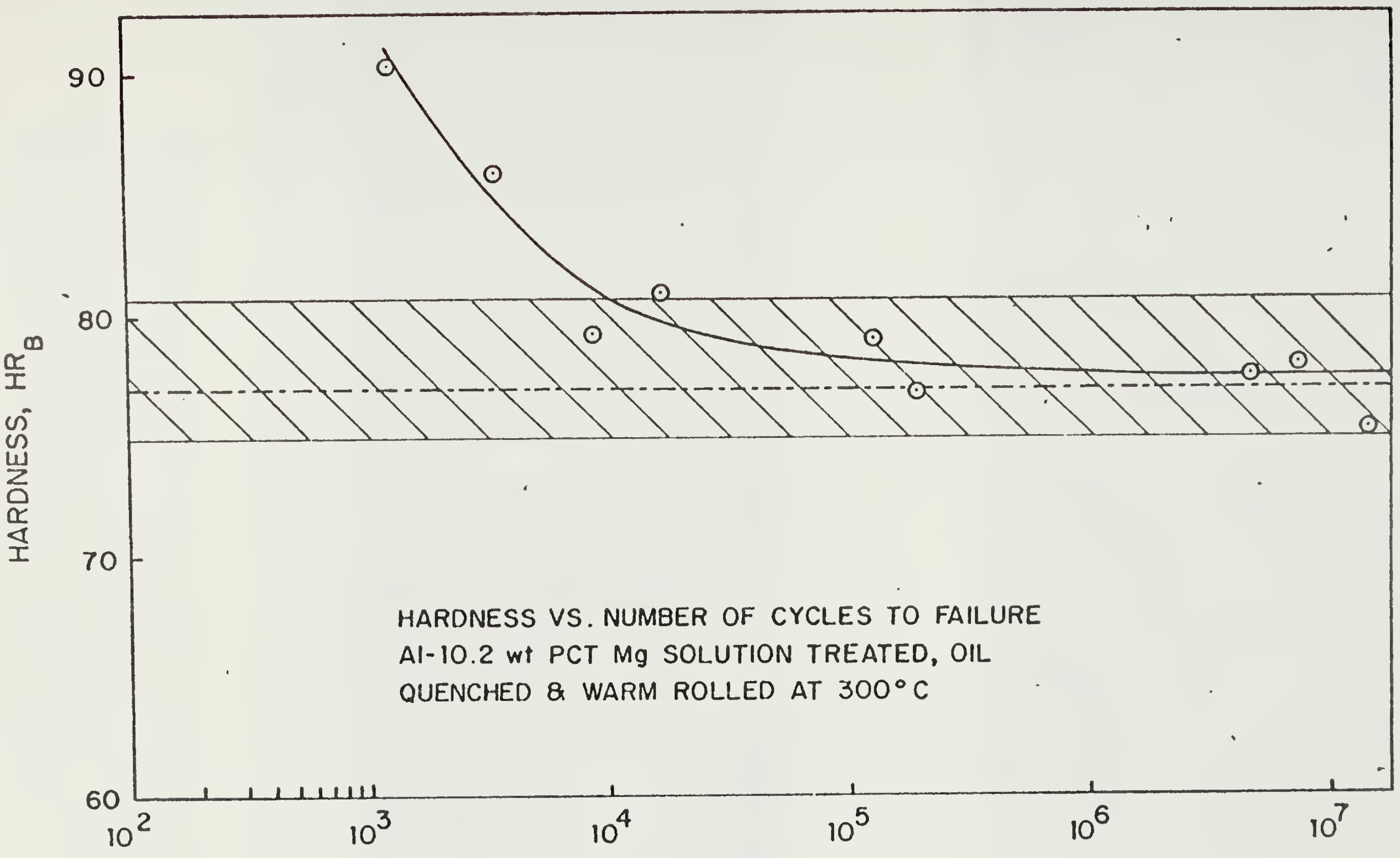

FIGURE 22. Hardness vs number of cycles to failure for Al-10.2 wt pct Mg solution treated, oil-quenched and warm-rolled at 300°C, illustrating cyclic hardening under low cycle fatigue conditions

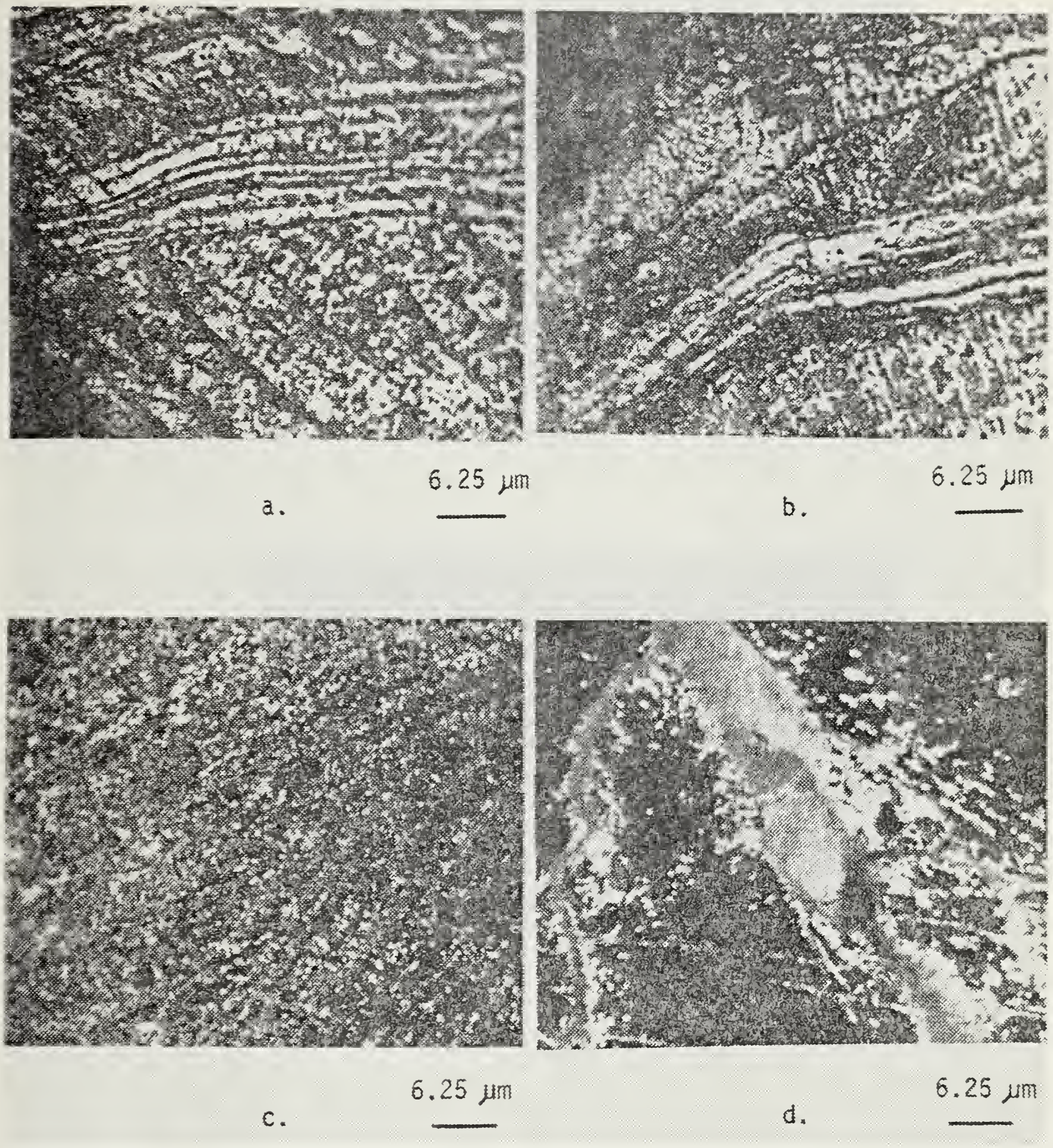

FIGURE 23. Optical micrographs of a low cycle fatigued specimen of Al-10.2 wt pct Mg solution treated, oil-quenched and warm-rolled at 300°C: (a) adjacent to the main fracture surface; (b) adjacent to the main fracture surface; (c) adjacent to the main fracture surface (dark field image); (d) adjacent to secondary crack (dark field image)

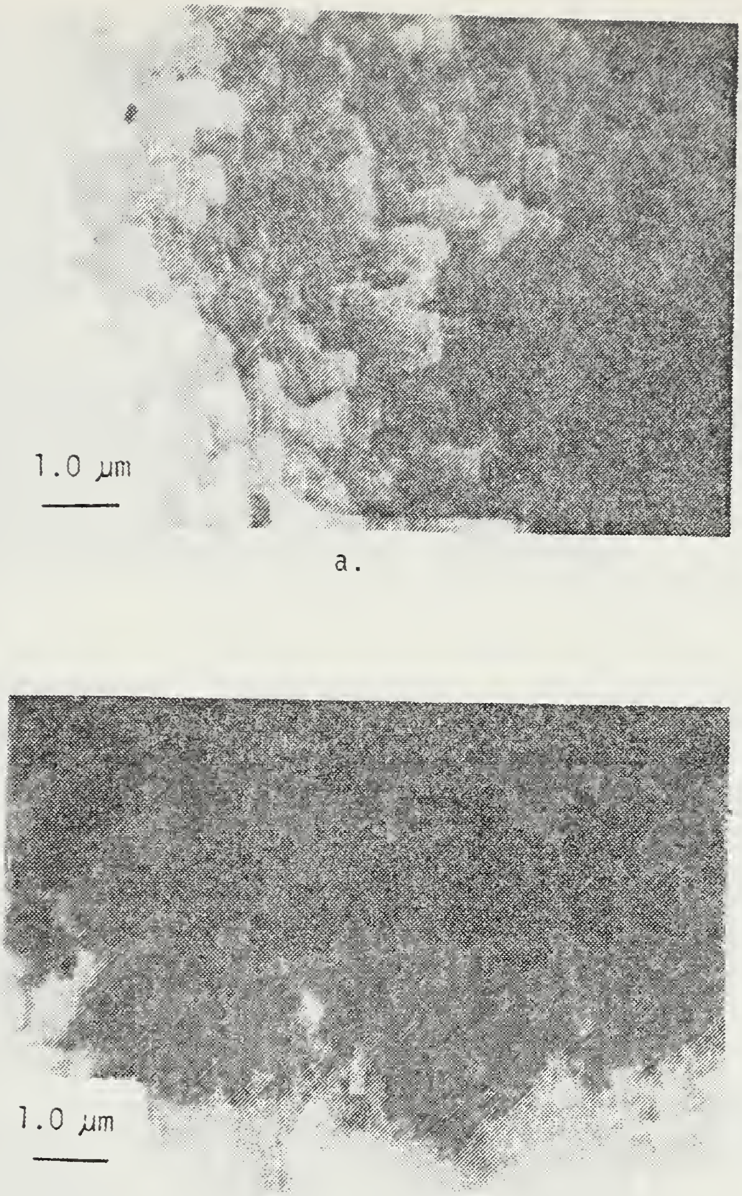

a.

b.

FIGURE 24. Thin Foil TEM micrographs of Al-10.2 wt pct Mg solution treated, oil-quenched and warm-rolled at 300°C, after being tested under low cycle fatigue conditions (a) foil taken from a region adjacent to the main fracture surface parallel to the rolling plane (b) foil taken from a region heavily concentrated with secondary cracks (parallel to the rolling plane)

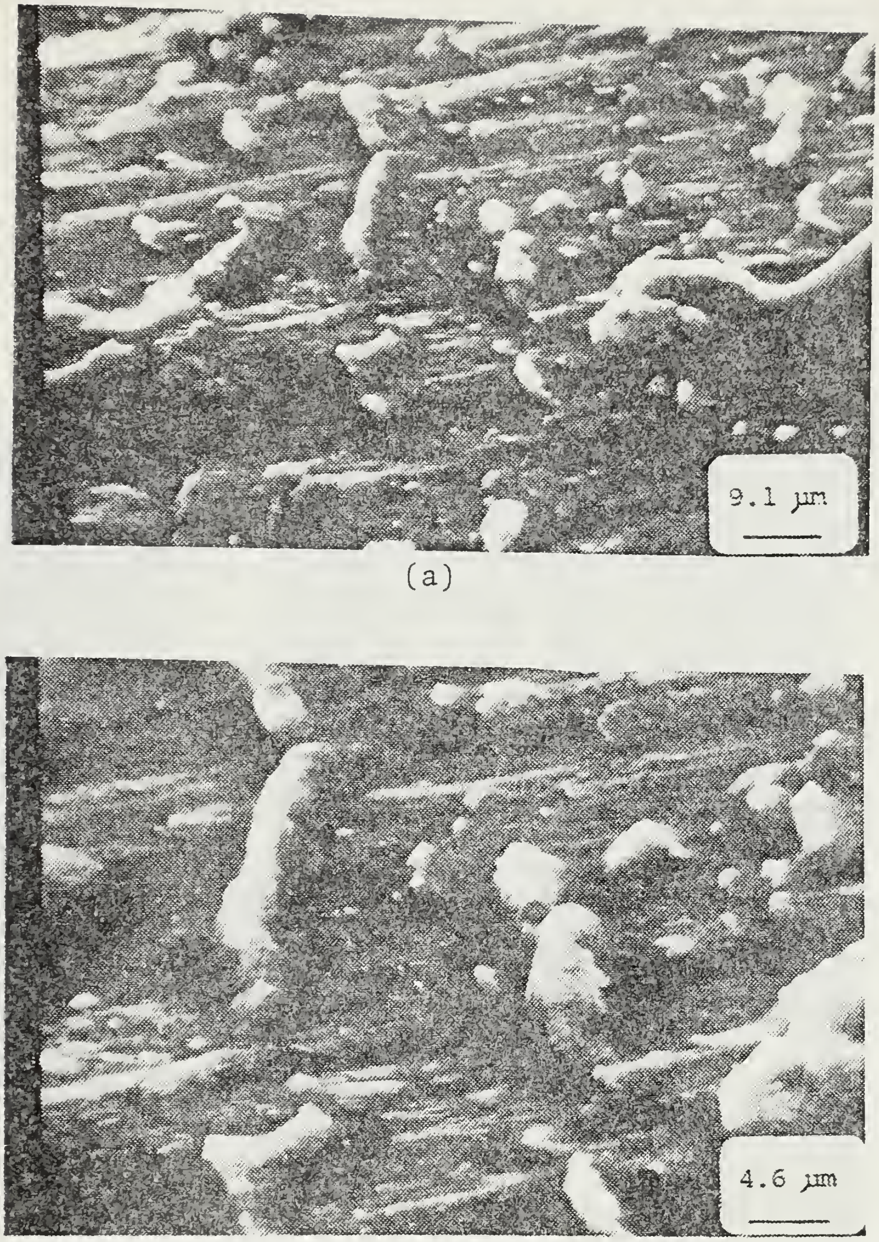

(a)

(b)

FIGURE 25. Scanning Electron Fractographs of stage II crack growth region of a specimen of Al-10.2 wt pct Mg, oil-quenched from homogenization. Failure occurred after 3300 cycles of fully reversed bending fatigue; (a) 1100x; (b) 2200x

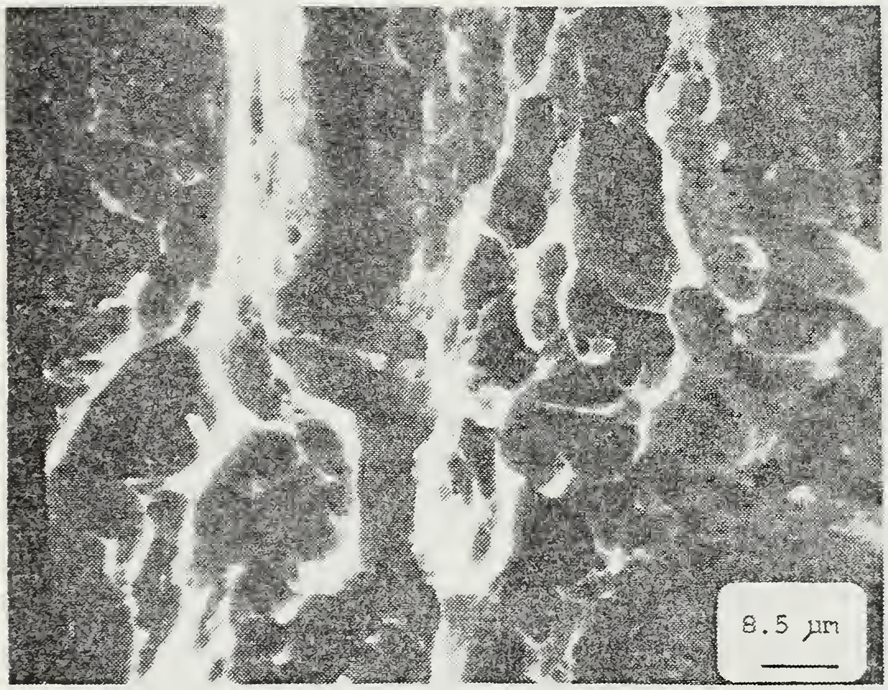

FIGURE 26. Overload region of same specimen as Figure 27 at 1175x on the Scanning Electron Microscope

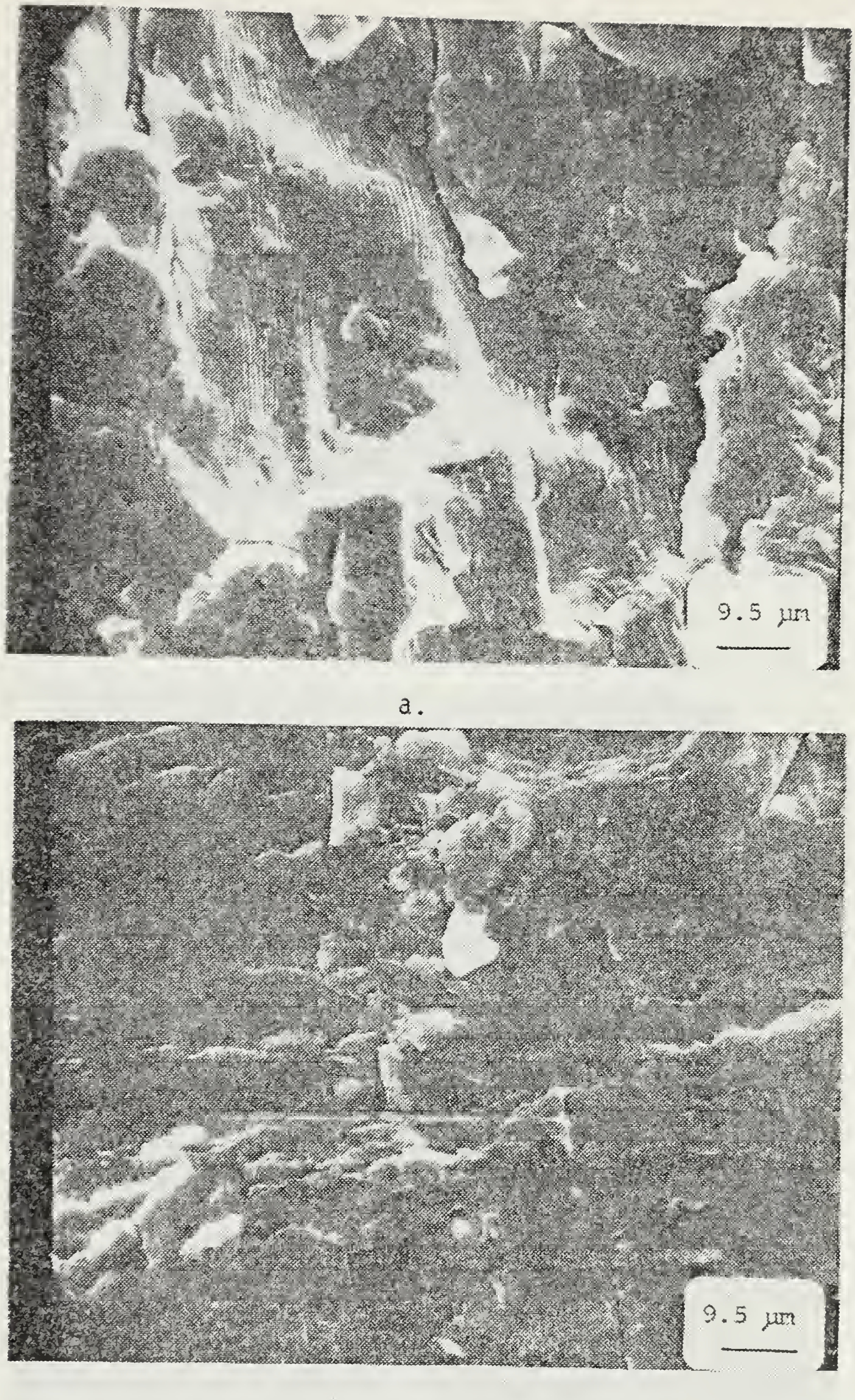

a.

b.

FIGURE 27. (a) Regions of Stage II crack growth in a specimen of Al-10.2 wt pct Mg oil-quenched from homogenization temperature which fractured after 1.81 x 10^5 cycles: (b) overload region of the same specimen (SEM x 1050)

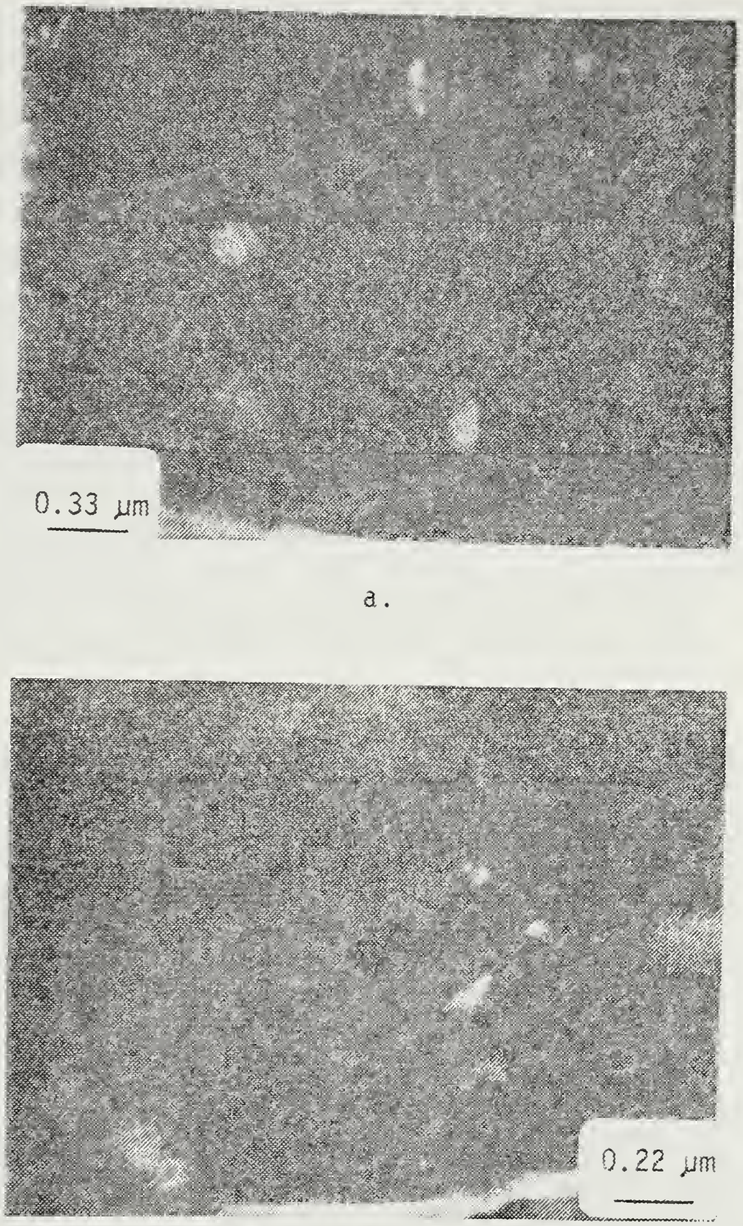

a.

b.

FIGURE 28. Transmission Electron Micrographs of thin foils taken from a plane parallel to the rolling plane of Al-10.2 wt pct Mg alloy, oil-quenched from homogenization and warm-rolled at 300°C. failure occurred after 4.4 x 10^6 cycles

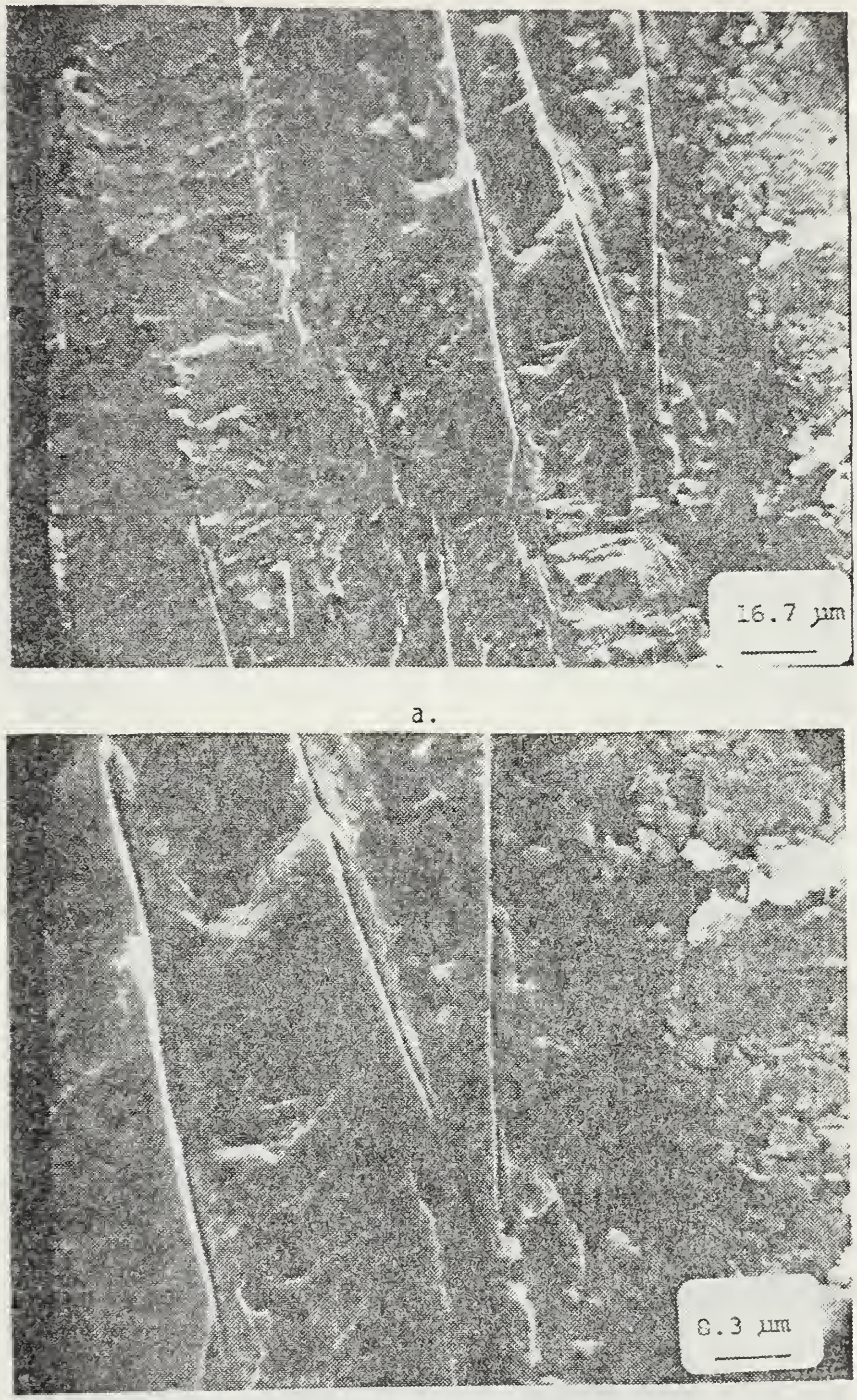

a.

b.

FIGURE 29. Transition from stage I growth to stage II growth in Al-10.2 wt pct Mg, oil-quenched from homogenization and warm-rolled at 300°C. failure occurred after 4.4×10^6 cycles of fully resersed bending fatigue. (a) SEM fractograph x600 (b) SEM fractograph x1200

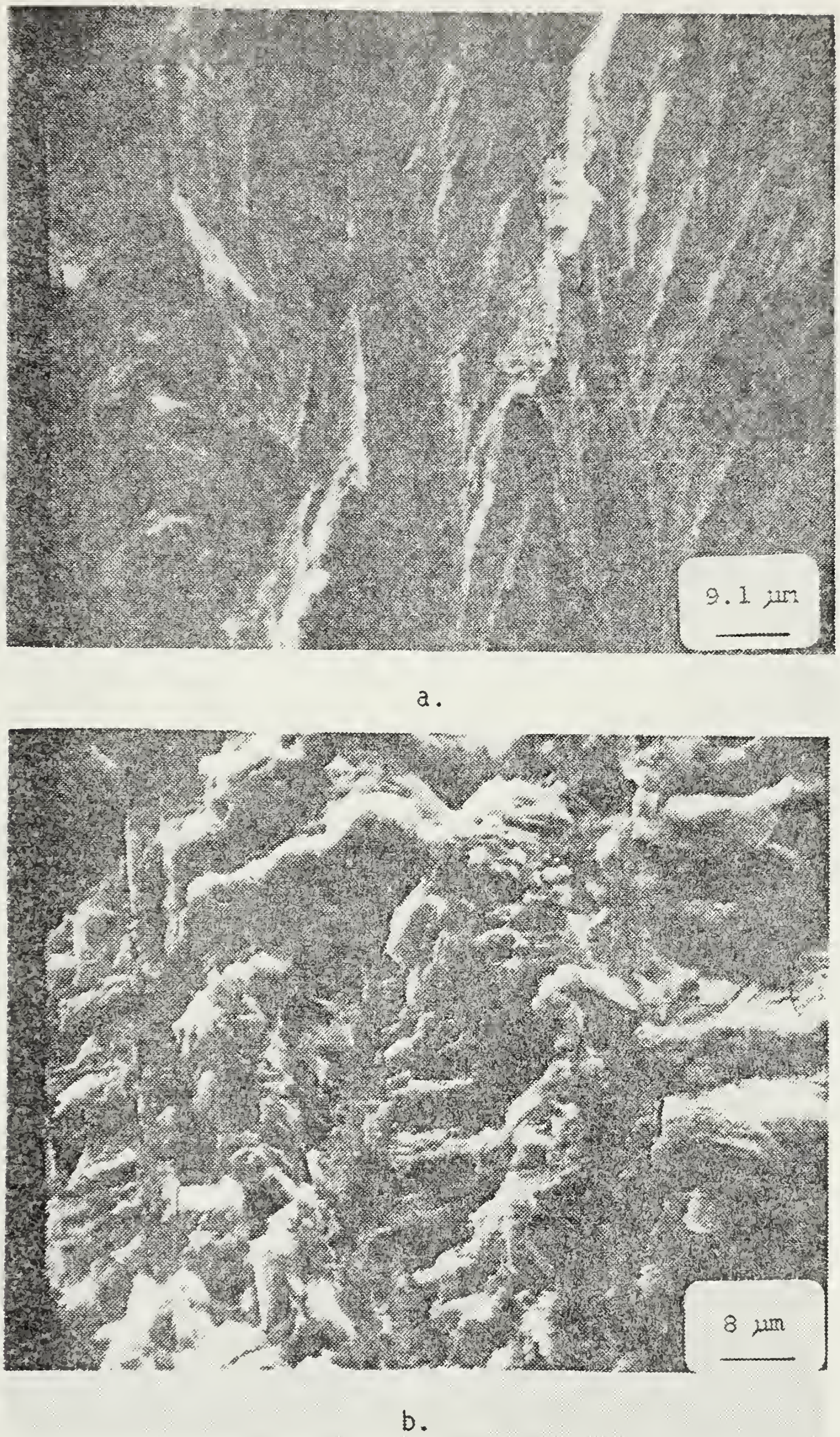

FIGURE 30. (a) Fully developed Stage II crack growth of same specimen shown in Figure 29; magnification 1100x SEM; (b) Stage III fracture appearance; magnification 1250x SEM

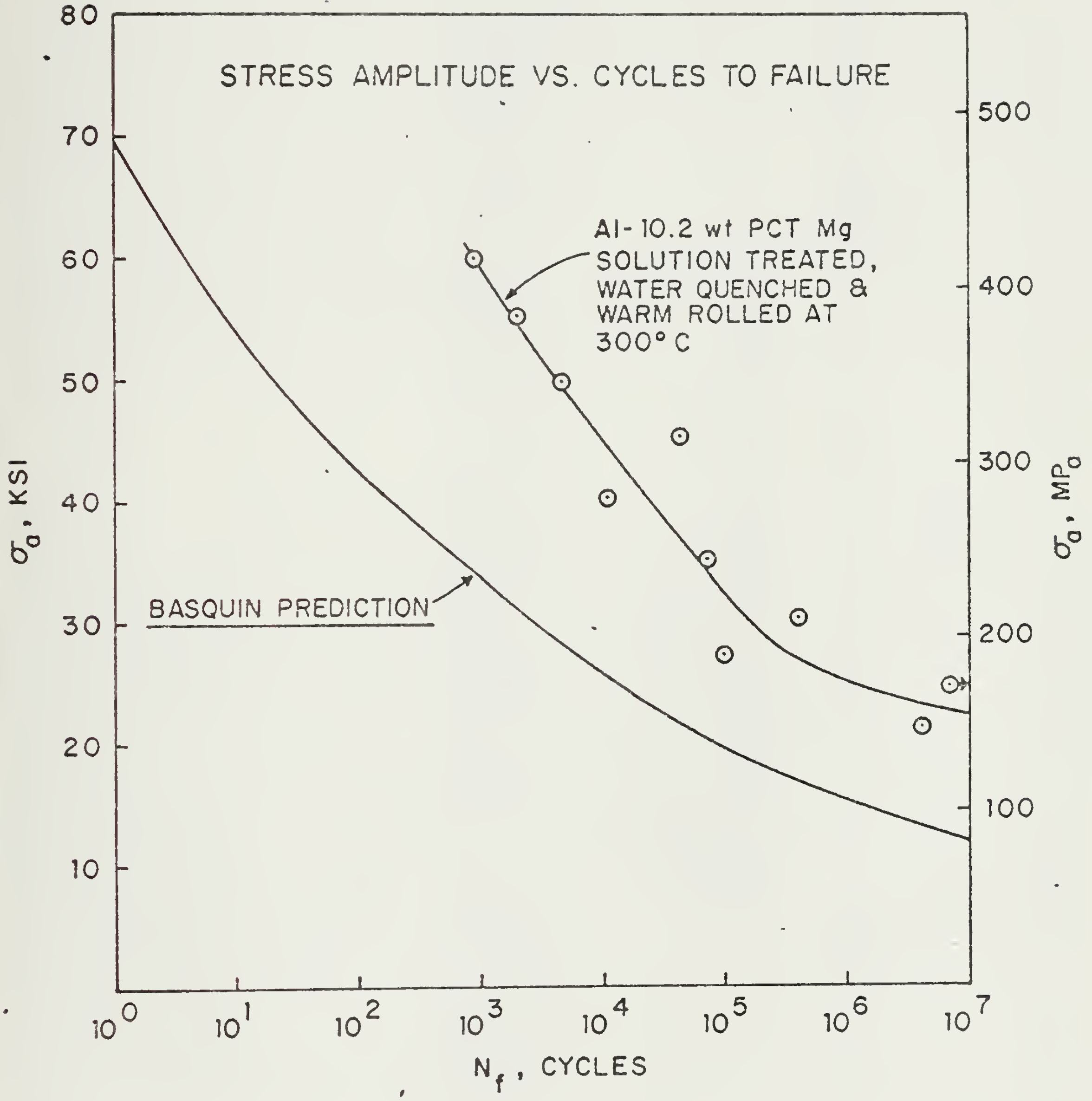

FIGURE 31. Stress amplitude vs cycles to failure for Al-10.2 wt pct Mg solution treated, water-quenched and warm-rolled at 300°C

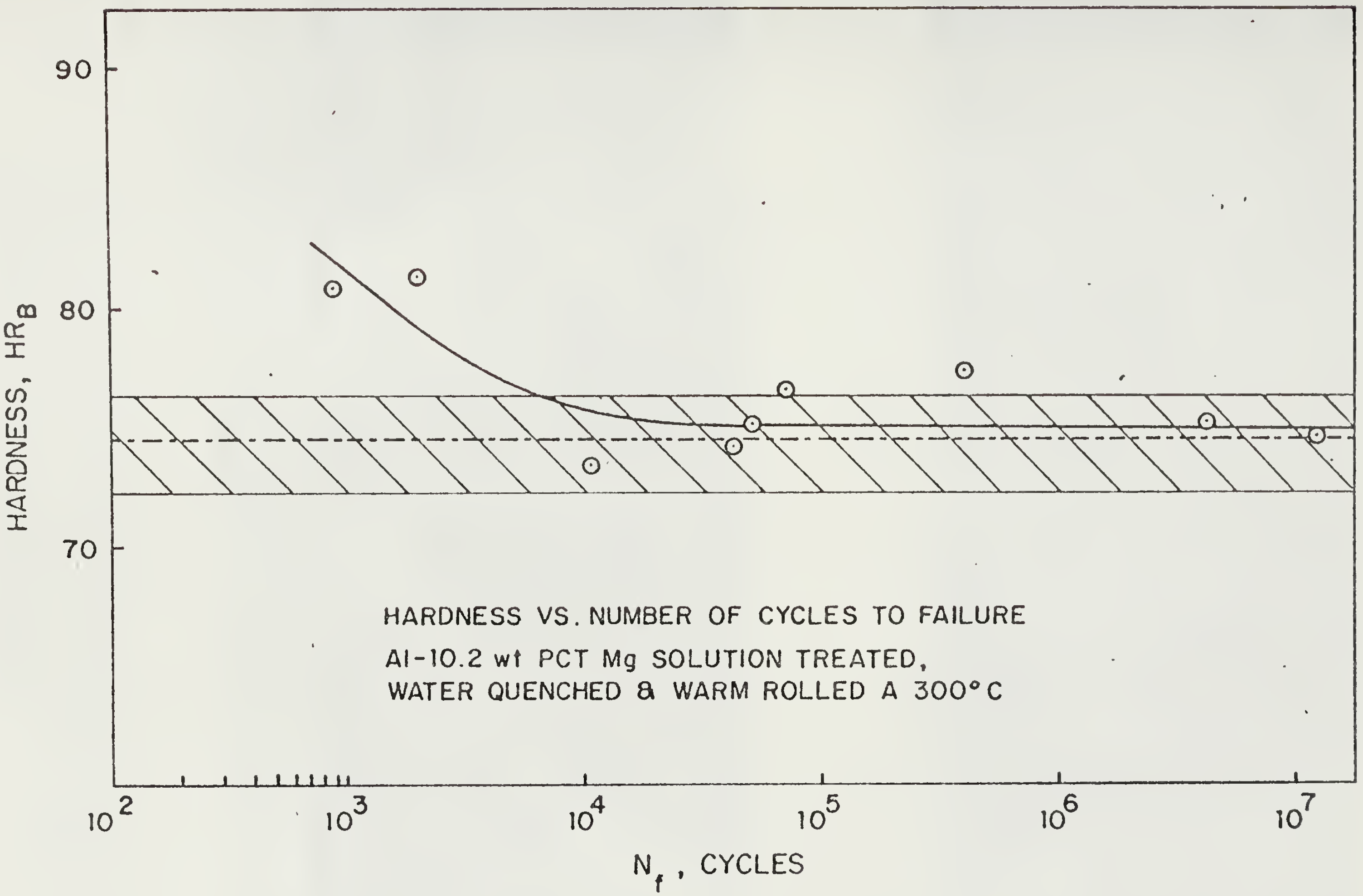

FIGURE 32. Hardness vs number of cycles to failure for Al-10.2 wt pct Mg solution treated, water-quenched and warm-rolled at 300°C. Illustration cyclic hardening under low cycle fatigue conditons

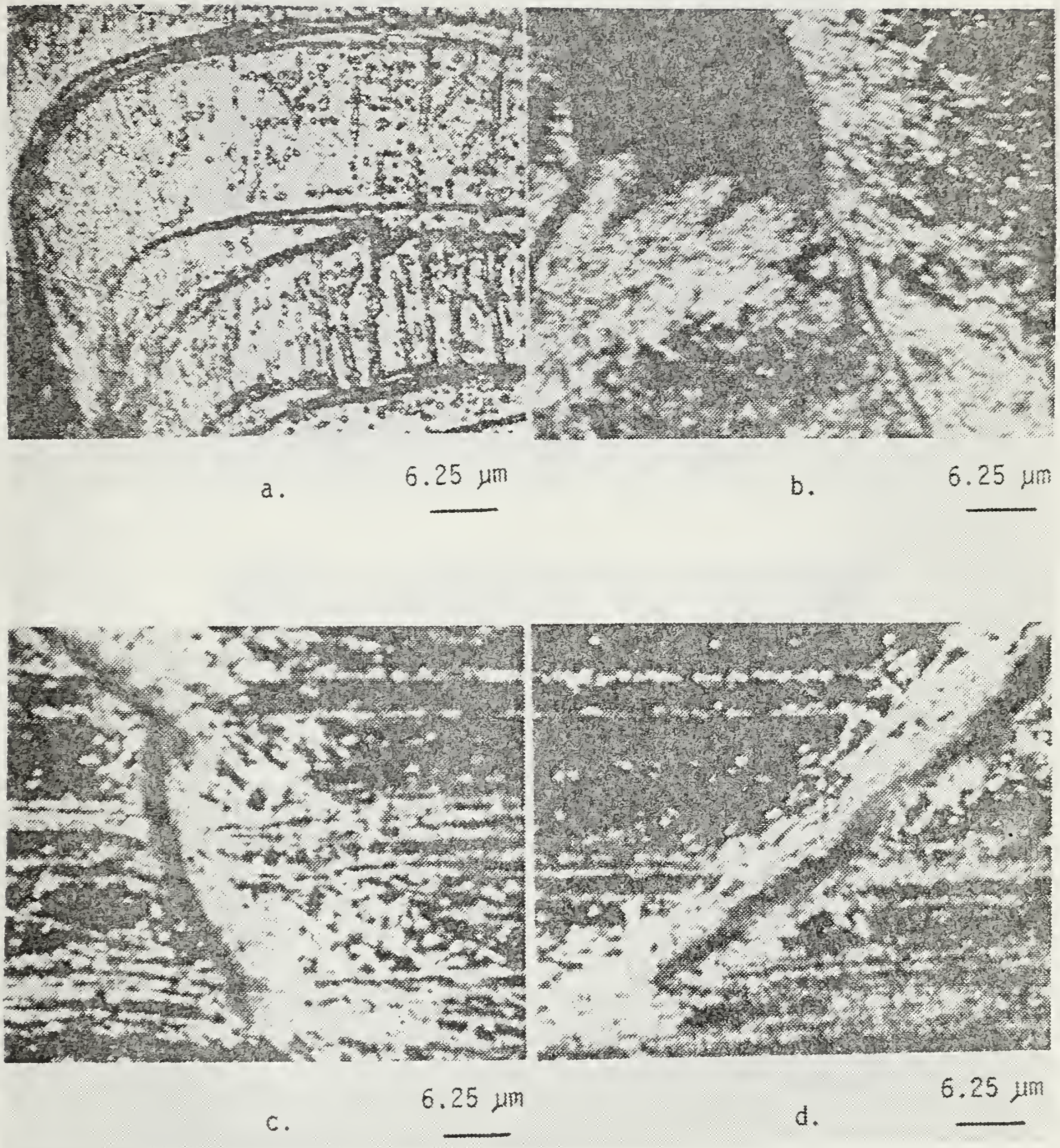

FIGURE 33. Optical micrographs of low cycle fatigued specimen of Al-10.2 wt pct Mg solution treated, water-quenched and warm-rolled at 300°C: (a) adjacent to the main fracture surface, (b), (c) and (d) adjacent to secondary cracks (dark images)

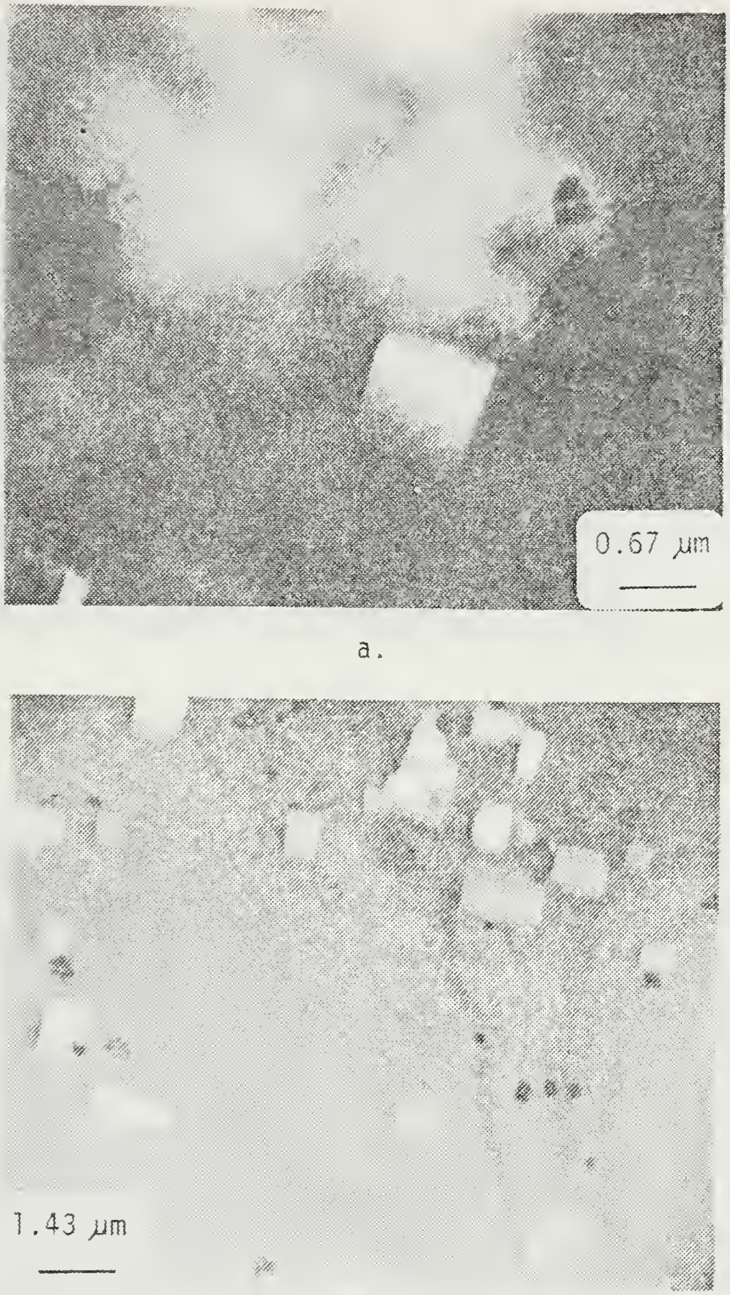

a.

b.

FIGURE 34. Thin foil TEM micrograph of Al-10.2 wt pct Mg solution treated, water-quenched and warm-rolled at 300°C after being tested under low cycle fatigue conditions; (a) some indication of larger precipitates (b) region where volume fraction of precipitates is increased over the as-rolled condition (dark blotches in (b) are artifact from electrolyte thinning)

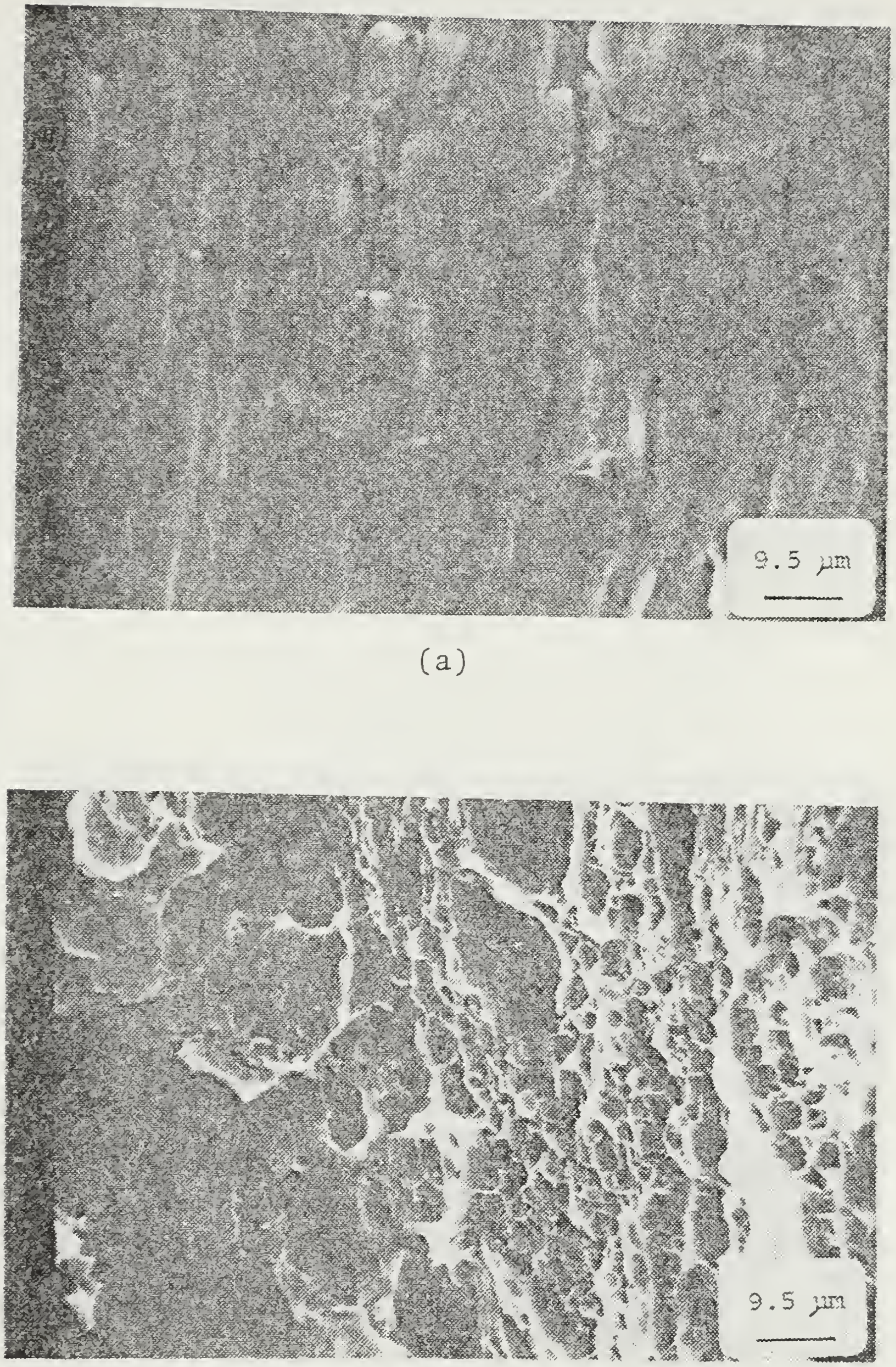

(a)

(b)

FIGURE 35. SEM fractographs of Al-10.2 wt pct Mg, solution treated, water-quenched and warm-rolled at 300°C, in which fracture occurred after 3400 cycles: (a) Stage II crack growth x1050; (b) overload region x1050

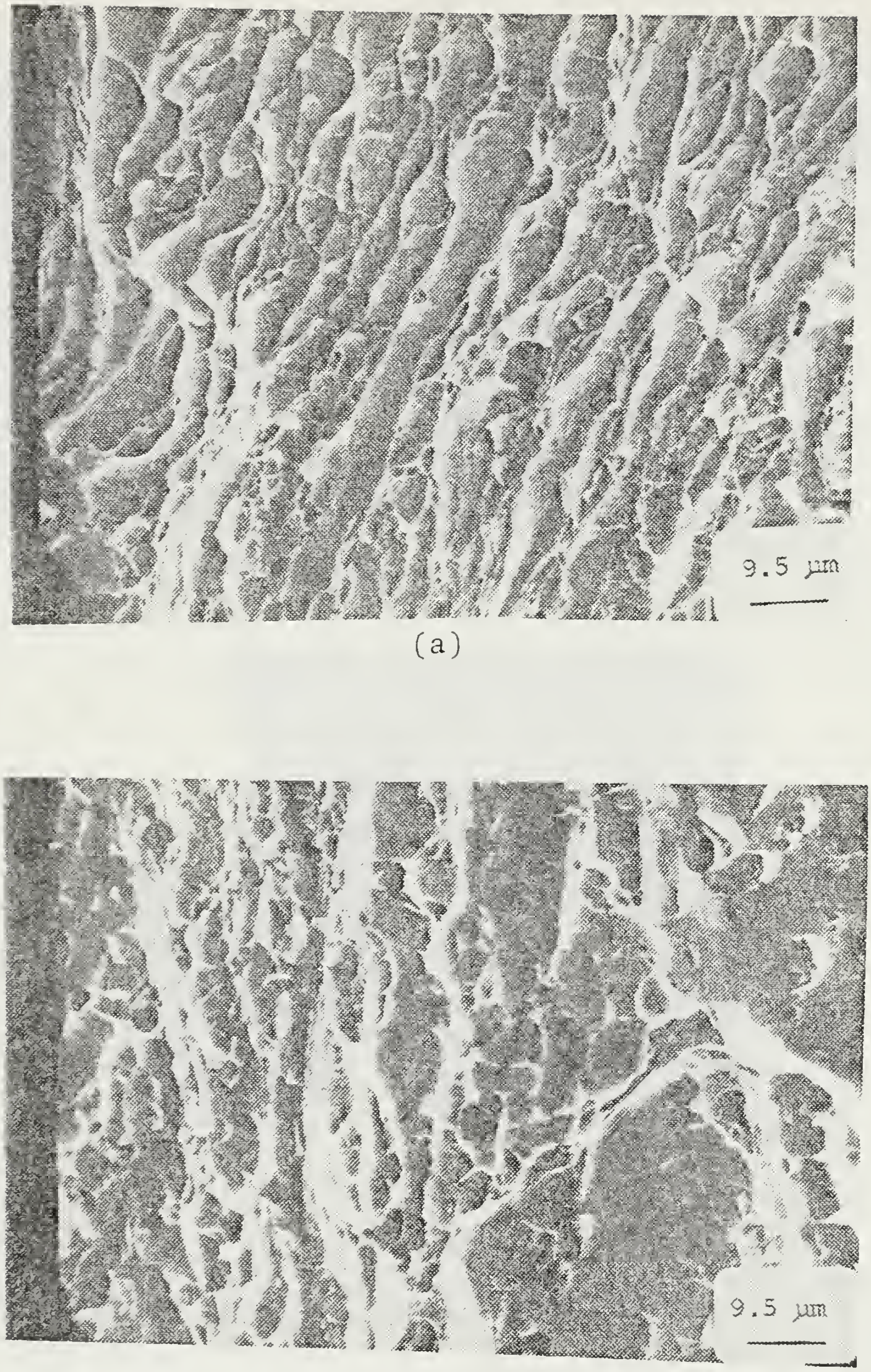

(a)

(b)

FIGURE 36. SEM fractographs of Al-10.2 wt pct Mg, water-quenched and warm-rolled at 300°C, in which fracture occurred after 10600 cycles: (a) Stage II striations x1050 and (b) Stage III (overload region) x1050

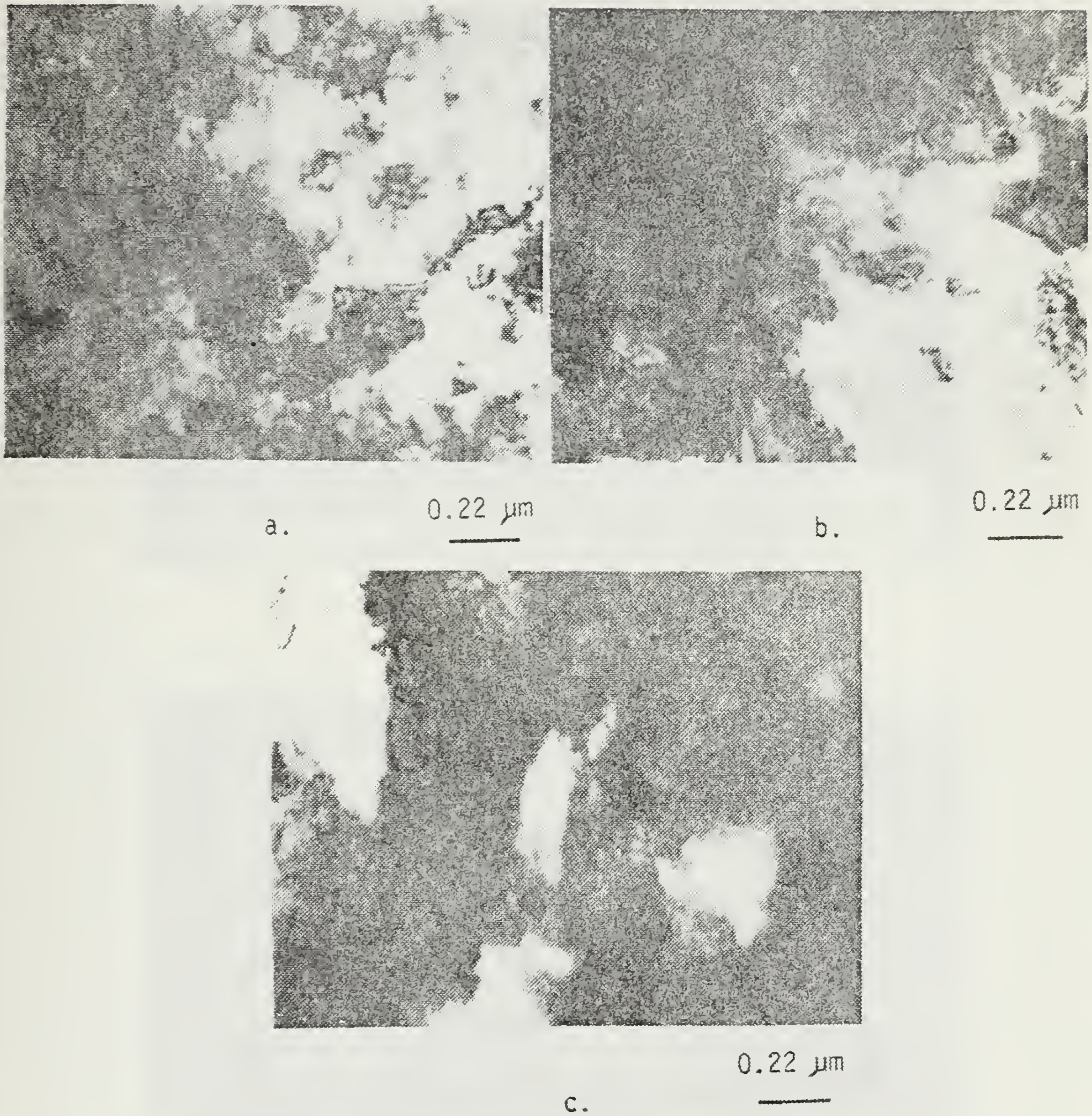

FIGURE 37. Thin foil TEM micrographs of Al-10.2 wt pct Mg, water-quenched and warm-rolled at 300°C, in which failure occurred after 4.2×10^6 cycles: (a) regions of high dislocation density and relatively dislocation free zones; (b) same region as (a) except tilted; (c) region similar to those shown in (a) and (b), but from a different section of the fatigue specimen

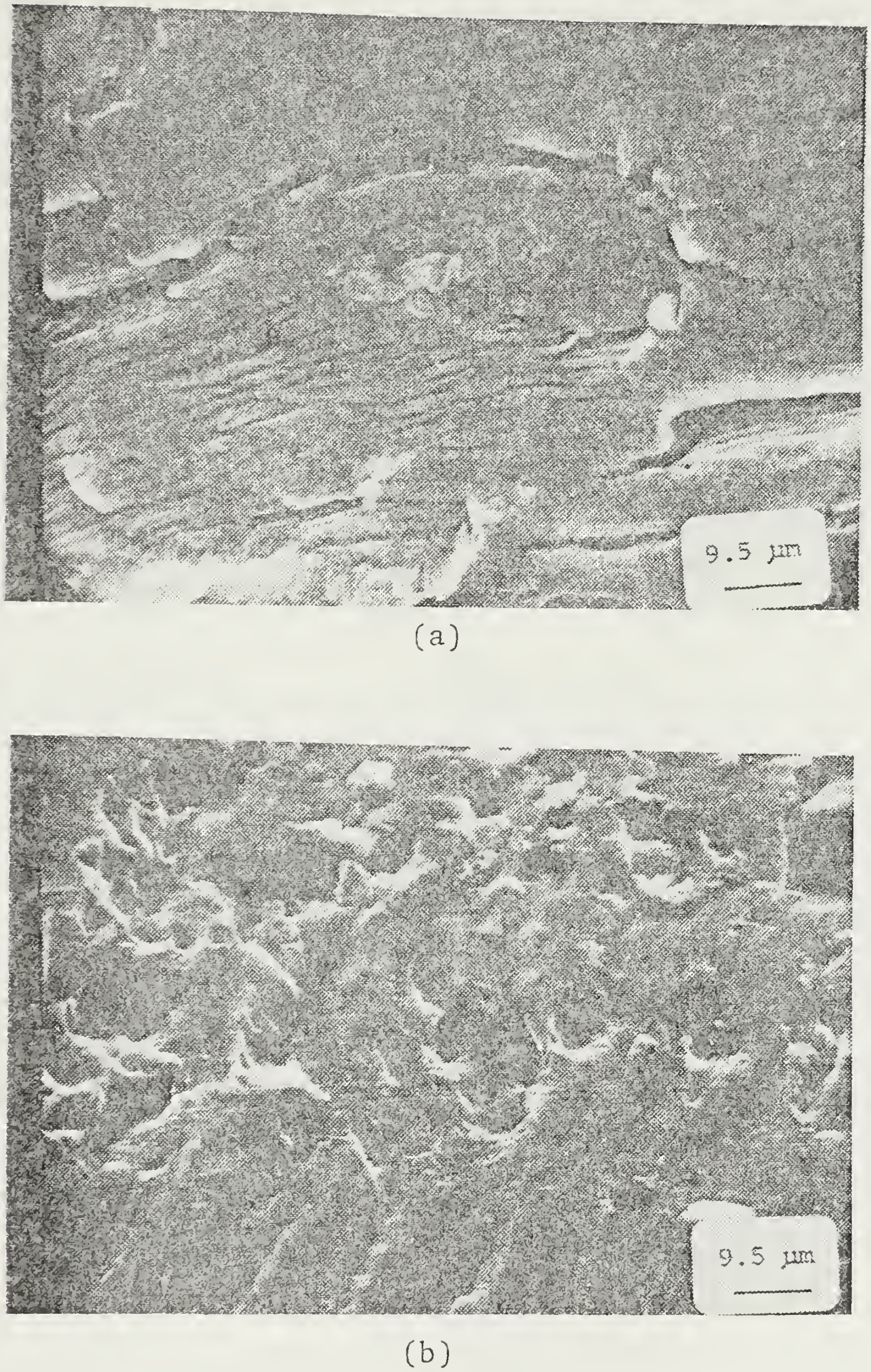

FIGURE 38. SEM fractographs of Al-10.2 wt pct Mg, solution treated, water-quenched and warm-rolled at 300°C, in which failure occurred after 4.2 x 10^6 cycles: (a) Stage II crack growth x 1050; (b) Stage III crack growth x1050

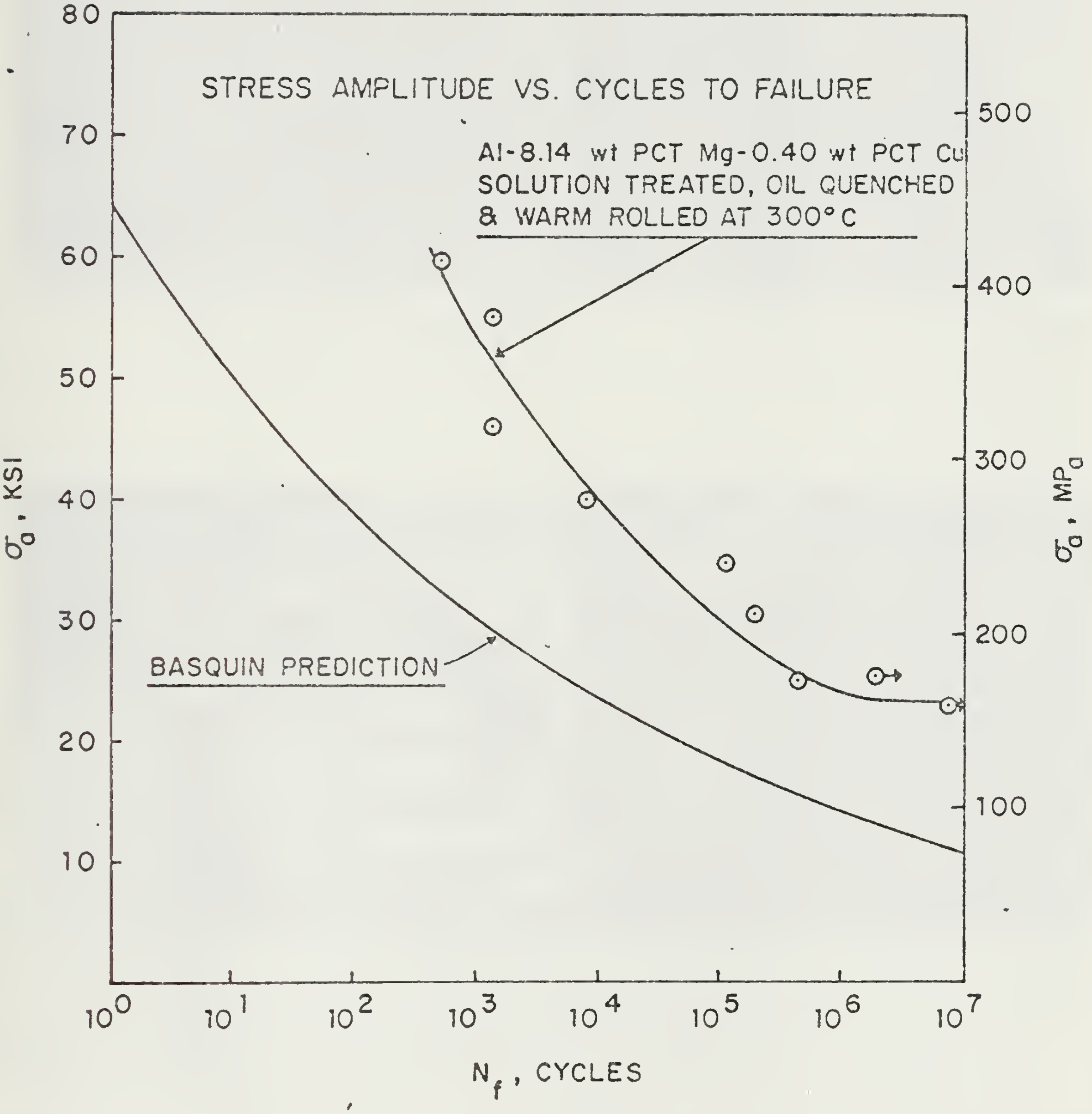

FIGURE 39. Stress amplitude vs cycles to failure for Al-8.14 wt pct Mg-0.40 wt pct Cu solution treated, oil-quenched and warm-rolled at 300°C

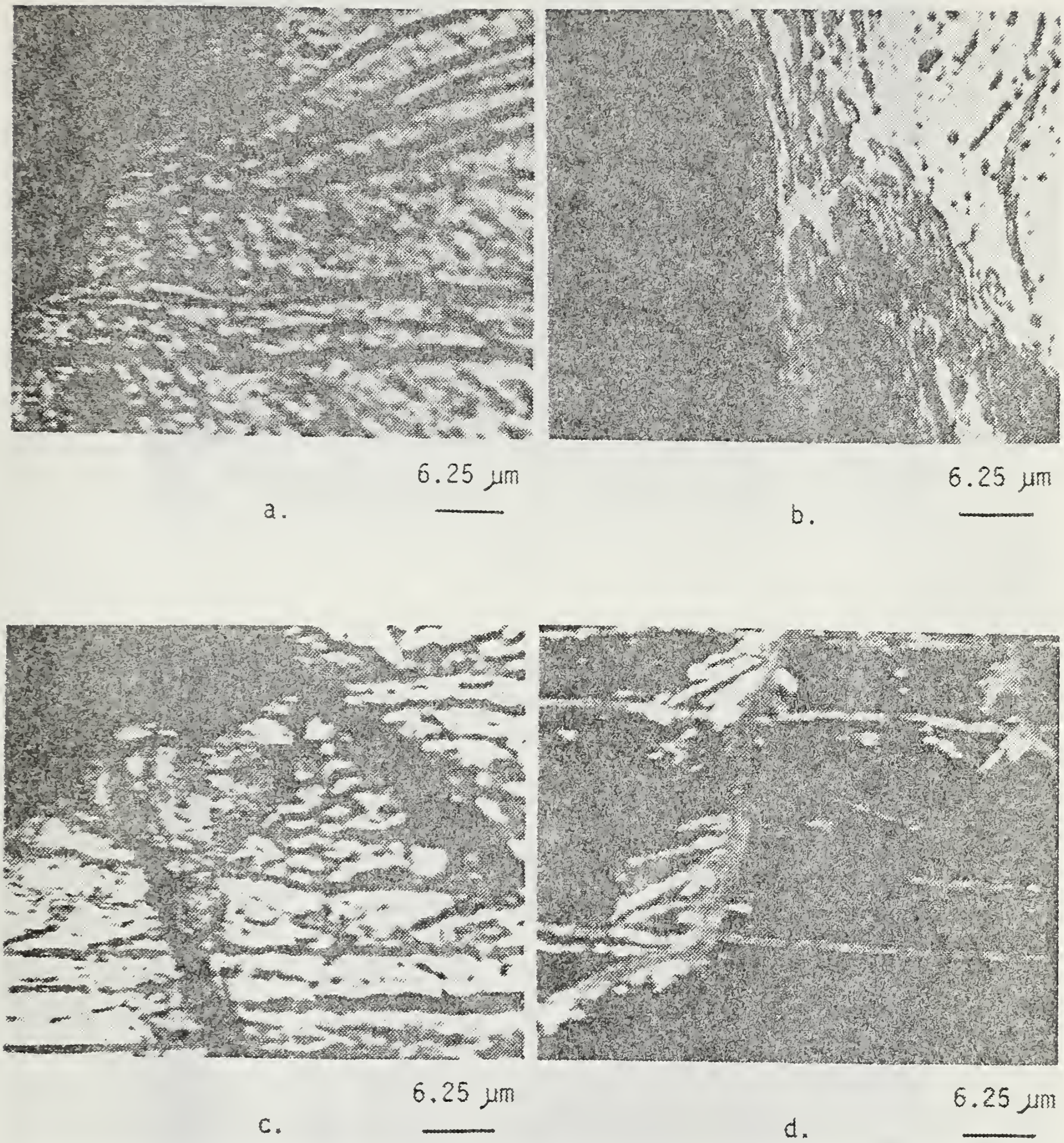

a. b. c. d.

FIGURE 40. Optical micrographs of a low cycle fatigued specimen of Al-8.14 wt pct Mg-0.40 wt pct Cu, solution treated, oil-quenched and warm-rolled at 300°C: (a) adjacent to the main fracture surface; (b) adjacent to the main fracture surface; (c) secondary cracks originating at the main fracture surface; and (d) secondary cracks (dark image)

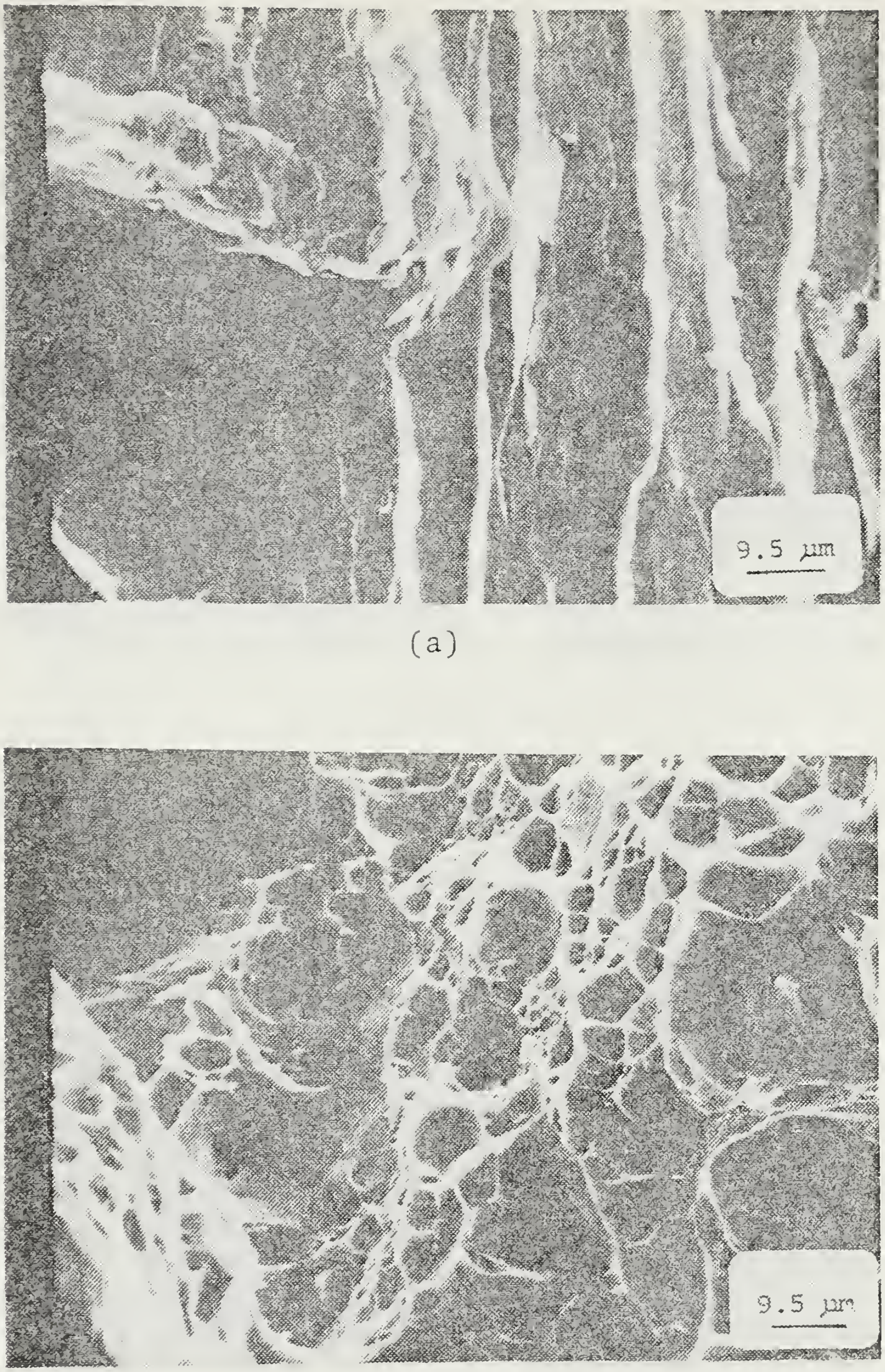

(a)

(b)

FIGURE 41. SEM fractographs of a specimen of Al-8.14 wt pct Mg-0.40 wt pct Cu, solution treated, oil-quenched and warm-rolled at 300°C, in which failure occurred after 1400 cycles: (a) Stage II crack growth x1050; (b) Stage III crack growth x1050

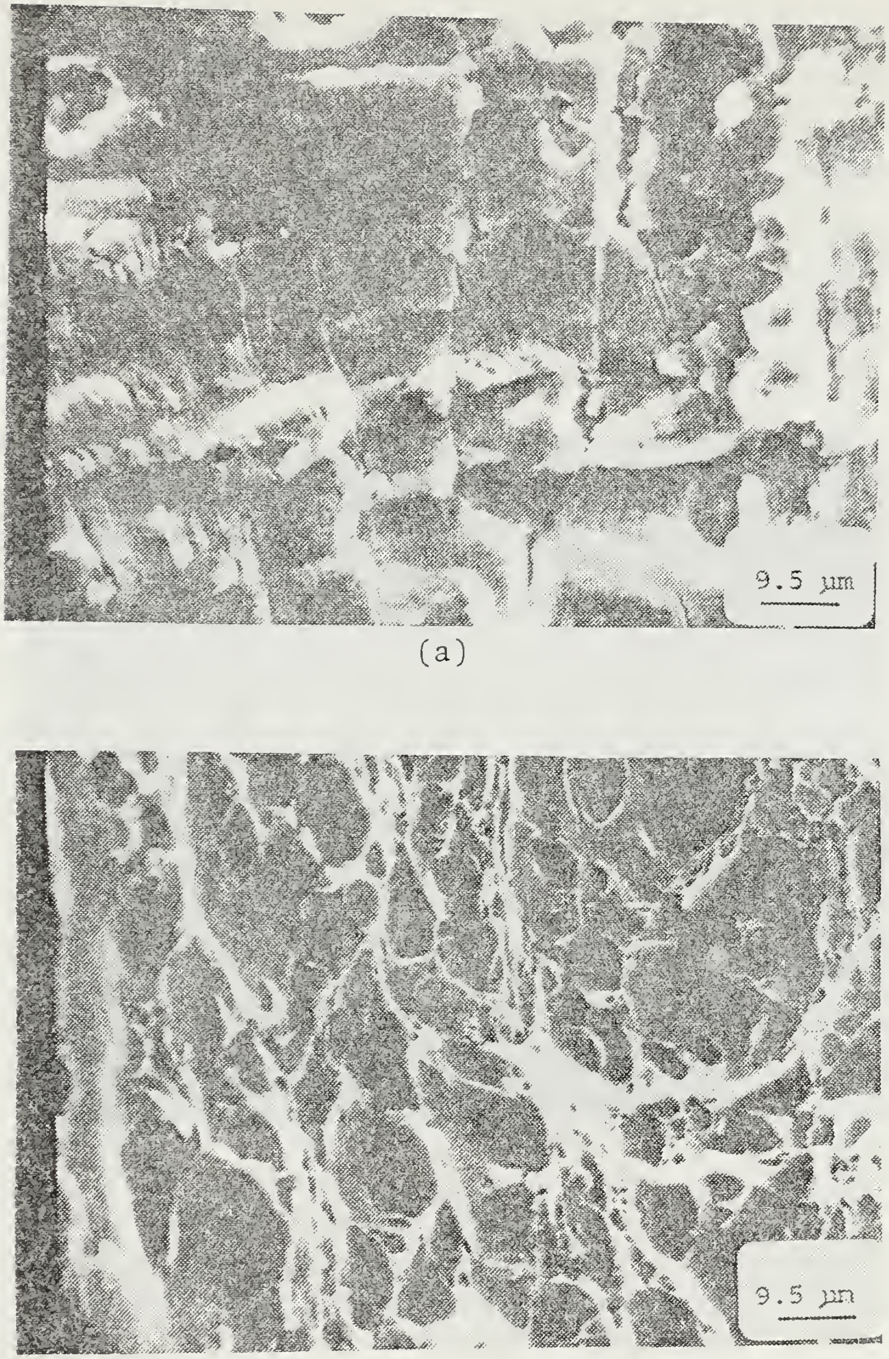

(a)

(b)

FIGURE 42. SEM fractographs of a specimen of Al-8.14 wt pct Mg-0.40 wt pct Cu solution treated, oil-quenched and warm-rolled at 300°C, in which failure occurred after 110200 cycles; (a) Stage II crack growth x1050; (b) Stage III crack growth x1050

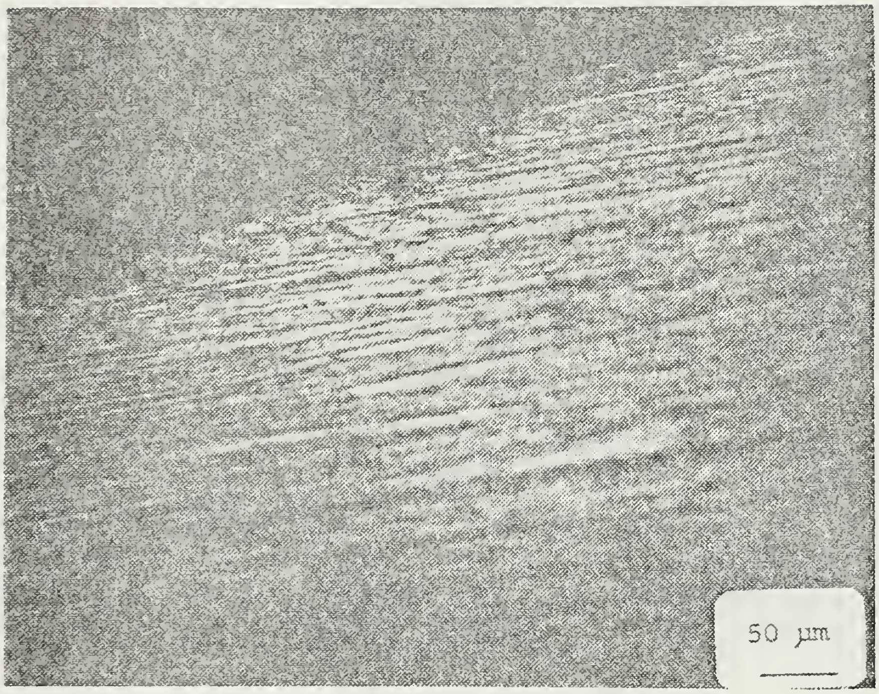

FIGURE 43. Microcrack formation on the surface of Al-8.14 wt pct Mg-0.40 wt pct Cu solution treated, oil-quenched and warm-rolled at 300°C. test terminated after 10^7 cycles without failure

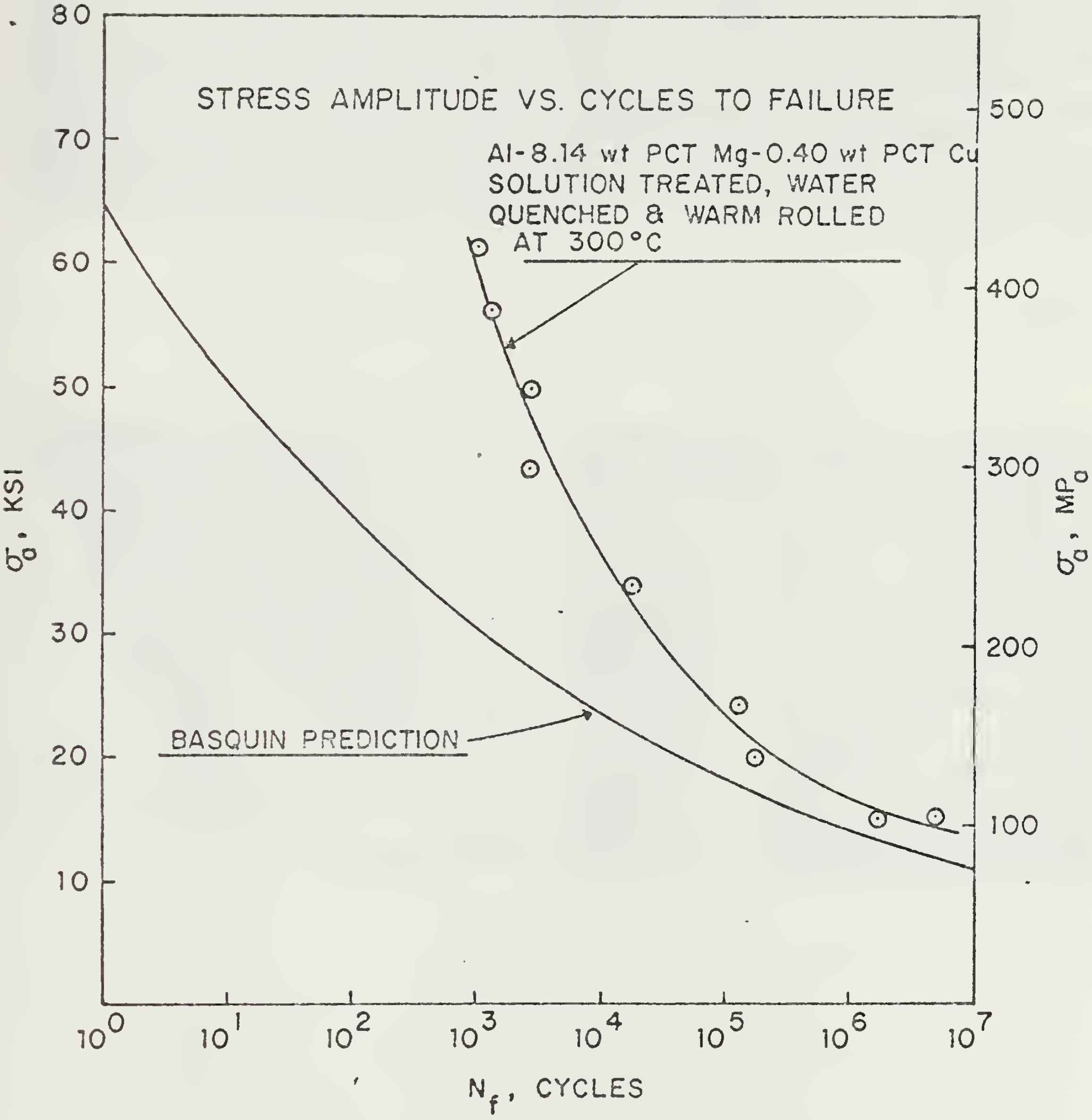

FIGURE 44. Stress amplitude vs cycles to failure for Al-8.14 wt pct Mg-0.40 wt pct Cu, solution treated water-quenched and warm rolled at 300°C

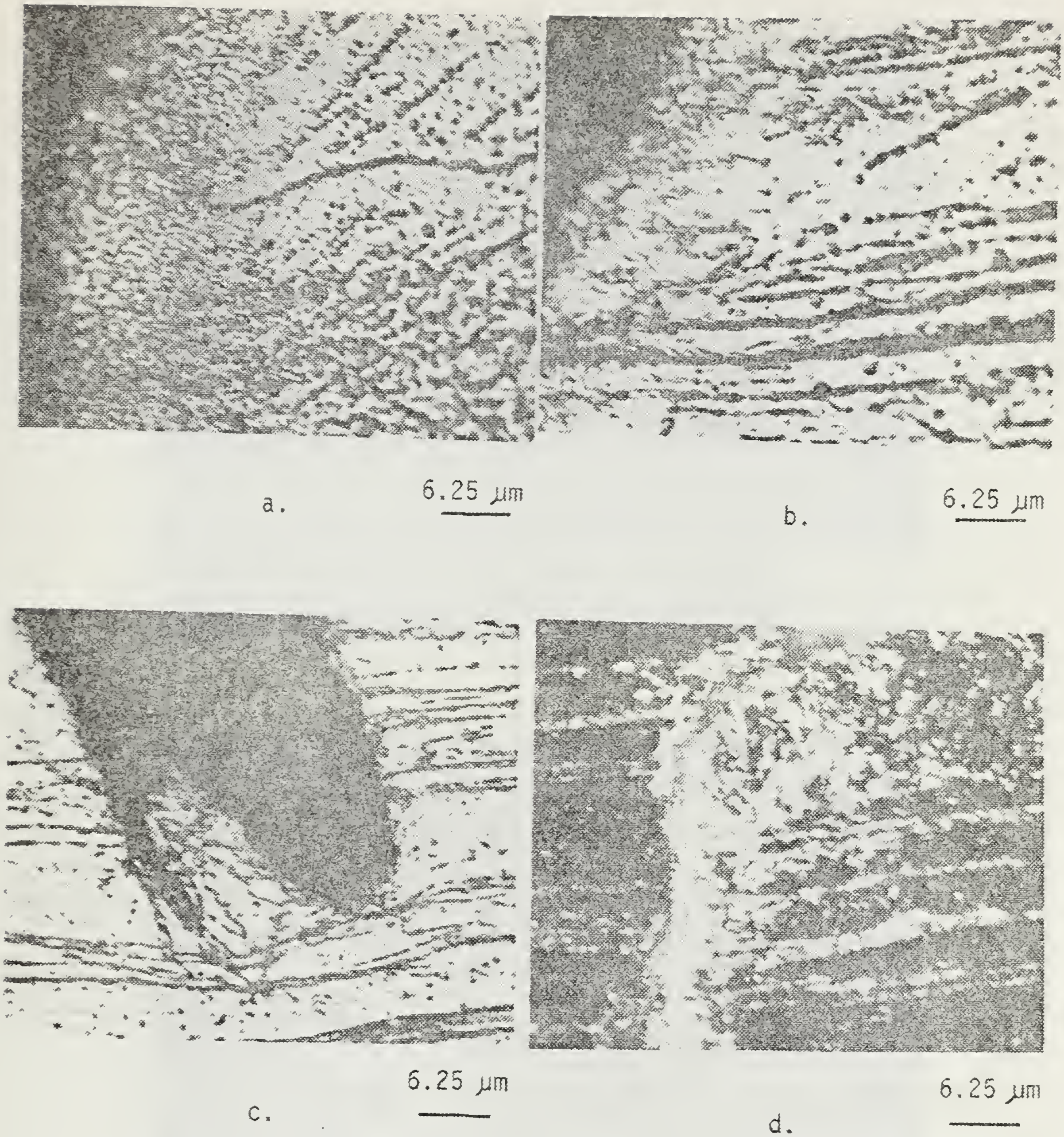

FIGURE 45. Optical micrographs of a low cycle fatigued specimen of Al-8.14 wt pct Mg-0.40 wt pct Cu, solution treated, water-quenched and warm-rolled at 300°C: (a) region adjacent to the main fracture surface; (b) region adjacent to the main fracture surface; (c) region adjacent to a blunt tipped secondary crack; and (d) region adjacent to and in front of a crack tip (dark field image)

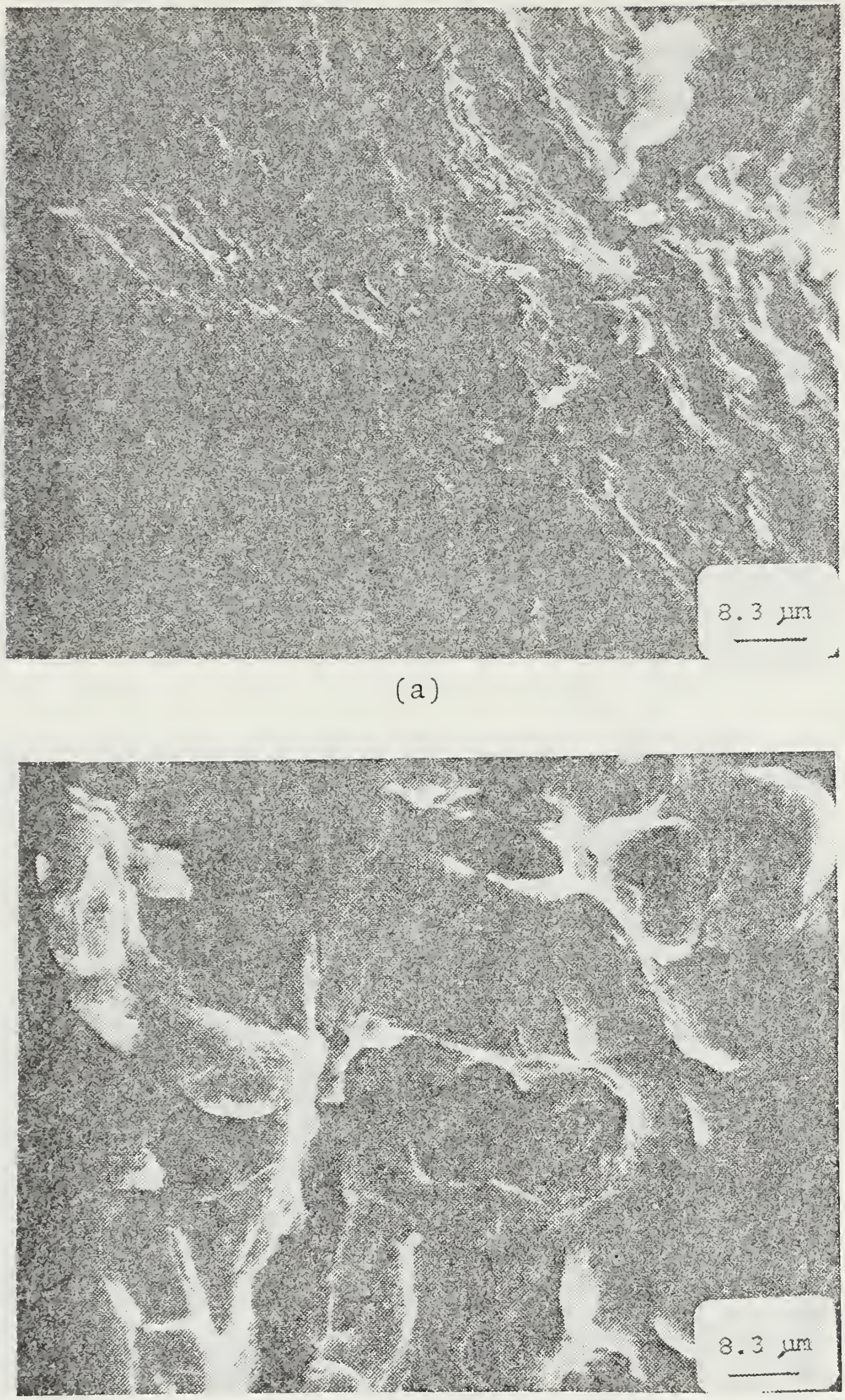

(a)

(b)

FIGURE 46. SEM fractographs of Al-8.14 wt pct Mg-0.40 wt pct Cu, solution treated, water-quenched and warm-rolled at 300°C; in which failure occurred after 2700 cycles: (a) Stage II crack growth x1200; (b) Stage III crack growth x1200

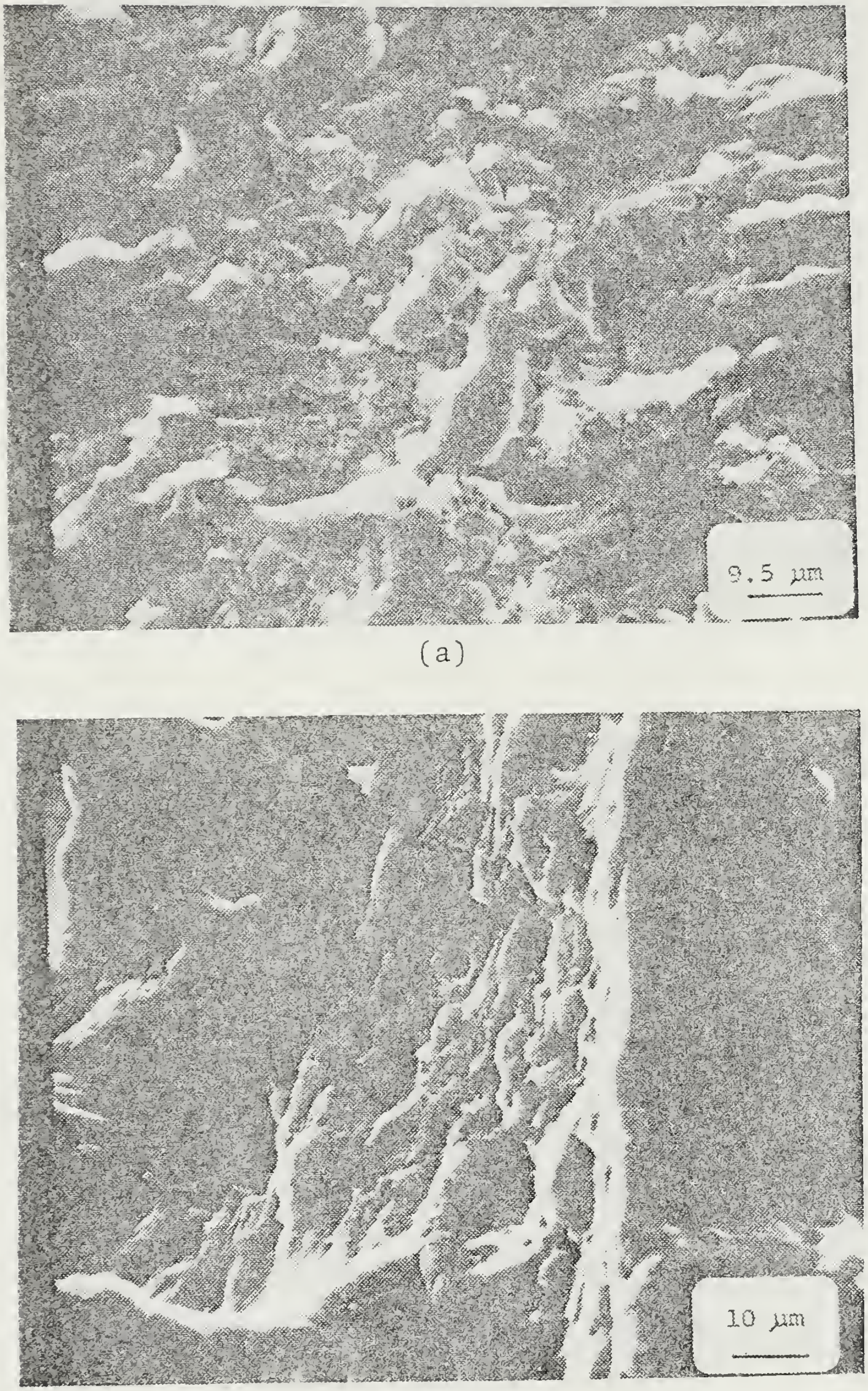

(a)

(b)

FIGURE 47. SEM fractographs of Al-8.14 wt pct Mg-0.40 wt pct Cu, solution treated, water-quenched, and warm-rolled at 300°C, in which failure occurred after 13.4×10^4 cycles: (a) Stage II crack growth x1000; (b) Stage III crack growth x1050

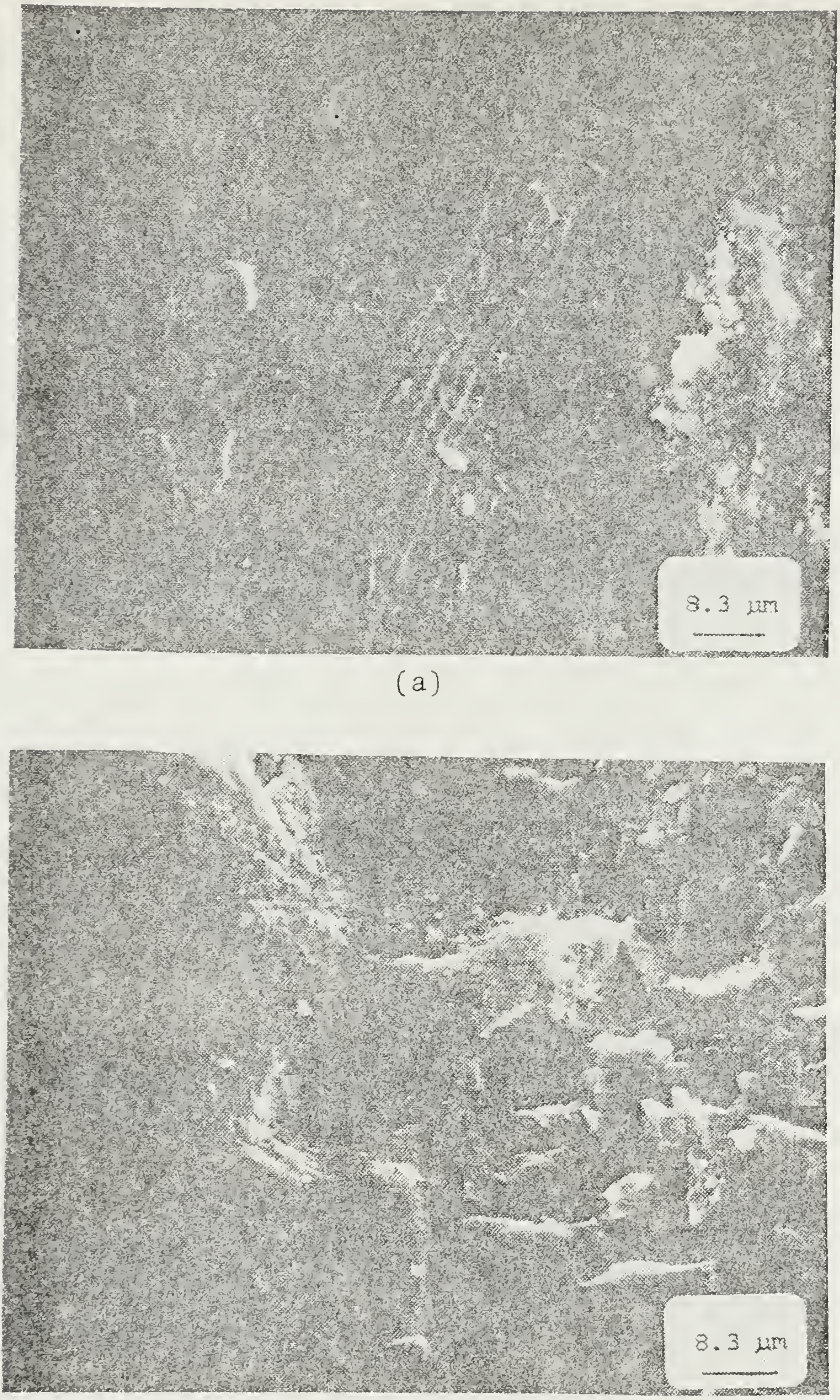

(a)

(b)

FIGURE 48. SEM fractographs of Al-8.14 wt pct Mg-0.40 wt pct Cu, solution treated, water-quenched and warm-rolled at 300°C, in which failure occurred after 4.8×10^6 cycles: (a) Stage II crack growth x1200; (b) Stage III crack growth x1200

LIST OF REFERENCES

1. Ness, F. G., Jr., High Strength to Weight Aluminum-18 Weight Percent Magnesium Alloy Through Thermal Mechanical Processing, M.S. Thesis, Naval Postgraduate School, Monterey, California, December 1976.

2. Bingay, C. P., Microstructural Response of Aluminum-Magnesium Alloys to Thermomechanical Processing, M.S. Thesis, Naval Postgraduate School, Monterey, California, December 1977.

3. Glover, T. L., Effects of Thermomechanical Processing on Aluminum-Magnesium Alloys Containing High Weight Percentage Magnesium, M.S. Thesis, Naval Postgraduate School, Monterey, California, December 1977.

4. Grandon, R. A., High Strength Aluminum-Magnesium Alloys: Thermomechanical Processing, Microstructure and Tensile Mechanical Properties, M.S. Thesis, Naval Postgraduate School, Monterey, California, December 1979.

5. Speed, W. G., An Investigation into the Influence of Thermomechanical Processing on Microstructure and Mechanical Properties of High-Strength Aluminum-Magnesium Alloys, M.S. Thesis, Naval Postgraduate School, Monterey, California, December 1979.

6. Chesterman, C. W., Jr. Precipitation, Recovery and Recrystallization Under Static and Dynamic Conditions for High-Magnesium Aluminum-Magnesium Alloys, M.S. Thesis, Naval Postgraduate School, Monterey, California, March 1980.

7. Johnson, R. B., The Influence of Alloy Composition and Thermo-Mechanical Processing Procedure on Microstructure and Mechanical Properties of High-Magnesium Aluminum Magnesium Alloys, M.S. Thesis, Naval Postgraduate School, Monterey, California, June 1980.

8. Sanders, T. H., Jr., and Staley, J. T., "Review of Fatigue and Fracture Research on High-Strength Aluminum Alloys," Fatigue and Microstructure, pp. 467-522, American Society for Metals, 1979.

9. American Society for Metals, Metals Handbook Ninth Edition Volume 2, Properties and Selection: Nonferrous Alloys and Pure Metals, pp. 44-62, American Society for Metals, 1979.

10. Mondolfo, L. F. Aluminum Alloys: Structure and Properties, pp. 311-322, Butterworth & Co. (Publishers), 1976.

11. Bly, D. L. Sherby, O. D., and Young, C. M., "Influence of Thermal Mechanical Treatments on the Mechanical Properties of a Finely Spheroidized Eutectic Composition Steel," Materials Science and Engineering, Vol. 12, pp. 41-46, 1973.

12. American Society for Metals, Metals Handbook Eight Edition Volume 10 Failure Analysis and Prevention, pp. 95-112, American Society for Metals, 1975.

13. Boyapati, K. and Polmear, I. J. "Effects of Silver in Tensile and Fatigue Properties of an Aluminum-Magnesium Alloy," Strength of Metals and Alloy Preceedings, 15th International Conference on the Strength of Metals and Alloys, Aachen, West Germany, August 1979.

14. Prince, K. C. and Martin, J. W., "The Effects of Dispersoids Upon the Micromechanisms of Crack Propagation in Al-Mg-Si Alloys," Acta Metallurgica, Vol. 27, pp. 1401-1408, 1979.

15. Dowling, J. M. and Martin, "The Influence of Mn Additions on the Deformation Behaviour of an Al-Mg-Si Alloy," Acta Metallurgica, Vol. 24, pp. 1147-1153, 1979.

16. Mondolfo, L. F., Aluminum Alloys: Structure and Properties, p. 499, Butterworth & Co. (Publishers), 1976.

17. Mondolfo, L. F., Aluminum Alloys: Structure and Properties, p. S49, Butterworth & Co. (Publishers), 1976.

18. Forsyth, P. J. E., The Physical Basis of Metal Fatigue, p. 71, American Elsevier Publishing Company, Inc., New York, 1969.

19. Stubbington, C. A., Journal Institute of Metals, Vol. 88, p. 227, 1959-1960.

20. Forsyth, P. J. E., The Physical Basis of Metal Fatigue, p. 151, American Elsevier Publishing Company, Inc., New York, 1969.

21. ASTM, Manual on Fatigue Testing, pp. 30-79, American Society for Testing Materials, 1949.

22. Popov, E. P., Introduction to Mechanics of Solids, p. 183, Prentice-Hall, Inc., 1968.

23. Popov, E. P., Introduction to Mechanics of Solids, p. 555, Prentice-Hall, Inc., 1968.

24. Basquin, O. H., Proc., ASTM, Vol. 10, Part II, p. 625, 1910.

25. Hertzberg, R. W., Deformation and Fracture Mechanics of Engineering Materials, p. 415-463, John Wiley & Sons, 1976.

26. ASM, Metals Handbook 8th Edition, Vol. 8, pp. 124-129, American Society for Metals, 1973.

27. Vining, P. G., Mechanisms of Elevated Temperature Fatigue Damage in 2 1/4 Cr - 1 Mo Steels, M.S. Thesis, Naval Postgraduate School, Monterey, California, June 1981.

28. Schultz, C. W., Effect of Thermomechanical Treatment on the Microstructure and Mechanical Properties of AISI 52100 Steel, M.S. Thesis, Naval Postgraduate School, Monterey, California, March 1981.

29. Nutting, J., "The Influence of Plastic Strain Upon the Aging Characteristics of Alloys," Metallurgical Transactions, Vol. 2, pp. 45-51, January 1971.

30. Calabrese, C. and Laird, C., "High Strain Fatigue Fracture Mechanisms in Two Phase Alloys," Metallurgical Transaction, Vol. 5, pp. 1785-1793, August 1974.

31. Hertzberg, R. W., Deformation and Fracture Mechanics of Engineering Materials, p. 97, John Wiley & Sons, 1976.

INITIAL DISTRIBUTION LIST

		No. Copies
1.	Defense Technical Information Center Cameron Station Alexandria, Virginia 22314	2
2.	Library, Code 0142 Naval Postgraduate School Monterey, California 93940	2
3.	Department Chairman, Code 69Mx Department of Mechanical Engineering Naval Postgraduate School Monterey, California 93940	1
4.	Professor T. R. McNelley, Code 69Mc Department of Mechanical Engineering Naval Postgraduate School Monterey, California 93940	5
5.	Professor M. Edwards Metallurgy Branch The Royal Military College of Science Shrivenham, Swindon, Wilts SN6-8LA ENGLAND	3
6.	Assistant Professor K.D. Challenger Code 69Ch Department of Mechanical Engineering Naval Postgraduate School Monterey, California 93940	1
7.	LT Charles A. Cadwell, Jr., USN Supervisor of Shipbuilding Bath, Maine 62786	2

Thesis
C166
c.1

Cadwell 193218

Fatigue characteristics and microstructural analysis of thermomechanically-processed, high-magnesium aluminum-magnesium alloy.

Thesis 193218
C166 Cadwell
c.1
Fatigue characteristics and microstructural analysis of thermomechanically-processed, high-magnesium aluminum-magnesium alloy.

thesC166
Fatigue characteristics and microstructu
3 2768 002 08427 9
DUDLEY KNOX LIBRARY